A Three-Dimensional Fully Nonlinear Model in Curvilinear Coordinates for Simulating Waves Interaction with a Bottom-Mounted or Partially-Submerged Fixed Cylindrical Structure

A Dissertation

Presented to

the Faculty of the Department of Civil and Environmental Engineering

University of Houston

In Partial Fulfillment

of the Requirements for the Degree

Doctor of Philosophy

in Civil Engineering

by

Yu-Hsiang Chen

May 2016

A Three-Dimensional Fully Nonlinear Model in Curvilinear Coordinates for Simulating Waves Interaction with a Bottom-Mounted or Partially-Submerged Fixed Cylindrical Structure

_____

Yu-Hsiang Chen

Approved:

_____
Chair of the Committee
Keh-Han Wang, Professor,
Civil and Environmental Engineering

Committee Members:

_____
Yi-Lung Mo, Professor,
Civil and Environmental Engineering

_____
Cumaraswamy Vipulanandan, Professor,
Civil and Environmental Engineering

_____
Alaa M. Mansour, Associate Professor,
Civil Engineering,
Cairo University

_____
Qin Qian, Associate Professor,
Civil and Environmental Engineering,
Lamar University

_____
Suresh K. Khator, Associate Dean
Cullen College of Engineering

_____
Roberto Ballarini, Professor and Chair
Civil and Environmental Engineering

Acknowledgments

I would like to express my sincere gratitude to my advisor, Dr. K. H. Wang, for the guidance, support, and encouragement throughout this research and the writing of the dissertation. I appreciate he has contributed a lot to my personal and scientific development.

I would also like to thank Dr. Yi-Lung Mo, Dr. Cumaraswamy Vipulanandan, Dr. Alla M. Mansour, and Dr. Qin Qian for their serving on my dissertation committee and giving me a lot of suggestions to complete this dissertation.

I have to express my deepest gratitude to my parents for their encouragement, assistance, love, and support. I also want to thank my sister, little brother, Min-Fang, and my aunt's family for their generous support.

I would like to thank my colleagues, Dr. Ted Chu, Fangfang Sheng, and Fong-Shu Jao, for their kind support and assistance, especially for helping me to carry out the experiments. I would also like to specially thank Dr. Ted Chu and Dr. Zhengyong Zhong for helpful discussion and suggestions on the numerical method.

Last but not least, I wish to thank all of you who have assisted me in various ways throughout my graduate studies.

A Three-Dimensional Fully Nonlinear Model in Curvilinear Coordinates for Simulating Waves Interaction with a Bottom-Mounted or Partially-Submerged Fixed Cylindrical Structure

An Abstract

of a

Dissertation

Presented to

the Faculty of the Department of Civil and Environmental Engineering

University of Houston

In Partial Fulfillment

of the Requirements for the Degree

Doctor of Philosophy

in Civil Engineering

by

Yu-Hsiang Chen

May 2016

Abstract

This dissertation presents a three-dimensional fully nonlinear wave model developed to simulate solitary waves propagating in straight or curved channels and interactions bottom mounted or partially submerged structures. The three-dimensional Laplace equation and fully nonlinear boundary conditions are solved numerically by the finite difference method. In order to have the computational grids fit closely to the curved structural boundaries and the time varying free surface for numerical advantage, the transient three-dimensional curvilinear coordinate transformation technique is adopted to convert the original governing equation and boundary conditions in Cartesian coordinates into the curvilinear coordinate based formulations.

The effects of grid size and time step on the accuracy and convergence of the present numerical model are examined and discussed by simulating a solitary wave freely propagating in a straight rectangular channel. Then, the feature of the curvilinear coordinate transformation is tested by modeling the case of a solitary wave propagating in a 180° curved channel. After comparing with the results obtained from the generalized Boussinesq (gB) two-equation model, this three-dimensional model can produce stable and accurate predictions on nonlinear waves propagation in a channel with irregular boundary.

The present three-dimensional model is extended to solve the wave and structure interaction problems. One of the cases is a solitary wave impinging a bottom mounted and surface piercing vertical cylinder. The results obtained from the present three-dimensional model shows a reasonable agreement with the experimental measurements

and those calculated from the gB model. The other case is a solitary wave interacting with a partially submerged and fixed floating cylinder. Laboratory tests for a solitary wave passing through a partially immersed and fixed floating cylinder were conducted to verify the present three-dimensional model performance. The numerical results of the present model match well with the experimental measurements. It is demonstrated through these comparisons that the present three-dimensional fully nonlinear wave model can provide reliable predictions on wave evolution and loading for a solitary wave interacting with selected cylindrical structures.

Table of Contents

Acknowledgments iv

Abstract. vi

Table of Contents viii

List of Figures xi

List of Symbols xvii

Chapter 1 Introduction 1

1.1 PRACTICAL SIGNIFICANCE 1

1.2 STATEMENT OF THE PROBLEM 2

1.3 LITERATURE REVIEW 5

1.1 Shallow water waves interacting with bottom mounted cylindrical structures 5

1.2 Water waves interacting with floating structures 8

1.3 Water wave propagation in a curved channel 11

1.4 OUTLINE OF THE DISSERTATION 12

Chapter 2 Theoretical Model for Fully Nonlinear Water Waves 16

2.1 GOVERNING EQUATIONS 16

2.2 BOUNDARY CONDITIONS 20

2.2.1 Free-surface boundary conditions 20

2.2.2 Bottom boundary condition 21

2.2.3 Solid side wall and structural boundary conditions 21

2.2.4 Open boundary conditions 21

2.3 Initial Condition for Incident Solitary Waves 23
2.4 Forces on cylinders 24
2.5 Three-Dimensional Transient Curvilinear Coordinate Transformation 26
Chapter 3 Numerical Method 32
3.1 Finite Difference Formulations 32
3.2 Computational Domain with Multi-grid Systems 37
3.3 Validation of the Numerical Model 42
3.3.1 Selection of time step and grid size 45
3.3.2 Mass conservation 49
3.4 Solitary waves propagating in a curved channel 51
Chapter 4 Solitary Waves Interacting with a and Bottom Mounted Surface Piercing Vertical Cylinder 75
4.1 Interaction Process 77
4.2 Comparisons of the Present Model Results with Other Published Solutions and Experimental Data 82
Chapter 5 Solitary Waves Interacting with a Fix Floating Cylinder 98
5.1 Experimental Measurement 99
5.2 Comparisons of the Present Model Results with Experimental Measurements and Analysis of the Effect of the Draft 103
5.3 Forces on a Partially Immersed and Fixed Floating Cylinder 107
5.4 Interaction Process 111

Chapter 6 Summary and Conclusions 117

References 122

List of Figures

FIGURE 2- 1 COORDINATE SYSTEM FOR THE DESCRIPTION OF THE GOVERNING EQUATIONS: (A) BOTTOM MOUNTED AND SURFACE PIERCING VERTICAL CYLINDER, AND (B) FIXED FLOATING CYLINDER 19

FIGURE 3- 1 TWO-GRID SYSTEM WITH ARRANGED GRID POINTS FOR A BOTTOM MOUNTED AND SURFACE PIERCING CYLINDER SITUATED IN A COMPUTATIONAL DOMAIN 38

FIGURE 3- 2 AN X-Z PLANE VIEW OF THE GRID SYSTEM IN THE PHYSICAL DOMAIN 39

FIGURE 3- 3 GRID ARRANGEMENT WITH TWO RECTANGULAR GRID SYSTEMS AND ONE POLAR GRID SYSTEM FOR THE FLOW DOMAIN INCLUDING A REGION BENEATH A PARTIALLY SUBMERGED CYLINDER. 41

FIGURE 3- 4 THREE-DIMENSIONAL PERSPECTIVE VIEW PLOT OF THE FREE-SURFACE ELEVATION FOR AN $\alpha = 0.4$ INCIDENT SOLITARY WAVE AT $t = 50$ 43

FIGURE 3- 5 A SEQUENCE OF TIME SERIES PLOTS OF NUMERICALLY SIMULATED SOLITARY WAVES PROPAGATING IN A CHANNEL OF CONSTANT DEPTH ($\alpha = 0.4$)..... 44

FIGURE 3- 6 COMPARISONS OF NUMERICAL WAVE ELEVATION PROFILES OF DIFFERENT TIME INTERVAL FOR SOLITARY WAVES PROPATION WITH A CONSTANT DEPTH ($\Delta x = \Delta y = 0.25$, $t = 30$) 46

FIGURE 3- 7 COMPARISONS OF NUMERICAL PROFILES OF DIFFERENT GRID SIZES IN X-DIRECTION FOR SOLITARY WAVES PROPATION WITH A CONSTANT DEPTH ($\Delta t = 0.1$) 48

FIGURE 3- 8 COMPARISONS OF NUMERICAL PROFILES OF DIFFERENT GRID SIZES IN Y-DIRECTION FOR SOLITARY WAVES PROPATION WITH A CONSTANT DEPTH ($\Delta t = 0.1$) 48

FIGURE 3- 9 COMPARISONS OF NUMERICAL PROFILES OF DIFFERENT GRID SIZES IN X-DIRECTION FOR SOLITARY WAVES PROPATION WITH A CONSTANT DEPTH ($\Delta x = \Delta y = 0.25, \Delta t = 0.1$) 49

FIGURE 3- 10 TIME VARIATION OF TOTAL EXCESS MASS WITHIN THE COMPUTATIONAL DOMAIN 50

FIGURE 3- 11 A VERTICAL VIEW OF THE U-SHAPE CURVED CHANNEL 51

FIGURE 3- 12 THREE-DIMENSIONAL PERSPECTIVE VIEW PLOT OF AN INITIAL SOLITARY WAVE WITH $\alpha = 0.3$ 52

FIGURE 3- 13 THREE DIMENSIONAL PERSPECTIVE VIEW AND CONTOUR PLOTS OF FREE-SURFACE ELEVATION Z FOR $\alpha = 0.3$ AT DIFFERENT TIME STEPS 54

FIGURE 3- 14 THE LOCATION OF COMPARISONS OF TIME VARIATION OF FREE-SURFACE ELEVATION 68

FIGURE 3- 15 COMPARISONS OF TIME VARIATIONS OF FREE-SURFACE ELEVATIONS OBTAINED FROM GB MODEL AND THE PRESENT 3D FULLY NONLINEAR MODEL AT THE POSITIONS OF "OUTER WALL", "CENTER OF CHANNEL", AND "INNER WALL" IN CROSS SECTION A 70

FIGURE 3- 16 COMPARISONS OF TIME VARIATIONS OF FREE-SURFACE ELEVATIONS OBTAINED FROM GB MODEL AND THE PRESENT 3D FULLY NONLINEAR MODEL AT THE POSITIONS OF "OUTER WALL", "CENTER OF CHANNEL", AND "INNER WALL" IN CROSS SECTION B 71

FIGURE 3- 17 COMPARISONS OF TIME VARIATIONS OF FREE-SURFACE ELEVATIONS OBTAINED FROM GB MODEL AND THE PRESENT 3D FULLY NONLINEAR MODEL AT THE POSITIONS OF "OUTER WALL", "CENTER OF CHANNEL", AND "INNER WALL" IN CROSS SECTION C 72

FIGURE 3- 18 COMPARISONS OF TIME VARIATIONS OF FREE-SURFACE ELEVATIONS OBTAINED FROM GB MODEL AND THE PRESENT 3D FULLY NONLINEAR MODEL AT THE POSITIONS OF "OUTER WALL", "CENTER OF CHANNEL", AND "INNER WALL" IN CROSS SECTION D 73

FIGURE 3- 19 COMPARISONS OF TIME VARIATIONS OF FREE-SURFACE ELEVATIONS OBTAINED FROM GB MODEL AND THE PRESENT 3D FULLY NONLINEAR MODEL AT THE POSITIONS OF "OUTER WALL", "CENTER OF CHANNEL", AND "INNER WALL" IN CROSS SECTION E 74

FIGURE 4- 1 SCHEMATIC DIAGRAM OF INITIAL SOLITARY WAVE INCIDENT UPON SURFACE-PIERCING BOTTOM MOUNTED VERTICAL CYLINDER 76

FIGURE 4- 2 THREE-DIMENSIONAL PERSPECTIVE VIEW PLOT OF FREE-SURFACE ELEVATION Z FOR $\alpha = 0.4$ AT SELECTED INSTANTS OF TIME 78

FIGURE 4- 3 CONTOUR PLOT OF THE FREE-SURFACE ELEVATION FOR AMPLITUDE OF A SOLITARY WAVE A=0.4 AND CYLINDER DIAMETER R =1.5875 AT T=40 81

FIGURE 4- 4 COMPARISONS OF TIME VARIATION OF FREE-SURFACE ELEVATION ALONG θ = 0° AT (A) r/R=4.5 AND (B) r/R=2.61 OBTAINED FROM THE PRESENT 3D NONLINEAR MODEL, THE GB-FDM (WANG ET AL., 1992), AND EXPERIMENTAL DATA (YETES AND WANG, 1994) 84

FIGURE 4- 5 COMPARISONS OF TIME VARIATION OF FREE-SURFACE ELEVATION ALONG $\theta =$ 60° AT (A) r/R=3.87 AND (B) r/R=2.92 OBTAINED FROM THE PRESENT 3D NONLINEAR MODEL, THE GB-FDM (WANG ET AL., 1992), AND EXPERIMENTAL DATA (YETES AND WANG, 1994) 86

FIGURE 4- 6 COMPARISONS OF TIME VARIATION OF FREE-SURFACE ELEVATION ALONG $\theta =$ 100° AT (A) r/R=2.92 AND (B) r/R=2.29 OBTAINED FROM THE PRESENT 3D NONLINEAR MODEL, THE GB-FDM (WANG ET AL., 1992), AND EXPERIMENTAL DATA (YETES AND WANG, 1994) 89

FIGURE 4- 7 COMPARISONS OF TIME VARIATION OF FREE-SURFACE ELEVATION ALONG $\theta =$ 150° AT (A) r/R=2.92 AND (B) r/R=2.29 OBTAINED FROM THE PRESENT 3D NONLINEAR MODEL, THE GB-FDM (WANG ET AL., 1992), AND EXPERIMENTAL DATA (YETES AND WANG, 1994) 91

FIGURE 4- 8 COMPARISONS OF TIME VARIATION OF FREE-SURFACE ELEVATION ALONG $\theta =$ 180° AT (A) r/R=2.92 AND (B) r/R=2.29 OBTAINED FROM THE PRESENT 3D NONLINEAR MODEL, THE GB-FDM (WANG ET AL., 1992), AND EXPERIMENTAL DATA (YETES AND WANG, 1994) 93

FIGURE 4- 9 COMPARISONS OF FORCE COEFFICIENT CfH IN TIME SEQUENCE, (A) $\alpha = 0.18$, (B) $\alpha = 0.24$, (C) $\alpha = 0.32$, AND (D) $\alpha = 0.4$..... 96

FIGURE 5- 1 SCHEMATIC DIAGRAM OF INITIAL SOLITARY WAVE INCIDENT UPON FIXED FLOATING CYLINDER 99

FIGURE 5- 2 THE EXPERIMENTAL SETUP IN THE GLASS-WALLED FLUME FOR MEASURING THE WAVE AMPLITUDE IN FRONT OF THE CYLINDER..... 100

FIGURE 5- 3 SCHEMATIC DIAGRAM OF EXPERIMENT SETUP: (A) MEASUREMENT FREE SURFACE ELEVATION IN FRONT OF CYLINDER; (B) MEASUREMENT FREE SURFACE ELEVATION IN BACK OF CYLINDER 101

FIGURE 5- 4 THE PARTIALLY IMMERSED AND FIXED FLOATING CYLINDER FOR EXPERIMENT 103

FIGURE 5- 5 COMPARISONS OF TIME VARIATION OF FREE SURFACE ELEVATION OBTAINED FROM NUMERICAL AND EXPERIMENTAL MEASUREMENT: (A) IN FRONT OF THE CYLINDER ($\theta = 0°$) AND (B) IN BACK OF THE CYLINDER ($\theta = 180°$)..... 105

FIGURE 5- 6 COMPARISONS OF TIME VARIATION OF FREE SURFACE ELEVATION OBTAINED FROM THE PRESENT MODEL WITH GAP G = 0.3, 0.5, AND 0.7: IN FRONT OF THE CYLINDER ($\theta = 0°$) 106

FIGURE 5- 7 COMPARISONS OF TIME VARIATION OF FREE SURFACE ELEVATION OBTAINED FROM THE PRESENT MODEL WITH GAP G = 0.3, 0.5, AND 0.7: AT THE BACK OF THE CYLINDER ($\theta = 180°$) 107

FIGURE 5- 8 COMPARISONS OF FORCE COEFFICIENT, C_{fH}, CALCULATED BY THE PRESENT THREE-DIMENSIONAL MODEL AND MORISON EQUATION IN TIME SEQUENCE 110

FIGURE 5- 9 VERTICAL FORCE COEFFICIENT C_{fV}, CALCULATED BY THE PRESENT THREE-DIMENSIONAL MODEL IN TIME SEQUENCE 110

FIGURE 5- 10 THREE-DIMENSIONAL PERSPECTIVE VIEW PLOT OF FREE-SURFACE ELEVATION Z FOR $\alpha = 0.3$ AT SELECTED INSTANTS OF TIME (PARTIALLY SUBMERGED CYLINDER CASE)..... 113

FIGURE 5- 11 CONTOUR PLOT OF THE FREE-SURFACE ELEVATION FOR AMPLITUDE OF THE SOLITARY WAVE $\alpha = 0.4$ AND CYLINDER DIAMETER $R = 2.0$ AT $t = 42$.. 116

List of Symbols

c	Dimensionless phase speed
c^*	Dimensional phase speed
C_D	Drag coefficient
C_M	Inertia coefficient
C_{fH}	Horizontal force coefficient
C_{fV}	Vertical force coefficient
e_x	Unit normal direction along the *x*-axis
e_z	Unit normal direction along the *z*-axis
F_D	Drag force
F_H	Horizontal wave force
F_I	Inertia force
g	Gravitational acceleration
G	Dimensionless space between the bottom of cylinder and the channel bed
h	Dimensionless water depth
h^*	Dimensional water depth
h_0	Typical water depth
h_0^*	Dimensional reference water depth
H	Dimensional wave height
k	Wave number

Kc	Keulegan-Carpenter number
p	Pressure
R	Radius of cylinder
Re	Reynold number
t	Dimensionless time
t^*	Dimensional time
u, v, w	Dimensionless three-dimensional velocity vector
u^*, v^*, w^*	Dimensional three-dimensional velocity vector
x, y, z	Dimensionless coordinates in three-dimensional Cartesian system
x^*, y^*, z^*	Dimensional coordinates in three-dimensional Cartesian system
α	Dimensionless wave height
ξ, η, γ	The transformed coordinate
ζ	Dimensionless water surface elevation
ζ^*	Dimensional water surface elevation
θ	Angle of the angular direction measured from the x-axis
λ	Characteristic wave length
ρ	Fluid dentcity
ϕ	Dimensionless velocity potential
ϕ^*	Dimensional velocity potential

Chapter 1

Introduction

1.1 Practical Significance

Water waves commonly occur in nature. They are routinely generated by many factors, such as wind, gravitational forces between the sun, moon, and earth, undersea earthquakes, and others. As ocean covers nearly three-quarters of the surface of the earth, the consequence of wave motion and its interaction with structures is closely associated with human activities. The occurrence of extreme waves as a result of undersea earthquakes, hurricanes (typhoons), or eruptions of submarine volcanoes can cause devastating property damage and loss of life. In 2011, a submarine earthquake triggered a tsunami at Japan's northeastern offshore and has resulted in the loss of nearly 18,000 lives, billions of dollars of property damages, and a world shocking crisis of a nuclear power plant. A tsunami is one kind of extreme wave that behaves as a nonlinear shallow-water wave. It is essential to understand the formation and transformation of water waves under different scenarios, especially shallow-water waves. Thus, detailed investigation of nonlinear shallow-water waves has become increasingly important. A wide range of topics related to costal and offshore engineering applications, such as design of offshore structures, coastal seawalls, breakwaters, harbors, and so on, have been studied in the past decades. However, as the layout of the costal and offshore structures become more complicated, it is increasingly challenging to develop proper methods to solve the complex governing equations and physical boundary conditions describing the interaction

process between waves and structures. Thus, to advance the capability of wave-structure interaction modeling, the present study focuses on the development of curvilinear coordinates based fully nonlinear wave model to investigate the interaction between waves and three-dimensional structures.

1.2 Statement of the Problem

The main fluid body of water waves can be assumed to be incompressible and its motion irrotational. With this assumption, a velocity potential that satisfies the Laplace equation can be defined to describe the wave motion. Certainly, the main problems faced in solving the wave related problems, either analytically or numerically, are mostly related to the formulation of the nonlinear boundary conditions, especially at the free surface, and solutions of the nonlinear equations. Linear water wave theory can provide the simplified and approximate solutions for the fully nonlinear waves by neglecting some of the nonlinear effects. However, the linear wave solutions cannot truly reflect the physical impacts caused by the nonlinear waves, especially the extreme waves, on wave elevations and wave loads on structures. The waves in higher dimensions, such as the three-dimensional, increase the difficulty of solving the real wave problems.

If the focus of the study is to determine the free-surface elevation and vertically averaged flow variables, then the three-dimensional problems can be formulated by two-dimensional equations. A Boussinesq model is a typical example of two-dimensional models applied to three-dimensional wave propagation. The Boussinesq equations, due to their orders of accuracy, are best described as the weakly nonlinear and weakly dispersive shallow-water waves. In the past decades, a limited number of researchers have developed and extended the Boussinesq equations to engineering applications. The

generalized Boussinesq equations were derived by Wu (1979, 1981). Later, Wu and Wu (1982) established a numerical model for the generation and propagation of nonlinear long waves under a moving surface pressure condition. Nwogu (1993) modified the Boussinesq equations by using the velocity vector at an arbitrary depth as a dependent variable. This modification makes Boussinesq equations applicable to a wider range of water depths.

With the advancement of computing power, fully three-dimensional models may be developed to simulate complex wave propagation problems, as they can provide more detailed information on wave motion, velocity distribution, and especially the three-dimensional wave loadings on structures. One way to solve the fully three-dimensional wave problems is by adopting the three-dimensional Navier-Stokes equations as the governing equations. In addition, a free-surface tracking technique, such as the Volume of Fluids (VOF) method, needs to be applied to predict the free-surface elevations. However, the overall numerical computations are tedious and the VOF method is not effective for large scale simulations and tracking of the three-dimensional free surface. The other way of modeling wave propagation and wave-structure interaction in three dimensions is to solve the Laplace equations of the velocity potentials in various fluid regions satisfying the associated free-surface, interfacial and structural boundary conditions. The procedure allows the direct application of the kinematic and dynamic free-surface boundary conditions to accurately obtain the free-surface elevations in transient motion. For practical applications, the Laplace equations and boundary conditions can be solved up to the three-dimensional domain by selected numerical schemes, such as the finite difference, finite element or finite volume method.

Obtaining the numerical solutions requires the discretization of the governing equations into a set of algebraic equations of the unknown variables to be solved in the grid system of the computational domain. For three-dimensional computations, the finite difference method is considered to be an effective numerical scheme and can be easily applied to solve the model equations. However, it is limited to the domains with a regular and structured grid system. To extend the finite difference method to a domain with irregular boundaries, the boundary-fitted coordinate (or curvilinear coordinate) transformation technique (Thompson et al. 1974, 1977) has been applied to solve more complex wave-structure interaction problems. For example, Wang et al. (1992) developed a generalized Bousinessq numerical model in a curvilinear coordinate system in two horizontal dimensions to simulate scattering of solitary waves by a vertical cylinder. The model was also applied to study nonlinear long waves interacting with multiple vertical cylinders (e.g. Wang and Jiang, 1994; Wang and Ren, 1999). Recently, Chang and Wang (2011) developed a three-dimensional model using transient curvilinear coordinate transformation along the vertical direction to investigate the generation of nonlinear long waves by a submerged moving body. The three-dimensional nonlinear wave model with the three-dimensional curvilinear coordinate transformation technique has not yet been developed for simulating wave propagation and wave-structure interaction.

As the number of structures built in offshore or coastal environments increases, the study of wave and structure interaction becomes more important, especially under the conditions of nonlinear waves and floating structures. The wave run-up and forces acting on the structures are critical information for the design of the fixed or floating structures.

Wave run-up onto the deck, called green water load, can cause damage to the floating structures. Forces on the main offshore structures affect the overall design of the supporting structures, mooring lines, risers, and others. Three-dimensional numerical models can provide effective and comprehensive estimations of wave run-ups and forces on structures.

In this study, a three-dimensional fully nonlinear wave model, based on solving the Laplace equation and boundary conditions in a domain with three-dimensional curvilinear coordinate system, is developed to simulate propagation of solitary waves and their interactions with a bottom mounted and surface-piercing cylindrical structure or a floating cylindrical structure. Model results with selected cases will be validated by comparing the simulated solutions with measured data from Wang et al. (1994), present wave tank tests, and other published analytical and numerical results. Other results in terms of wave elevations and forces on structures are also presented.

Following the Introduction section, a Literature Review section is provided to describe the prior studies of nonlinear waves, especially the propagation of nonlinear long waves and their interactions with fixed or floating structures.

1.3 Literature Review

1.1 Shallow water waves interacting with bottom mounted cylindrical structures

The interactions between water waves and cylindrical structures have been investigated for decades. MacCamy and Fuchs (1954) applied the diffraction theory to study the interaction of long-crested waves with a vertical cylinder in general water

depths and compared the wave profiles with experimental measurements. Molin (1979) derived the nonlinear wave solutions to compute the second-order diffraction loads on three-dimensional bodies. For nonlinear long waves, Isaacson (1983) implemented the expressions of the free-surface elevation and velocity potential in Fourier integral forms to derive the analytical solutions on wave force and free-surface run-up for a solitary wave scattered around a vertical cylinder. Later, Basmat and Ziegler (1998) obtained higher-order equations for the diffraction of a solitary wave with a vertical cylinder and accordingly extended Isaacson's (1983) first-order approximation to second-order solutions.

For the class of nonlinear shallow-water (or long) waves, the two important dimensionless parameters, $\alpha = H/h_0$ and $\varepsilon = (h_0/\lambda)^2$, are assumed to be small. However, their ratio, known as the Ursell number, is of order one, or $\alpha = O(\varepsilon)$. Here, H is a representative wave height, h_0 is a typical water depth, and λ is a characteristic wavelength. The standard expansion method using the two small dimensionless parameters α and ε can be followed to derive the Boussinesq equations to describe the so-called weakly nonlinear and weakly dispersive waves. The Boussinesq equations have been widely applied numerically to study the propagation, transformation, and diffraction of nonlinear long waves under the influence of variable water depths and the existence of structures. The associated wave loads on structures have also been investigated.

The lower-order Boussinesq equations were originally derived in a domain of constant water depth. To extend the applications, the improved Boussinesq equations in higher order have been developed to describe the higher-order nonlinear long waves in a wide range of water depth (Peregrine, 1967; Wu, 1981, 1998; Nwogu, 1993; Wei and

Kirby, 1995; Agnon et al., 1999; Gobbi and Kirby, 2000; Madsen et al., 2002). Based on the concept of layer-mean velocity potentials, Wu (1979) developed a generalized Boussinesq two-equation model for modeling a three-dimensional nonlinear long wave propagating in shallow water. In 1998, Wu further derived the fully nonlinear and weakly dispersive Boussinesq equations for the study of fully nonlinear long waves. Wang et al. (1992) solved the generalized Boussinesq equations using the finite difference scheme and curvilinear coordinate system to investigate the three-dimensional scattering of solitary waves by a vertical cylinder. Later, Wang and Jiang (1994) and Wang and Ren (1998) adopted the concept of the multiple grid system, which provides a better fit of the grid system along the surface of cylindrical structures, to simulate the interaction between a solitary wave or a cnoidal wave with arrays of cylinders.

The finite element method was also introduced into the numerical approach of solving the Boussinesq equations because of the advantage of using non-uniform and unstructured grids. Katopodes et al. (1987) and Antunes et al. (1993) constructed the finite element models to solve the original Boussinesq equations. Fully unstructured meshes were used in a linear finite element model developed by Kawahara et al. (1994). For modeling shallow water wave interaction with structures, Ambrosi et al. (1998) and Woo et al. (2004) investigated the interactions of solitary waves with a vertical cylinder by the finite element method. Recently, Zhong and Wang (2008) developed a time-accurate stabilized finite element model to investigate the diffraction processes of both weakly nonlinear and weakly dispersive waves and fully nonlinear and weakly dispersive waves by cylindrical structures. Other fully three-dimensional models have also been constructed to simulate the interaction between waves and structures. Yang and Ertekin

(1992) applied the boundary element method to calculate the solitary wave induced forces on a vertical cylinder. Simulations of the interaction between a vertical cylinder and steep waves were carried out by using a three-dimensional finite element model (Ma et al., 2001; Kim et al., 2006). Later, Eatock Taylor et al. (2008) combined the boundary element and finite element methods to perform numerical wave tank simulation. Ai and Jin (2010) applied an efficient non-hydrostatic finite volume model to simulate solitary waves interacting with a vertical cylinder, an array of four cylinders, and a submerged structure. Choi et al. (2011) solved the three-dimensional Navier-Stokes equations by means of a finite difference method to model the run-up of a cnoidal wave around a fixed bottom mounted cylinder. Experimentally, Yates and Wang (1994) provided a series of measurements of free-surface elevations around a vertical cylinder and induced forces for the case of a solitary wave scattered by a vertical cylinder.

1.2 Water waves interacting with floating structures

In recent years, construction of floating structures in offshore applications has been expanded considerably. However, the studies of wave interaction with floating structures have been very limited, especially considering nonlinear shallow-water waves. The analytical formulations to predict wave forces on floating structures can be found in Miles and Gilbert (1968), Garrett (1971), Yeung (1981), Mavrakoos (1985), and Sabuncu and Gören (1985). Yu and Chwang (1993) and Chwang and Wu (1994) used a linear wave theory and an eigenfunction expansion method to study the scattering of water waves by a horizontal submerged disk. The eigenfunction expansion method was also applied to investigate the wave interaction with floating structures (Drimer et al. 1992; Wu et al.,1995; William et al., 2000). For an array of floating cylinders, three-

dimensional analytical methods have been developed to solve the wave radiation and diffraction problems (Kagemoto et al., 1986; Kim, 1993; Yilmaz et al., 1998, 2001; Siddorn and Eatock Taylor, 2008; Zeng and Tang, 2013). Zheng and Zheng (2015) applied the concepts of the analytical solutions of an array of floating cylinders with eigenfunction expansion matching method to predict the wave diffraction by a truncated cylinder in front of a wall.

Numerically solving three-dimensional governing equations directly with fully nonlinear boundary conditions may be utilized to investigate the impinging of waves on floating structures. The boundary element method with its computational elements arranged along the boundary surfaces is an approach that has been applied by researchers to simulate the interaction of waves and floating structures. Isaacson (1982) solved the integral equations of the boundary element approach based on the Green's function theorem to obtain velocity potentials of the fluid domain. He also computed the wave forces acting on the fixed and floating structures. Isaacson and Cheung (1990, 1991, and 1992) modified the time-stepping procedure to solve wave diffraction around the two-dimensional and three-dimensional body problems. A higher-order boundary element model with the mixed Eulerian-Lagrangian method was developed to simulate nonlinear wave-wave and wave-body interactions (Kim et al., 1998; Xue et al., 2001; Lue et al., 2001). Boo (2002) used the time-domain higher-order boundary element method to simulate linear and nonlinear irregular waves and their interactions with a vertical truncated circular cylinder. Using different time domain scheme, Koo and Kim (2007) utilized Mixed Eulerian-Lagrangian numerical method and Runge-kutta fourth-order time integration techniques on the free surface to study the problem of two-dimensional fully

nonlinear waves encountering a surface-piercing body. Bai and Taylor (2009) later applied the higher-order boundary element method to simulate fully nonlinear water waves interacting with fixed and floating flared structures.

In addition to the boundary element method, other discretization methods, such as finite difference and finite element methods, have also been used to develop models to study wave and floating structure interaction problems. Park et al. (2001) presented a numerical wave tank study on nonlinear waves interacting with a stationary and vertically truncated circular cylinder by a finite difference based Navier-Stokes equations solver. Lin (2006) also solved the Navier-Stokes equations with the finite difference method and multiple-layered σ-coordinate transformation technique to simulate the transformation of solitary waves by a two-dimensional rectangular floating structure. Later, Kang et al. (2015) extended the multiple-layered σ-coordinate transformation technique to study the problems of wave interacting with a submerged three-dimensional vertical circular cylinder. By applying the finite element method, Zhu et al. (2001) solved the Navier-Stokes equations to simulate free-surface waves over submerged horizontal cylinders. Wang et al. (2007) investigated the interaction between nonlinear waves and non-wall-sided three-dimensional structures. Sun et al. (2015) applied the higher-order finite element method to simulate a solitary wave impacting on a two-dimensional structure. Recently, Lu and Wang (2015) developed an integrated analytical-numerical approach for modeling a solitary wave propagating past a fixed two-dimensional floating body. A series of experimental measurements in terms of reflected and transmitted wave elevations have also been conducted by Lu and Wang (2015) to compare to their model solutions.

1.3 Water wave propagation in a curved channel

As curved channels are easily observed in nature and in engineering applications, the phenomenon of wave propagation in curved channels is also an important topic to study. In past decades, only very limited researches focused on investigating the nonlinear shallow-water waves propagating in curved channels. Rostafinski (1972) derived a two-dimensional analytical solution by using linear wave equations for the propagation of long acoustic waves in curved ducts. Katopodes and Wu (1987) developed a finite element model with a rectangular grid system to simulate a solitary wave traveling through a 90 degree sharp-cornered channel. However, it is difficult to describe non-orthogonal boundaries, like curved channels, by using the rectangular orthogonal grid system for numerical simulations. For this reason, coordinate transformation systems have been developed and applied in different cases of non-orthogonal boundaries such as breakwaters, shorelines, and riverbanks (Wang, 1994; Shi, 2005; Wood and Wang, 2015). Kirby et al. (1994) applied small- and large-angle parabolic approximations in conformally mapped coordinate systems to investigate linear waves propagating in a curved water channel. For nonlinear wave modeling, Boussinesq equations with coordinate transformations can provide solutions to describe nonlinear long waves propagating in variable topographies. Shi et al. (1996, 1998) adopted the boundary-fitted curvilinear finite difference scheme developed by Wang et al. (1992) to solve the generalized Boussinesq equations (Wu, 1981) for modeling solitary waves propagating through a sharp-cornered channel bend and a smoothly curved channel bend. Then, the higher-order Boussinesq equations were developed and applied with the curvilinear coordinate transformation system to simulate waves propagating through a circular

channel (Yuhi et al., 2000; Shi et al., 2001; Fang, 2012). In addition, the boundary-fitted curvilinear transformations were combined with the solvers of the Navier-Stokes equations to investigate nonlinear waves traveling in a curved channel (Choi et al., 2011; Choi and Yuan, 2012). Different from using the boundary-fitted curvilinear transformation technique, Nachbin and Da Silva Simões (2012) applied the Schwarz-Christoffel transformation into the generalized Boussinesq equations to study the interaction of a solitary wave with a sharp-cornered and a smoothly curved 90 degree bend.

Solving equations in an unstructured grid system is another way to model wave propagation in a domain with non-orthogonal boundaries. Löhner et al. (1984) developed a finite element model for a computational domain that is constructed by the linear triangular elements to simulate two-dimensional oblique waves passing through a channel with a sudden contraction of width. Asmar and Nwogu (2007) solved Boussinesq-type equations by the finite volume method with irregular triangular grids to carry out the simulations of a solitary wave traveling in a curved channel.

1.4 Outline of the Dissertation

It is noticed from the literature review that the applications of Boussinesq models are limited to the problems associated with the interaction between three-dimensional nonlinear shallow-water waves and bottom mounted and surface piercing structures. For the floating bodies, the vertically integrated (or averaged) Boussinesq models face the difficulty to cover the solutions for the regions beneath the bodies. The development of a fully three-dimensional modeling approach becomes necessary to investigate the evolution of waves scattered by three-dimensional floating bodies. In addition, the study

of nonlinear shallow-water waves interacting with a floating structure by solving the three-dimensional governing equations has brought only very limited attention, especially considering solitary wave interactions with floating structures. Thus, the aim of this study is to develop a three-dimensional fully nonlinear wave model by solving the three-dimensional Laplace equation and specified boundary conditions on the free surface and structural surface in order to investigate the interaction process between nonlinear shallow-water waves and cylindrical structures.

The general introduction, literature review, and the outline of the dissertation are introduced in Chapter 1. Chapter 2 presents the theoretical development of the present three-dimensional fully nonlinear wave model. The three-dimensional governing equation, Laplace equation, and the various boundary conditions, including the kinematic and dynamic boundary conditions, the open boundary conditions, and solid wall boundary conditions, are formulated in this chapter. Additionally, the wave considered in this study is a Boussinesq type solitary wave, where the analytical expressions of the wave elevation and velocity potential are available to be used as the incident wave conditions. In order to have the computational grids fitting closely to the irregular and curved boundaries, such as a circular cylinder surface, and the time-varying free surface for the numerical advantage, the transient three-dimensional curvilinear coordinate transformation technique is adopted to convert the original governing equations and boundary conditions in Cartesian coordinates into the curvilinear coordinate based equations. The derivations of the transformed equations are also included in Chapter 2.

Chapter 3 describes a finite difference formulation for the governing equation and a mixed explicit-implicit scheme for solving nonlinear free-surface boundary conditions.

Moreover, numerically the multiple grid systems with curvilinear grid points covering the regions close to or beneath the structures and separating from those regular grids for regions far outside of the structures are used. This requires an iteration procedure to generate consistent and converged results at grid points in the overlapped regions. Once the three-dimensional velocity potentials and free-surface elevation around the cylindrical surface are determined, the pressure distribution on the cylinder can be computed by means of the Bernoulli equation. Accordingly, the total forces acting on the cylinder can be calculated by integrating the pressure. In order to validate the stability and accuracy of the present three-dimensional fully nonlinear model, modeling a solitary wave freely propagating in a long fluid domain was performed for studying the effects of grid size and time step. Another case study, a solitary wave propagating through a 180° curved channel, was also carried out to demonstrate the capability of the present model to simulate propagation of waves in a channel of arbitrary shapes.

Chapter 4 and Chapter 5 present the application studies of the interaction between solitary waves and structures. In Chapter 4, the present three-dimensional fully nonlinear wave model simulates a solitary wave interacting with a bottom mounted and surface piercing vertical cylinder. The results showing the time variation of the diffracted wave pattern and hydrodynamic forces acting on the cylinder considered in the simulation are presented. The model performance is examined by comparing the time-varying wave elevations at selected locations with those obtained from Boussinesq model and experimental measurements (Yates and Wang, 1994). In Chapter 5, in order to show the capability of the present three-dimensional fully nonlinear wave model in solving more complicated wave-structure interaction problems, the results from simulating the

propagation of a solitary wave and its interaction with a partially immersed and fixed floating circular cylinder are presented. In addition, the laboratory experiments of a solitary wave interacting with a partially immersed and fixed floating circular cylinder were conducted for verifying the numerical results obtained from the present model. The detailed data recording and experimental setup including the dimensions and locations of the wave gauges, the wavemaker, and the circular cylinder are described. The evolution of the wave diffraction process and wave induced hydrodynamic forces along the horizontal and vertical directions for the selected cases are also presented in this chapter.

Finally, the key results and conclusions of the present three-dimensional fully nonlinear modeling studies are summarized in Chapter 6. This chapter also discusses the future study and potential applications of the developed wave model.

Chapter 2

Theoretical Model for Fully Nonlinear Water Waves

There are many approaches based on general Boussinesq model to simulate the long wave propagate. However, the vertical averaged Boussinesq model is hard to describe the change in the vertical direction while the velocity potentials of each layer are different such as a solitary wave passes through a floating structure. It is hard for using vertical averaged method to solve the velocity potentials underneath the floating structure. Moreover, the Boussinesq model is derived for weakly-nonlinear long wave. In order to simulate the fully nonlinear long wave interaction with structures, especially with a floating structure, the equations need to suit for fully three-dimension and fully non-linear wave. The curvilinear coordinate transformation which can describe the boundaries fittingly is also applied to this model. The equations used for developing three-dimension fully non-linear solitary wave model and the curvilinear coordinate transformation in this study will be presented in the following sections.

2.1 Governing Equations

In this study, simulations of solitary waves interaction with a full (bottom mounted and surface piercing) vertical cylinder or a partially immersed and fixed floating cylinder were carried out using a developed three-dimensional fully nonlinear wave model. For the convenience of model development and results presentation, all physical variables are nondimensionalized according to h_0^*, $\sqrt{h_0^*/g}$, and $\sqrt{gh_0^*}$ as respectively the length, time, and velocity scales. We have

$$(x, y, z, \zeta, h) = \frac{\left(x^*, y^*, z^*, \zeta^*, h^*\right)}{h_0^*},$$

$$t = \frac{t^*}{\sqrt{h_0^*/g}},$$

$$(u, v, w) = \frac{\left(u^*, v^*, w^*\right)}{\sqrt{gh_0^*}},$$

$$\phi = \frac{\phi^*}{ch_0^*} = \frac{\phi^*}{h_0^*\sqrt{gh_0^*}} \qquad (2\text{-}1)$$

where a variable with superscript "*" represent the dimensional form of that variable. Here, ϕ = velocity potential and (u, v, w) = three-dimensional velocity vector. Sketches showing a solitary wave encountering a full vertical cylinder and a partially immersed one are presented in Figures, 2-1(a) and 2-1(b), respectively. The Cartesian coordinates were chosen as the original coordinate system to formulate the governing equation and the boundary conditions. As shown in Figure 2-1, the *x*- and *y*- axes represent the two horizontal coordinates while *z*-axis points upward with z =0 being set at the level of the undisturbed free surface. $z = \zeta(x, y, t)$ denotes the displacement of the free surface from the undisturbed water level and t = time The bottom of flow domain is horizontal and is placed at $z^* = -h_0^*$ or in dimensionless form $z = -1$, where h_0^* is a constant water depth. It is assumed that the fluid is incompressible and inviscid and the motion irrotational. The velocity potential of the wave motion satisfies the Laplace equation, which is described in dimensionless form as

$$\nabla^2\phi = 0\,, \qquad \text{at } -h \le z \le \zeta\,, \tag{2- 2}$$

where $\nabla = (\partial/\partial x, \partial/\partial y, \partial/\partial z)$ is a vector differential operator. The velocity components *u*, *v*, and *w* can be related to the velocity potential as

$$u = \partial\phi/\partial x\,, \tag{2- 3}$$

$$v = \partial\phi/\partial y\,, \text{ and} \tag{2- 4}$$

$$w = \partial\phi/\partial z\,. \tag{2- 5}$$

In addition to the governing equation (2- 2), the boundary conditions at the free surface, the bottom boundary, the rigid side wall and structural boundaries, and the upstream and downstream open boundaries need to be formulated to complete the required equations for the development of a three-dimensional nonlinear wave model that can be used to simulate the propagation of nonlinear long waves and their interactions with cylindrical structures. Those boundary equations are addressed in Section 2.2.

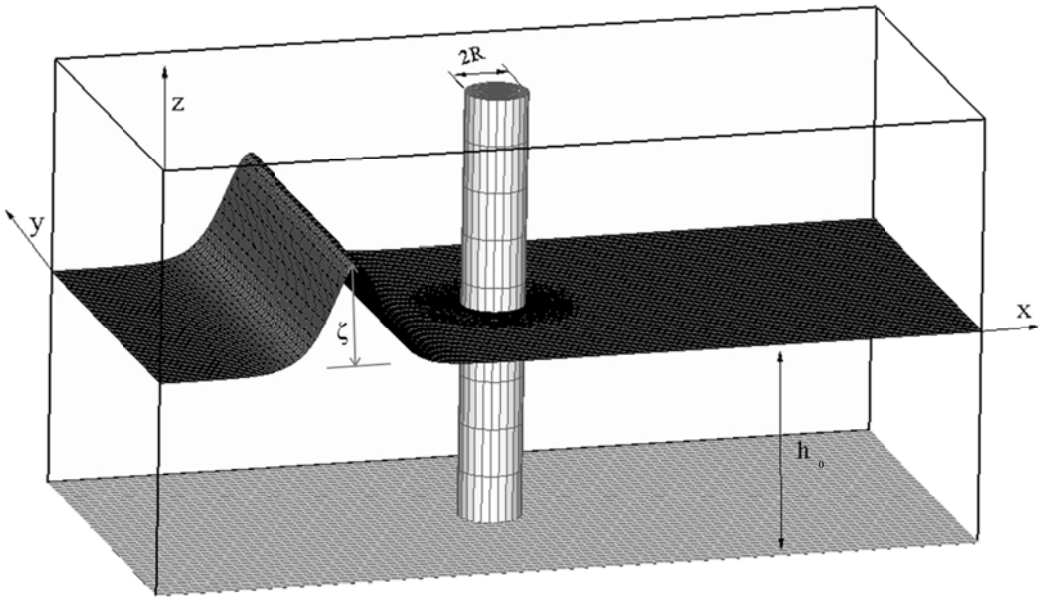

(a)

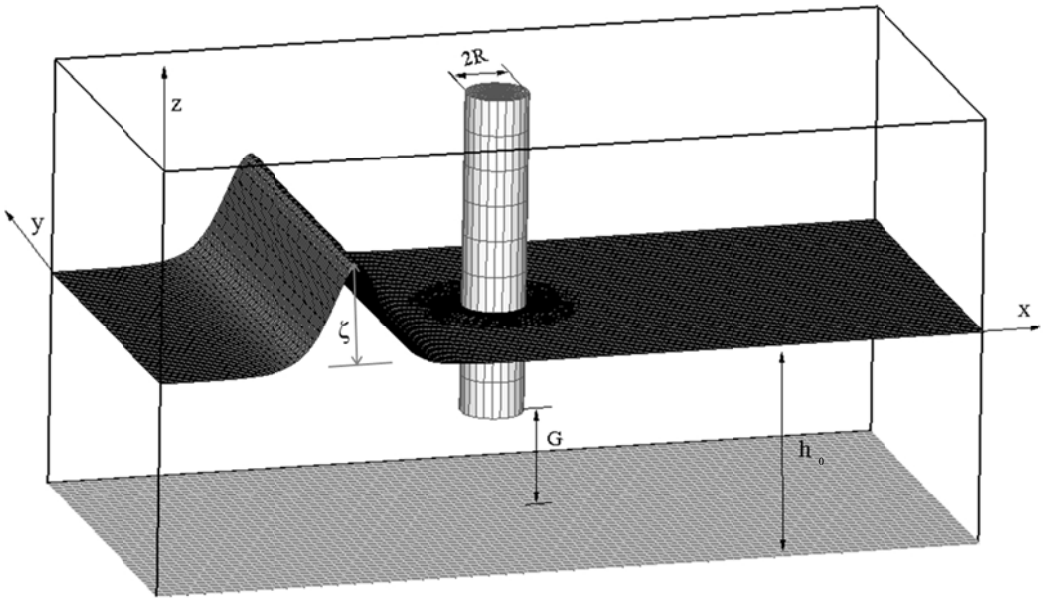

(b)

Figure 2- 1 Coordinate system for the description of the governing equations: (a) bottom mounted and surface piercing vertical cylinder, and (b) fixed floating cylinder

2.2 Boundary Conditions

As described above, providing appropriate boundary conditions is essential for the development of stable and accurate wave simulation model for the present wave-structure interaction study. The boundary conditions for each specified boundary are introduced and formulated in the following subsections.

2.2.1 Free-surface boundary conditions

The kinematic property of the free surface indicates that once a fluid particle is on the free surface, it remains on the free surface and its normal velocity follows the normal velocity of the free surface. Defining the free surface function as $F(x, y, z, t) = z - \zeta(x, y, t)$, the condition suggests that the total derivative of the surface function with respect to time is equal to zero there. Thus, the kinematic free-surface boundary condition (KFSBC) can be written as

$$w = \zeta_t + u\zeta_x + v\zeta_y \qquad \text{at } z = \zeta(x, y, t), \tag{2- 6}$$

where the subscripts denote the partial derivatives.

Moreover, the pressure is maintained as a constant at the free surface. The Bernoulli equation is applied at the free surface as the dynamic free-surface boundary condition (DFSBC), which is described as

$$\phi_t + \frac{1}{2}(u^2 + v^2 + w^2) + \zeta + p = 0 \quad \text{at } z = \zeta(x, y, t), \tag{2- 7}$$

where p is a pressure on the surface. Let p = 0, the DFSBC is reduced to

$$\phi_t + \frac{1}{2}(u^2 + v^2 + w^2) + \zeta = 0 \quad \text{at } z = \zeta(x, y, t). \tag{2- 8}$$

2.2.2 Bottom boundary condition

The no fluid penetrating at the flat solid bottom boundary leads to the following bottom boundary condition

$$\frac{\partial \phi}{\partial z} = 0 \quad \text{at } z = -1. \tag{2- 9}$$

2.2.3 Solid side wall and structural boundary conditions

For modeling the interactions between nonlinear waves and cylindrical structures in a domain of wave channel with two side walls, the boundary conditions on the rigid side walls and the circular cylinder surface follow that the normal fluid velocity vanishes there. We have

$$\frac{\partial \phi}{\partial n} = 0, \tag{2- 10}$$

where n is the unit normal direction to a solid boundary surface.

2.2.4 Open boundary conditions

The open boundary conditions control the waves propagating out of the computational domain without the adverse impact from wave reflection. The Orlanski type simple wave equations used as the open boundary conditions for simulating propagation of nonlinear long waves were firstly applied by Wu and Wu (1982). The equations in dimensionless forms for velocity potential and wave elevation are given as

$$\phi_t \pm \phi_x = 0 \text{ and} \tag{2- 11a}$$

$$\zeta_t \pm \zeta_x = 0, \tag{2- 11a}$$

where the + or – sign is referenced according to the downstream or upstream boundary. The above described open boundary conditions have been proven to be able to propagate the primary and scattered waves out of the computational domain effectively, including the cases of modeling scattering of a solitary wave by a vertical cylinder (Wang el al., 1992), by a breakwater (Wang, 1993) and the interactions of cnoidal waves with cylinder arrays (Wang and Ren, 1999). Later, the boundary conditions in equations (2- 11a) and (2- 11a) were extended by Chang and Wang (2011) in their modeling study of generation of three-dimensional water waves by a submerged moving object. The extended open boundary conditions for the downstream boundary are given as

$$\phi_t + \sqrt{(1+\zeta)}\phi_x = 0 \text{ and} \tag{2- 12a}$$

$$\zeta_t + \sqrt{(1+\zeta)}\zeta_x = 0 . \tag{2- 12a}$$

The wave elevation effect is included in Equations (2- 12a) and (2- 12a). The upstream open boundary conditions that control the transmission of the scattered or reflected waves out of the upstream boundary are expressed as

$$\phi_t - \sqrt{(1+\zeta)}\phi_x = 0 \text{ and} \tag{2- 13a}$$

$$\zeta_t - \sqrt{(1+\zeta)}\,\zeta_x = 0\,. \tag{2- 13a}$$

2.3 Initial Condition for Incident Solitary Waves

As a solitary wave has a unique property of cohesive balance between the nonlinear and dispersive effects and can be effectively applied to reveal the nonlinear behavior of wave-structure interaction, it is selected, in this study, a solitary wave to be the initial and incident wave condition.

An up to the second-order solitary wave solution as derived by Schember (1982) is used. This second-order solitary wave solutions in term of wave elevation ζ and vertically averaged (layer-mean) velocity potential $\bar{\phi}$ are expressed as

$$\zeta = \frac{\alpha}{1+\alpha}[\text{sech}^2\, k(x - ct - x_0) + \alpha\text{sech}^2\, k(x - ct - x_0)] \text{ and} \tag{2- 14}$$

$$\bar{\phi} = \left(\frac{4}{3}\alpha\right)^{1/2} \tanh k(x - ct - x_0), \tag{2- 15}$$

where

$$k = \left[\frac{3\alpha}{4(1+\alpha)}\right]^{1/2} \text{ and} \tag{2- 16}$$

$$c = (1+\alpha)^{1/2}\,, \tag{2- 17}$$

α = dimensionless wave amplitude, and the layer-mean velocity potential $\bar{\phi} = [\int_{-1}^{\zeta} \phi(x,z,t)dz]/(1+\zeta)$.

In order to extend the $\bar{\phi}$ equation in (2- 15) to the expression of three-dimensional velocity potential, a relationship between the original velocity potential $\phi(x, y, z, t)$ and the layer-mean velocity potential $\bar{\phi}(x, y, t)$ as given in Wu (1981) and Wang et al. (1992)

$$\phi = \bar{\phi} - \alpha\left(\frac{1}{3} + z + \frac{z^2}{2}\right)\nabla^2\bar{\phi} + O(\varepsilon^5), \tag{2- 18}$$

is applied. The neglected error terms in Eq. (2- 18) are up to $O(\varepsilon^5)$, where $\varepsilon = h_0/\lambda$. The three-dimensional velocity potential for an incident solitary wave can be derived by substituting $\bar{\phi}$ from Eq. (2- 15) into Eq. (2- 18) as

$$\phi = \left(\frac{4}{3}\alpha\right)^{1/2} \tanh k(x - ct - x_0) - \alpha\left(\frac{1}{3} + z + \frac{z^2}{2}\right)\left(\frac{4}{3}\alpha\right)^{1/2} (2k^2) \tanh k(x - ct - x_0)\,[\tanh^2 k(x - ct - x_0) - 1]\,. \tag{2- 19}$$

Equation (2- 19) can be used as an initial wave condition by setting $t = 0$ and letting the peak of a specified solitary wave be situated at $x = x_0$. For modeling wave and cylinder interaction, the initial wave peak location is selected to be sufficiently far away from the cylinder (Wang et al., 1992). This will allow the inputted incident waves from Eqs. (2- 14) and (2- 19) to gradually transition into an initial solitary wave that satisfies the derived three-dimensional model equations before it encountering a vertical cylinder.

2.4 Forces on cylinders

Once the free-surface elevation and velocity potentials are determined from solving the model equations, the wave-induced hydrodynamic force F acting on either a

bottom mounted cylinder or a floating cylinder can be calculated by integrating the pressure on the cylinder surface, where the pressure, p, is computed from the Bernoulli equation

$$p = -z - \phi_t - \frac{1}{2}\left(\phi_x^2 + \phi_y^2 + \phi_z^2\right) . \tag{2- 20}$$

For the convenience of force comparisons with other published results for the cases of a bottom mounted and surface piercing cylinder, the inline force coefficient $C_{fH}(t)$ is defined as the integral of the x-direction component of the excess pressure $(p + z)$ over the surface of the cylinder in contact with the fluid. The form of the force coefficient is

$$C_{fH}(t) = \frac{F \cdot e_x}{\rho g h_0^2 R} = -2\int_0^{\pi} d\theta \int_{-h}^{\zeta} (p + z)\cos\theta \, dz , \tag{2- 21}$$

where e_x = the unit normal direction along the x-axis, R is the radius of a cylinder considered in the study, and θ is the angle of angular direction measured from the x-axis.

For the partially submerged floating cylinder cases, the hydrodynamic forces include two parts: horizontal force and vertical force. The horizontal (inline) force coefficient $C_{fH}(t)$ is similar to Equation (2- 21), but integrated only the submerged portion of the cylindrical surface. The vertical force coefficient $C_{fV}(t)$, which is acting on the bottom of the floating cylinder, is computed according to

$$C_{fV}(t) = \frac{F \cdot e_z}{\rho g h_0 R^2} = \iint (p + z) dA , \tag{2- 22}$$

where e_z = the unit normal direction along the z-axis and dA is a small incremental area of the bottom surface.

2.5 Three-Dimensional Transient Curvilinear Coordinate Transformation

The traditional Cartesian coordinates are convenient to define with rectangular grids a regular flow domain with straight-line boundaries. However, when complex and curved boundaries exist in the physical domain, the Cartesian coordinates based finite difference models are expected to face the difficulty in representing the irregular boundaries with rectangular grids and the associated numerical challenge in computing the values of physical variables there. In order to facilitate the application of the boundary conditions on the irregular and curved boundaries (e.g. cylinder surface) and to represent the selected structural surface in the computational domain well, the boundary-fitted (or curvilinear) coordinate transformation technique is applied in the present modeling study.

The curvilinear coordinate transformation technique was introduced by Thompson et al. (1974) and has been extended to the modeling studies of solitary waves interactions with a bottom mounted cylinder (Wang et al., 1992) or cylinder arrays (Jiang and Wang, 1994; Wang and Ren, 1999) and the generation of fully nonlinear waves by a submerged moving object (Chang and Wang, 2011). In this study, a fully 3D transient curvilinear coordinate transformation is utilized to transform the transient rectangular grids in Cartesian coordinates $(x, y, z; t)$ into transient curvilinear coordinates $(\xi, \eta, \gamma; \tau)$ for multi-grid modeling application. The transient effect on the computational grids is limited to the vertical coordinate. This indicates that the physical z coordinates vary at each time level according to the updated vertical domain at a given location. The transformation of the governing equations and the boundary conditions are summarized in the following.

The spatial derivatives of velocity potential ϕ with respect to ξ, η, and γ are

$$\frac{\partial \phi}{\partial \xi} = \frac{\partial \phi}{\partial x}\frac{\partial x}{\partial \xi} + \frac{\partial \phi}{\partial y}\frac{\partial y}{\partial \xi} + \frac{\partial \phi}{\partial z}\frac{\partial z}{\partial \xi} \quad , \tag{2- 23}$$

$$\frac{\partial \phi}{\partial \eta} = \frac{\partial \phi}{\partial x}\frac{\partial x}{\partial \eta} + \frac{\partial \phi}{\partial y}\frac{\partial y}{\partial \eta} + \frac{\partial \phi}{\partial z}\frac{\partial z}{\partial \eta} \quad \text{, and} \tag{2- 24}$$

$$\frac{\partial \phi}{\partial \gamma} = \frac{\partial \phi}{\partial x}\frac{\partial x}{\partial \gamma} + \frac{\partial \phi}{\partial y}\frac{\partial y}{\partial \gamma} + \frac{\partial \phi}{\partial z}\frac{\partial z}{\partial \gamma} \quad . \tag{2- 25}$$

Solving the above three equations, we have

$$\frac{\partial \phi}{\partial x} = \frac{\mathrm{y}_\eta z_\gamma \phi_\xi + y_\xi z_\eta \phi_\gamma - z_\xi y_\eta \phi_\gamma - y_\xi z_\gamma \phi_\eta}{J} \quad , \tag{2- 26}$$

$$\frac{\partial \phi}{\partial y} = \frac{x_\xi z_\gamma \phi_\eta + x_\eta z_\xi \phi_\gamma - x_\eta z_\gamma \phi_\xi - x_\xi z_\eta \phi_\gamma}{J} \quad \text{, and} \tag{2- 27}$$

$$\frac{\partial \phi}{\partial z} = \frac{x_\xi y_\eta \phi_\gamma - x_\eta y_\xi \phi_\gamma}{J} \quad , \tag{2- 28}$$

where $J = \left(x_\xi y_\eta - x_\eta y_\xi\right) z_\gamma$ is the determinant of Jacobian matrix. For the time derivative, it can be shown

$$\frac{\partial \phi}{\partial t} = \frac{\partial \phi}{\partial \tau} - \frac{\partial \phi}{\partial z}\frac{\partial z}{\partial \tau} \quad . \tag{2- 29}$$

The terms of $\partial\phi/\partial x$, $\partial\phi/\partial y$, and $\partial\phi/\partial z$ in Eqs. (2- 26)- (2- 28) are substituted into the Laplace equation [Eq. (2- 2)] in Cartesian coordinates

$$\frac{\partial^2 \phi}{\partial x^2} + \frac{\partial^2 \phi}{\partial y^2} + \frac{\partial^2 \phi}{\partial z^2} = 0 \ , \qquad \text{(2- 30a)}$$

to give

$$\frac{1}{J^2}\left\{\left(x_\eta^2 + y_\eta^2\right) z_\gamma^2 \phi_{\xi\xi} + \left[-2\left(x_\eta^2 + y_\eta^2\right) z_\xi z_\gamma + 2\left(x_\xi x_\eta + y_\xi y_\eta\right) z_\eta z_\gamma\right]\phi_{\xi\gamma} - 2\left(x_\xi x_\eta + y_\xi y_\eta\right) z_\gamma^2 \phi_{\xi\eta}\right.$$
$$+ \left[2\left(x_\xi x_\eta + y_\xi y_\eta\right) z_\xi z_\gamma - 2\left(x_\xi^2 + y_\xi^2\right) z_\eta z_\gamma\right]\phi_{\eta\gamma} + \left(x_\xi^2 + y_\xi^2\right) z_\gamma^2 \phi_{\eta\eta} + \left[\left(y_\xi z_\eta - y_\eta z_\xi\right)^2 + \left(x_\eta z_\xi - x_\xi z_\eta\right)^2\right.$$
$$\left.\left. + \left(x_\xi y_\eta - x_\eta y_\xi\right)^2\right]\phi_{\gamma\gamma}\right\} + \frac{1}{J^3}\left\{\left[y_\xi z_\gamma^3 \phi_\eta - y_\eta z_\gamma^3 \phi_\xi + \left(y_\eta z_\xi z_\gamma^2 - y_\xi z_\eta z_\gamma^2\right)\phi_\gamma\right]\left[\left(x_\eta^2 + y_\eta^2\right) x_{\xi\xi}\right.\right.$$
$$- 2\left(x_\xi x_\eta + y_\xi y_\eta\right) x_{\xi\eta} + \left(x_\xi^2 + y_\xi^2\right) x_{\eta\eta}\Big] + \left[x_\eta z_\gamma^3 \phi_\xi - x_\xi z_\gamma^3 \phi_\eta + \left(x_\xi z_\eta z_\gamma^2 - x_\eta z_\xi z_\gamma^2\right)\phi_\gamma\right]\left[\left(x_\eta^2 + y_\eta^2\right) y_{\xi\xi}\right.$$
$$- 2\left(x_\xi x_\eta + y_\xi y_\eta\right) y_{\xi\eta} + \left(x_\xi^2 + y_\xi^2\right) y_{\eta\eta}\Big] + \left(x_\eta y_\xi - x_\xi y_\eta\right)\Big[2\left(x_\xi x_\eta + y_\xi y_\eta\right) z_\xi z_\gamma z_{\gamma\eta}$$
$$- 2\left(x_\xi^2 + y_\xi^2\right) z_\eta z_\gamma z_{\gamma\eta} + 2\left(x_\xi x_\eta + y_\xi y_\eta\right) z_\eta z_\gamma z_{\gamma\xi} - 2\left(x_\eta^2 + y_\eta^2\right) z_\xi z_\gamma z_{\gamma\xi} + \left(x_\eta^2 + y_\eta^2\right) z_\gamma^2 z_{\xi\xi}$$
$$- 2\left(x_\xi x_\eta + y_\xi y_\eta\right) z_\gamma^2 z_{\xi\eta} + \left(x_\xi^2 + y_\xi^2\right) z_\gamma^2 z_{\eta\eta} + \left(x_\xi^2 z_\eta^2 + y_\xi^2 z_\eta^2 + x_\xi^2 y_\eta^2\right) z_{\gamma\gamma} - 2\left(x_\xi x_\eta z_\xi z_\eta + y_\xi y_\eta z_\xi z_\eta\right.$$
$$\left.\left.\left. + x_\xi x_\eta y_\xi y_\eta\right) z_{\gamma\gamma} + \left(x_\eta^2 z_\xi^2 + y_\eta^2 z_\xi^2 + x_\eta^2 y_\xi^2\right) z_{\gamma\gamma}\right]\phi_\gamma\right\}.$$

(2- 30a)

Let

$$g_{11} = \frac{\left(x_\eta^2 + y_\eta^2\right) z_\gamma^2}{J^2}, \qquad \text{(2- 31)}$$

$$g_{12} = \frac{-2\left(x_\xi x_\eta + y_\xi y_\eta\right) z_\gamma^2}{J^2} \ , \qquad \text{(2- 32)}$$

$$g_{13} = \frac{2\left(x_\xi x_\eta + y_\xi y_\eta\right) z_\eta z_\gamma - 2\left(x_\eta^2 + y_\eta^2\right) z_\xi z_\gamma}{J^2} \ , \qquad \text{(2- 33)}$$

$$g_{22} = \frac{\left(x_\xi^2 + y_\xi^2\right) z_\gamma^2}{J^2} \ , \tag{2- 34}$$

$$g_{23} = \frac{2\left(x_\xi x_\eta + y_\xi y_\eta\right) z_\xi z_\gamma - 2\left(x_\xi^2 + y_\xi^2\right) z_\eta z_\gamma}{J^2} \ , \tag{2- 35}$$

$$g_{33} = \frac{\left(y_\xi z_\eta - y_\eta z_\xi\right)^2 + \left(x_\eta z_\xi - x_\xi z_\eta\right)^2 + \left(x_\xi y_\eta - x_\eta y_\xi\right)^2}{J^2} \ , \tag{2- 36}$$

$$f_1 = \frac{\left(x_\eta Dy - y_\eta Dx\right) z_\gamma^3}{J^3} \ , \tag{2- 37}$$

$$f_2 = \frac{\left(y_\xi Dx - x_\xi Dy\right) z_\gamma^3}{J^3} \ , \tag{2- 38}$$

$$f_3 = \frac{(gx + gy)}{J^3} + \frac{\left(x_\eta y_\xi - x_\xi y_\eta\right)\left(g_{23} z_{\gamma\eta} + g_{13} z_{\gamma\xi} + g_{11} z_{\xi\xi} + g_{12} z_{\xi\eta} + g_{22} z_{\eta\eta} + g_{33} z_{\gamma\gamma}\right)}{J} \ ,$$

(2- 39)

$$gx = \left(y_\eta z_\xi z_\gamma^2 - y_\xi z_\eta z_\gamma^2\right) Dx \ , \tag{2- 40}$$

$$gy = \left(x_\xi z_\eta z_\gamma^2 - x_\eta z_\xi z_\gamma^2\right) Dy \ , \tag{2- 41}$$

$$Dx = \left(x_\eta^2 + y_\eta^2\right) x_{\xi\xi} - 2\left(x_\xi x_\eta + y_\xi y_\eta\right) x_{\xi\eta} + \left(x_\xi^2 + y_\xi^2\right) x_{\eta\eta} \ , \text{ and} \tag{2- 42}$$

$$Dy = \left(x_\eta^2 + y_\eta^2\right) y_{\xi\xi} - 2\left(x_\xi x_\eta + y_\xi y_\eta\right) y_{\xi\eta} + \left(x_\xi^2 + y_\xi^2\right) y_{\eta\eta} \ . \tag{2- 43}$$

The governing equation Eq. (2- 30a) in the transformed coordinates can be reduced to

$$g_{11}\phi_{\xi\xi} + g_{13}\phi_{\xi\gamma} + g_{12}\phi_{\xi\eta} + g_{23}\phi_{\eta\gamma} + g_{22}\phi_{\eta\eta} + g_{33}\phi_{\gamma\gamma} + f_1\phi_\xi + f_2\phi_\eta + f_3\phi_\gamma = 0 \ . \tag{2- 44}$$

The fluid velocity can be calculated from velocity potential, namely (2- 3) to (2- 5) in the transformed domain are

$$u = \phi_x = \left(y_\eta z_\gamma \phi_\xi + y_\xi z_\eta \phi_\gamma - z_\xi y_\eta \phi_\gamma - y_\xi z_\gamma \phi_\eta\right)/J \ , \tag{2- 45}$$

$$v = \phi_y = \left(x_\xi z_\gamma \phi_\eta + x_\eta z_\xi \phi_\gamma - x_\eta z_\gamma \phi_\xi - x_\xi z_\eta \phi_\gamma\right)/J \ , \text{ and} \tag{2- 46}$$

$$w = \phi_z = \left(x_\xi y_\eta \phi_\gamma - y_\xi x_\eta \phi_\gamma\right)/J \ . \tag{2- 47}$$

The free-surface boundary conditions described in Eqs. (2- 6) and (2- 8) are transformed as

$$\zeta_\tau = w - u\left(\frac{y_\eta \zeta_\xi - y_\xi \zeta_\eta}{x_\xi y_\eta - x_\eta y_\xi}\right) - v\left(\frac{x_\xi \zeta_\eta - x_\eta \zeta_\xi}{x_\xi y_\eta - x_\eta y_\xi}\right) \text{ and} \tag{2- 48}$$

$$\phi_\tau - w\zeta_\tau + \frac{1}{2}(u^2 + v^2 + w^2) + \zeta = 0 \ . \tag{2- 49}$$

where *u, v,* and *w* are three-dimensional velocity components given in Eqs. (2- 45), (2-46), and (2- 47) respectively. Similarly, the open boundary conditions as given in Eqs. (2-11a) and (2- 12a) are reformulated in the transformed coordinate system to have

$$\phi_\tau - w\zeta_\tau \pm \sqrt{(1+\zeta)}\left(\phi_\xi / x_\xi - \phi_\gamma z_\xi / x_\xi z_\gamma\right) = 0 \text{ and} \tag{2- 50}$$

$$\zeta_\tau \pm \sqrt{(1+\zeta)}\left(\zeta_\xi / x_\xi\right) = 0 . \tag{2- 51}$$

Chapter 3

Numerical Method

The numerical scheme and procedure of solving the governing equation and boundary conditions formulated in Chapter 2 are described in this chapter. Numerically, the finite difference scheme is adopted for the development of the three-dimensional nonlinear wave model. The technique of multi-grid system is also used to handle more complex computational domains. Cases with a solitary wave propagating along a 180° bend channel and wave interactions with a bottom mounted and surface-piercing vertical cylinder or with a fixed and partially submerged cylinder are simulated. The model tests and validation in terms of the effects of grid size, time step and irregular domain are presented and discussed.

3.1 Finite Difference Formulations

The finite difference method is applied to solve the governing equation and boundary conditions. Following the usual notations, $\phi_{i,j,k}^{n}$ and $\zeta_{i,j}^{n}$ are defined as $\phi_{i,j,k}^{n} = \phi\left(i\Delta\xi, j\Delta\eta, k\Delta\gamma, n\Delta t\right)$ and $\zeta_{i,j}^{n} = \zeta\left(i\Delta\xi, j\Delta\eta, n\Delta t\right)$, in which *i, j,* and *k* are grid indices along respectively ξ, η, and γ directions, *n* is the time level index, Δt is the time step, and $\Delta\xi = \Delta\eta = \Delta\gamma = 1$ are spatial mesh sizes in ξ, η, and γ directions. The central difference scheme when applied to discretize the spatial derivatives in the governing equation [Eq.(2- 44)] yields

$$c111\phi_{i,j,k}^{n+1} = c112\phi_{i,j,k+1}^{n+1} + c110\phi_{i,j,k-1}^{n+1} + c211\phi_{i+1,j,k}^{n+1} + c011\phi_{i-1,j,k}^{n+1} +$$

$$c212\phi_{i+1,j,k+1}^{n+1} + c012\phi_{i-1,j,k+1}^{n+1} + c210\phi_{i+1,j,k-1}^{n+1} + c010\phi_{i-1,j,k-1}^{n+1} +$$

$$c221\phi_{i+1,j+1,k}^{n+1} + c021\phi_{i-1,j+1,k}^{n+1} + c201\phi_{i+1,j-1,k}^{n+1} + c001\phi_{i-1,j-1,k}^{n+1} +$$

$$c122\phi_{i,j+1,k+1}^{n+1} + c102\phi_{i,j-1,k+1}^{n+1} + c120\phi_{i,j+1,k-1}^{n+1} + c100\phi_{i,j-1,k-1}^{n+1} +$$

$$c121\phi_{i,j+1,k}^{n+1} + c101\phi_{i,j-1,k}^{n+1} , \tag{3- 1}$$

where

$$c111 = 2\left(\frac{g_{11}}{\Delta\xi^2} + \frac{g_{22}}{\Delta\eta^2} + \frac{g_{33}}{\Delta\gamma^2}\right) , \tag{3- 2}$$

$$c112 = \frac{g_{33}}{\Delta\gamma^2} + \frac{f_3}{2\Delta\gamma} , \tag{3- 3}$$

$$c110 = \frac{g_{33}}{\Delta\gamma^2} - \frac{f_3}{2\Delta\gamma} , \tag{3- 4}$$

$$c211 = \frac{g_{11}}{\Delta\xi^2} + \frac{f_1}{2\Delta\xi} , \tag{3- 5}$$

$$c011 = \frac{g_{11}}{\Delta\xi^2} - \frac{f_1}{2\Delta\xi} , \tag{3- 6}$$

$$c212 = c010 = \frac{g_{13}}{4\Delta\xi\Delta\gamma} , \tag{3- 7}$$

$$c012 = c210 = -\frac{g_{13}}{4\Delta\xi\Delta\gamma} , \tag{3- 8}$$

$$c221 = c001 = \frac{g_{12}}{4\Delta\xi\Delta\eta} \ , \tag{3- 9}$$

$$c021 = c201 = \frac{-g_{12}}{4\Delta\xi\Delta\eta} \ , \tag{3- 10}$$

$$c122 = c100 = \frac{g_{23}}{4\Delta\eta\Delta\gamma} \ , \tag{3- 11}$$

$$c102 = c120 = \frac{-g_{23}}{4\Delta\eta\Delta\gamma} \ , \tag{3- 12}$$

$$c121 = \frac{g_{22}}{\Delta\eta^2} + \frac{f_2}{2\Delta\eta} \ , \text{ and} \tag{3- 13}$$

$$c101 = \frac{g_{22}}{\Delta\eta^2} - \frac{f_2}{2\Delta\eta} \ . \tag{3- 14}$$

The value of $\phi_{i,j,k}$ at each grid point and at the new time level is evaluated by solving Eq. (3- 1) through the iteration procedure. A mixed explicit-implicit scheme is adopted to solve the nonlinear free surface boundary conditions specified at the grid points on the free surface. Free surface elevation ζ and velocity potential ϕ there at the new time level are determined through the developed numerical algorithm. The explicit finite difference expressions of the transformed kinematic and dynamic free-surface boundary conditions [Eqs. (2- 48) and (2- 49)] are derived as

$$\zeta_{i,j}^{\widetilde{n+1}} = \zeta_{i,j}^{n} + \Delta t E_{i,j,KM}^{n} \ , \tag{3- 15}$$

where

$$E^n_{i,j,KM} = w^n_{i,j,KM}$$
$$-\left\{u_{i,j,KM}\frac{\left(y_{i,j+1,KM}-y_{i,j-1,KM}\right)\left(\zeta_{i+1,j}-\zeta_{i-1,j}\right)-\left(y_{i+1,j,KM}-y_{i-1,j,KM}\right)\left(\zeta_{i,j+1}-\zeta_{i,j-1}\right)}{\left(x_{i+1,j,KM}-x_{i-1,j,KM}\right)\left(y_{i,j+1,KM}-y_{i,j-1,KM}\right)-\left(x_{i,j+1,KM}-x_{i,j-1,KM}\right)\left(y_{i+1,j,KM}-y_{i-1,j,KM}\right)}\right\}^n$$
$$-\left\{v_{i,j,KM}\frac{\left(x_{i+1,j,KM}-x_{i-1,j,KM}\right)\left(\zeta_{i,j+1}-\zeta_{i,j-1}\right)-\left(x_{i,j+1,KM}-x_{i,j-1,KM}\right)\left(\zeta_{i+1,j}-\zeta_{i-1,j}\right)}{\left(x_{i+1,j,KM}-x_{i-1,j,KM}\right)\left(y_{i,j+1,KM}-y_{i,j-1,KM}\right)-\left(x_{i,j+1,KM}-x_{i,j-1,KM}\right)\left(y_{i+1,j,KM}-y_{i-1,j,KM}\right)}\right\}^n$$

(3- 16)

and

$$\phi^{\widetilde{n+1}}_{i,j,KM} = \phi^n_{i,j,KM} + w^n_{i,j,KM}\left(\zeta^{n+1}_{i,j}-\zeta^n_{i,j}\right)-\Delta t F^n_{i,j,KM}\ , \tag{3- 17}$$

in which

$$F^n_{i,j,KM} = \left[\frac{1}{2}\left(u^2_{i,j,KM}+v^2_{i,j,KM}+w^2_{i,j,KM}\right)+\zeta_{i,j}\right]^n\ . \tag{3- 18}$$

The superscript $\widetilde{n+1}$ denotes the provisional values at $\widetilde{n+1}$time level through explicit computation. The index KM represents the vertical grid points at the water surface layer. Through the iteration procedure, the updated values of $\zeta^{\widetilde{n+1}}_{i,j}$ and $\phi^{\widetilde{n+1}}_{i,j,KM}$ after solving Eqs. (3-15) and (3-17) are used to average with the values calculated from the following implicit finite difference formulations

$$\zeta^{\overline{n+1}}_{i,j} = \zeta^n_{i,j} + \Delta t E^{n+1}_{i,j,KM} \text{ and} \tag{3- 19}$$

$$\phi^{\overline{n+1}}_{i,j,KM} = \phi^n_{i,j,KM} + w^{n+1}_{i,j,KM}\left(\zeta^{n+1}_{i,j}-\zeta^n_{i,j}\right)-\Delta t\left(F^{n+1}_{i,j,KM}\right), \tag{3- 20}$$

in which

$$E_{i,j,KM}^{n+1} = w_{i,j,KM}^{n+1} - \left\{ u_{i,j,KM} \frac{\left(y_{i,j+1,KM} - y_{i,j-1,KM}\right)\left(\zeta_{i+1,j} - \zeta_{i-1,j}\right) - \left(y_{i+1,j,KM} - y_{i-1,j,KM}\right)\left(\zeta_{i,j+1} - \zeta_{i,j-1}\right)}{\left(x_{i+1,j,KM} - x_{i-1,j,KM}\right)\left(y_{i,j+1,KM} - y_{i,j-1,KM}\right) - \left(x_{i,j+1,KM} - x_{i,j-1,KM}\right)\left(y_{i+1,j,KM} - y_{i-1,j,KM}\right)} \right\}^{n+1} - \left\{ v_{i,j,KM} \frac{\left(x_{i+1,j,KM} - x_{i-1,j,KM}\right)\left(\zeta_{i,j+1} - \zeta_{i,j-1}\right) - \left(x_{i,j+1,KM} - x_{i,j-1,KM}\right)\left(\zeta_{i+1,j} - \zeta_{i-1,j}\right)}{\left(x_{i+1,j,KM} - x_{i-1,j,KM}\right)\left(y_{i,j+1,KM} - y_{i,j-1,KM}\right) - \left(x_{i,j+1,KM} - x_{i,j-1,KM}\right)\left(y_{i+1,j,KM} - y_{i-1,j,KM}\right)} \right\}^{n+1}$$

(3- 21)

and

$$F_{i,j,KM}^{n+1} = \left[\frac{1}{2}\left(u_{i,j,KM}^2 + v_{i,j,KM}^2 + w_{i,j,KM}^2\right) + \zeta_{i,j}\right]^{n+1} . \quad (3\text{- }22)$$

The averaging procedures using values obtained from the explicit and implicit computations for $\zeta_{i,j}^{\widetilde{n+1}}$ and $\zeta_{i,j}^{\overline{n+1}}$ in kinematic free-surface boundary condition and for $\phi_{i,j,KM}^{\widetilde{n+1}}$ and $\phi_{i,j,KM}^{\overline{n+1}}$ in dynamic free-surface boundary condition are applied to further the determination of the final values of the free surface elevation $\zeta_{i,j}^{n+1}$ and velocity potential $\phi_{i,j,KM}^{n+1}$ at $(n+1)\Delta t$ time. The described formulations are shown below

$$\zeta_{i,j}^{n+1} = \left(\zeta_{i,j}^{\widetilde{n+1}} + \zeta_{i,j}^{\overline{n+1}}\right)/2 \text{ and} \quad (3\text{- }23)$$

$$\phi_{i,j,KM}^{n+1} = \left(\phi_{i,j,KM}^{\widetilde{n+1}} + \phi_{i,j,KM}^{\overline{n+1}}\right)/2 . \quad (3\text{- }24)$$

Once the values of $\zeta_{i,j}^{n+1}$ and $\phi_{i,j,KM}^{n+1}$ at the free surface are obtained from Eqs. (3- 23) and (3- 24), the velocity potential at each grid point below the free surface of the entire

computational domain at $(n+1)\Delta t$ time level can be determined by solving Eq. (3- 1) with additional inputs from open boundary conditions [Eqs. (2- 12a) to (2- 13a)].

3.2 Computational Domain with Multi-grid Systems

For modeling a solitary wave interaction with a fixed structure (e.g., a vertical circular cylinder), a single set of curvilinear grids can generally represent well the flow domain. However, the concern is that potentially the numerical instability and singularity may appear when applying the structural boundary conditions on the grid points located around the cylinder surface and the cuts of the grid system, especially at points in front of the structures that receive the direct impact from the incident nonlinear waves. In order to avoid the numerical errors caused by inappropriate grid points within a single set of curvilinear grid system, a multi-grid system and a multi-block computational method as introduced by Wang and Jiang (1994) for their numerical investigation of the interactions between a solitary wave and a transversely arranged two vertical cylinders is adopted for the present study. Polar grids (inner grids) are introduced to cover the region close to and on the cylinder surface while the rectangular grids (outer grids) are extended over the remaining fluid domain outside of the polar grid region. Overlapped grids between the inner and outer grid systems are arranged to allow the interpolation of physical variables at the grid interfaces for the numerical iteration and check of solution convergence. Figure 3- 1shows the distribution of the inner polar grids and the outer rectangular grids with the thick black line representing the inner boundary of the rectangular grids.

After an initial solitary wave introduced in the entire computational domain, to proceed to the next (or new) time level, the numerical procedure for the multi-grid systems is to firstly compute the velocity potentials and wave elevations throughout the

outer rectangular grids. Then, a three-point interpolation scheme using the solutions of neighboring rectangular grids is carried out to provide the values of ϕ and ζ at the grid points of the outer boundary of the inner polar grids. With the boundary values are determined, the computation moves to the inner polar grids. Once the values of physical variables within the inner polar grids are calculated, the velocity potentials and wave elevations of the inner boundary of the outer rectangular grids are updated by the three-point interpolation scheme using the values obtained from the computation within the inner polar grids. The procedures are repeated until the converged solutions are obtained at the new time level. The computation continues until the allotted final time level.

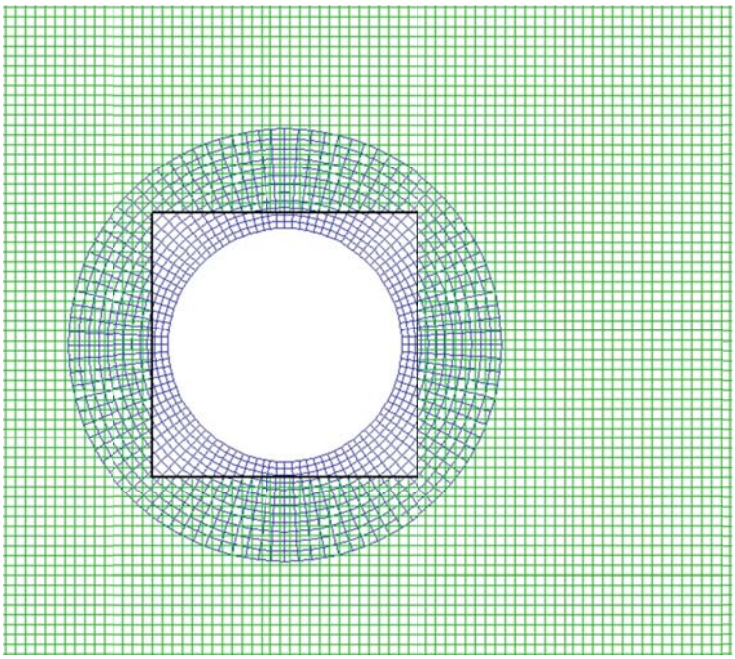

Figure 3- 1 Two-grid system with arranged grid points for a bottom mounted and surface piercing cylinder situated in a computational domain

For the vertical direction (z direction), the z coordinates are calculated using the algebraic grid generation method as

$$z(i,j,k) = z(i,j,1) + [z(i,j,\mathrm{KM}) - z(i,j,1)]\,(k-1)/(\mathrm{KM}-1)\ . \qquad (3\text{-}25)$$

Again, KM represents the maximum index of the grid points along the z direction and $z(i,j,\mathrm{KM})$ denotes the vertical coordinate of the free surface. An example plot of the grid system along the x-z plane is presented in Figure 3- 2.

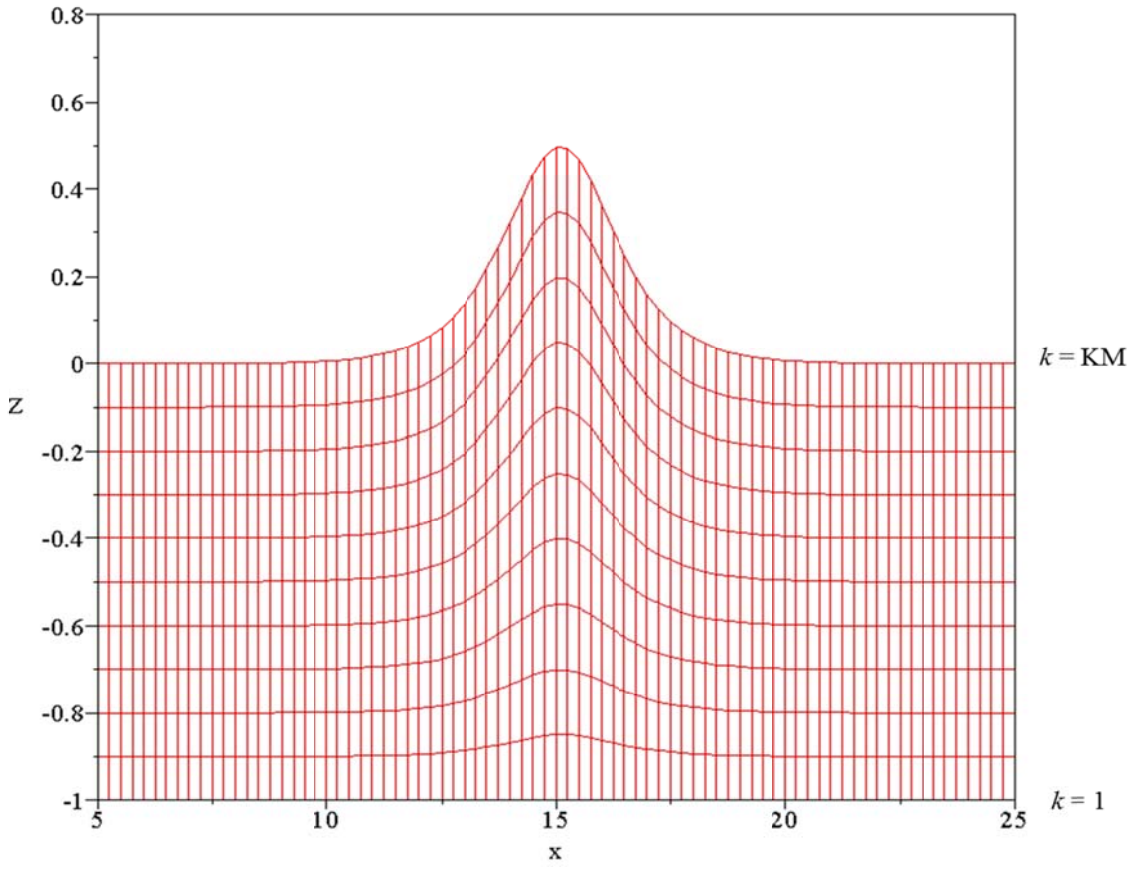

Figure 3- 2 An x-z plane view of the grid system in the physical domain

For a partially submerged floating cylinder case, the computational domain is separated into the outer region of the cylinder and the inner region beneath the cylinder. Computation for the flow domain beneath the cylinder needs to be considered. The grid setup for the outer region (excluding the region beneath the cylinder) is similar to the case with a bottom mounted and surface-piercing vertical cylinder. In the inner region (i.e. region beneath the cylinder), the horizontal polar grids are extended from the cylinder boundary to the inner region, however, ended at an inner boundary slightly away from the central region to prevent from the occurrence of numerical instability as a result of near zero grid sizes. Additional rectangular grids are placed to cover the central region beneath the cylinder. Again, within the central region, the overlapped inner rectangular and polar grids are arranged to allow the values of the physical variables be interpolated between the two-grid systems. The arrangement of the grid systems in the region outside of the cylinder is the same as the bottom-mounted vertical cylinder case as described above in Figure 3- 1. Overall, the grid arrangement, which consists of two rectangular grid systems and one polar grid system, for the flow domain including a region beneath a partially submerged cylinder is shown in Figure 3- 3. As can be seen in Figure 3- 3, the red dash circle represents the boundary of the cylinder. From Figure 3- 3, it is noted that the polar grids are extended to the outer part of the inner region beneath the cylinder. Added rectangular grids are set at the central region to cover the flow domain in that region. Compared to the thin polar lines, the thick ones represent the polar grid system for region outside of the cylinder. The interfaces connecting two overlapped neighboring grid systems are marked in black lines in Figure 3- 3.

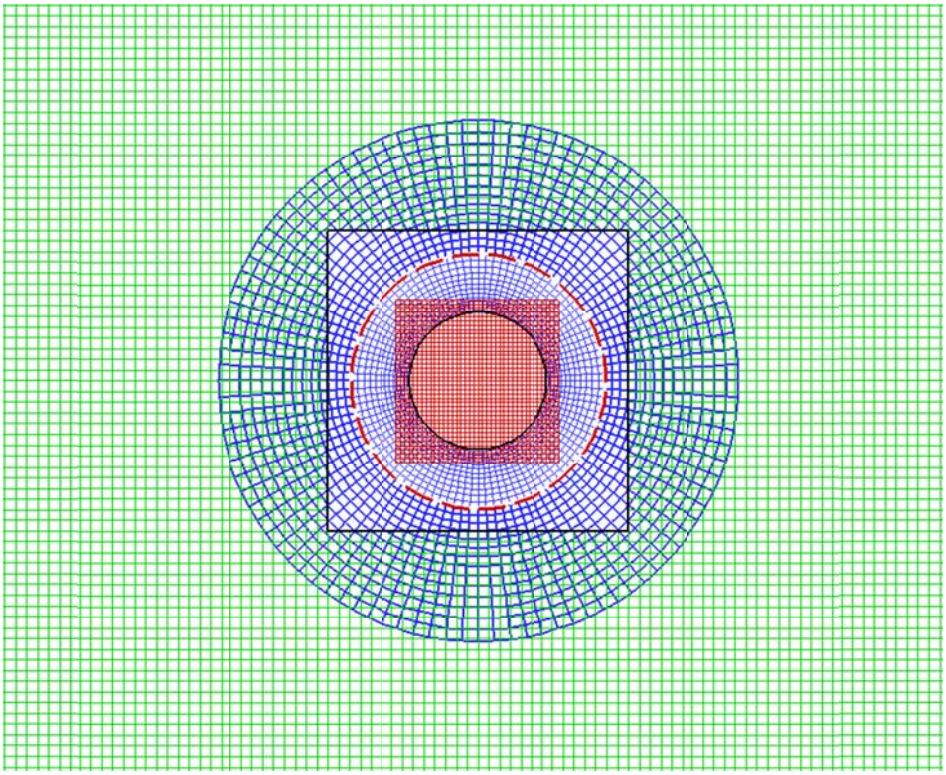

Figure 3- 3 Grid arrangement with two rectangular grid systems and one polar grid system for the flow domain including a region beneath a partially submerged cylinder

For the z direction, the algebraic grid generation method [Eq. (3- 25)] is again applied and modified to calculate the vertical coordinates for the regions beneath and nearby of the cylinder

$$\left.\begin{aligned} z(i,j,k) &= z(i,j,1)+\left[z(i,j,k_{bot})-z(i,j,1)\right](k-1)/(k_{bot}-1), k=2\sim k_{bot}-1 \\ z(i,j,k) &= z(i,j,k_{bot})+\left[z(i,j,KM)-z(i,j,k_{bot})\right](k-k_{bot})/(KM-k_{bot}), k=k_{bot}\sim KM \end{aligned}\right\}, \quad (3\text{- }26)$$

where k_{bot} is the index number of the vertical layer representing the level of the bottom of the cylinder. The values of the velocity potential and free surface elevation of the interfaces, namely the inner boundary of the outer rectangular grids (for flow domain outside of the cylinder) and the inner boundary of the polar grids (for the domain beneath the cylinder), are updated through a three-point interpolation scheme between two different grid systems to further the iteration procedure. The computational procedure is repeated to the next time level once the converged solutions at the interfaces and the entire three-dimensional flow domain are obtained at the current time level.

3.3 Validation of the Numerical Model

Before using the developed three-dimensional fully nonlinear wave model to investigate numerically the interactions between an incident solitary wave and cylindrical structures, a series of test cases were simulated to examine the effects of the grid sizes and time step on the solutions and to validate the model stability and accuracy. Throughout the tests, reasonable input parameters can be selected. For testing of the newly developed fully nonlinear wave model, the cases considering a plane solitary wave propagating in a rectangular wave channel with a constant water depth were used.

As defined above, the x and y axes denote respectively the wave propagating direction and the transverse direction. The z axis points upward with z=0, namely the x-y plane, represents the undisturbed free surface. The computational domain in dimensionless units along x and y axes are respectively $0 \leq x \leq 80$ and $0 \leq y \leq 3$. The dimensionless water depth is set as one and the amplitude of the incident solitary wave α is equal to 0.4. The rectangular grid sizes in x-y plane and time increment are $\Delta x = 0.25$,

$\Delta y = 0.25$, and $\Delta t = 0.1$ for the numerical computations. The grid sizes varying from 0.05 to 0.07 in z direction are determined using Eq. (3-25) with KM = 21. The converged criteria for the computations are set 10^{-6}. A three-dimensional perspective view plot of the simulated free-surface elevation (with inputs of $\alpha = 0.4$ and $x_0 = 10$) at $t = 50$ is presented in Figure 3- 4. Stable solutions showing the incident solitary wave reaching at a downstream location can be noticed from Figure 3- 4.

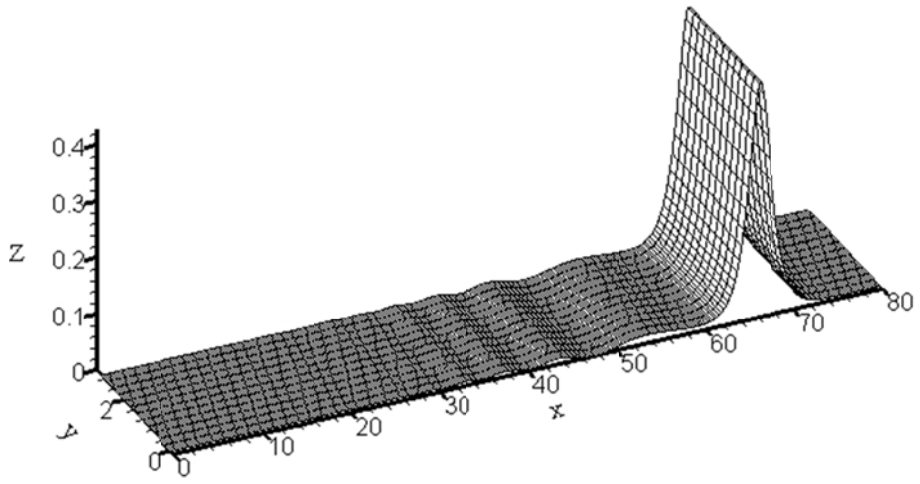

Figure 3- 4 Three-dimensional perspective view plot of the free-surface elevation for an $\alpha = 0.4$ incident solitary wave at $t = 50$.

Using the results obtained from the present model, a sequence of time series plots of the free-surface elevations along the central plane of the numerical channel are presented in Figure 3- 5. With the inputs of an incident solitary wave from Eqs. (2- 14) to (2- 19), the results in Figure 3- 5 indicate that the present model can produce stable wave

profles during the long process of wave propagation from upstream to downstream. Solitary wave solutions satisfying the three-dimensional fully nonlinear wave model can be obtained. It can be seen clearly that at different time levels the free-surface elevation of the solitary wave maintains the same shape and wave amplitude even when t =50. The difference between the computed peak of free-surface elevation and the targeted 0.4 amplitude is within one percent. The stable wave amplitude produced by the present model is an evidence of the stability and validity of the developed model.

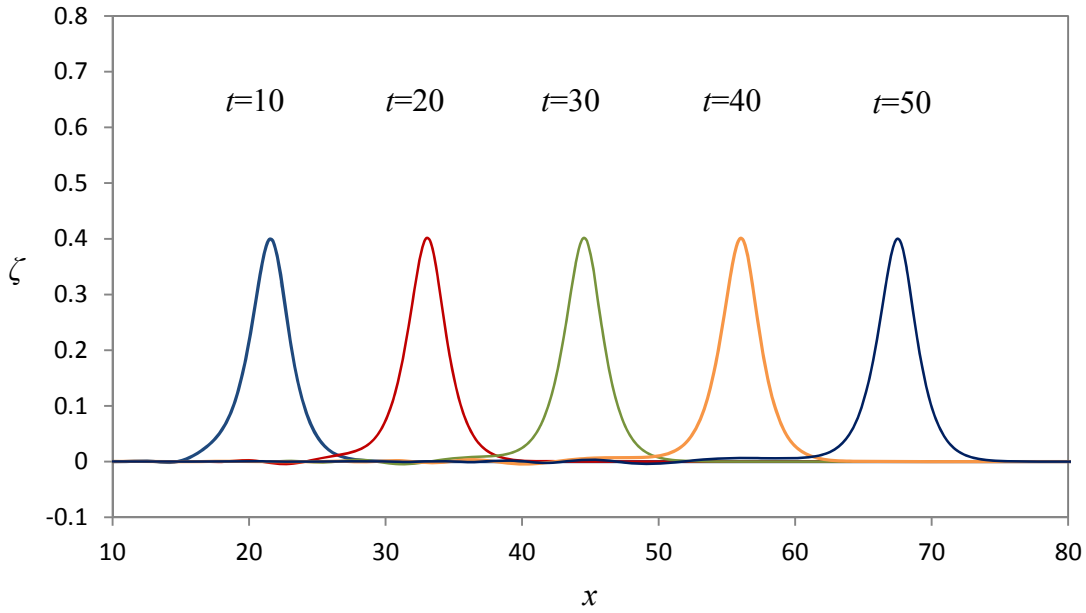

Figure 3- 5 A sequence of time series plots of numerically simulated solitary waves propagating in a channel of constant depth ($\alpha = 0.4$)

3.3.1 Selection of time step and grid size

The grid size and time step set for modeling studies affect the convergence and stability of the numerical simulation. In order to ascertain the convergence of the numerical scheme of the developed model, cases for a solitary wave propagating in a rectangular channel with various combinations of Δx, Δy, and Δt are selected to test the sensitives of the grid size and time step on the model results. As mentioned above, the x-axis represents the direction of wave propagation and the y-axis denotes the transverse direction. The z-axis points upward with $z = 0$ plane being located at the undisturbed free surface. The dimensionless dimensions of the wave channel are $0 \le x \le 80$ and $0 \le y \le 3$. The incident solitary-wave amplitude α is set as 0.4. The results of the free-surface elevation at $t = 30$ after the waves traveling from the initial position $x = 10$ ($t = 0$) are selected for comparison plots, where the effects of the time step and the grid size on the modeling performance can be examined.

First, the effects of time step on the wave simulation for fixed grid sizes are tested. The horizontal grid sizes Δx and Δy are set to be equal to 0.25 and twenty layers are arranged in the z-direction. The time steps Δt varying from 0.05 to 0.3 are considered for model simulations. Figure 3- 6 shows the comparisons of the numerically generated free-surface elevations with the case of different time interval at $t = 30$. The results in Figure 3- 6 indicate that similar water surface profiles are obtained for cases with $\Delta t = 0.05$, 0.1, 0.2, or 0.3. The simulation using $\Delta t = 0.3$ produces the least accurate results with a nearly three percent error. Certainly the amplitude of the solitary wave best fits to the set wave amplitude of 0.4 while time step is set as 0.1. The input of $\Delta t = 0.1$ gives the most accurate numerical solutions and the error is less than one percent. With

the further reduction of the time step to 0.05, the results do not show significant improvement from those obtained using $\Delta t = 0.1$. Thus, the time step $\Delta t = 0.1$ was used for all cases included in the present modeling study.

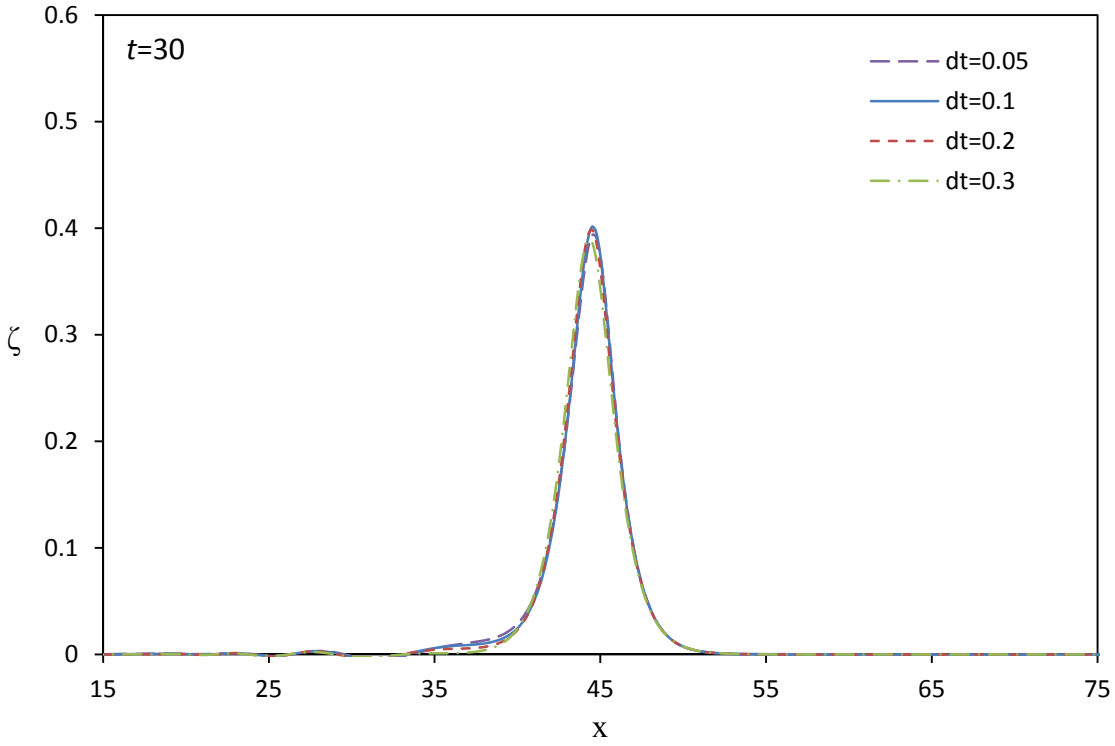

Figure 3- 6 Comparisons of numerical wave elevation profiles of different time interval for solitary waves propation with a constant depth ($\Delta x = \Delta y = 0.25$, $t = 30$)

The selection of grid size in the wave propagation direction, namely x-direction, is more critical for generating reliable results. The comparisons of simulated free-surface elevations under the various conditions of varying grid size Δx, which ranges from 0.2

to 0.3, are presented in Figure 3- 7. The results that when grid size 0.25 is used, the computed free surface elevations best fit to the targeted solitary wave profile including the wave amplitude of 0.4. Also, the overall error is less than 1 percent. The wave elevations from the case of grid size of 0.2 are in general similar to those from the case with $\Delta x = 0.25$, however, with a slightly overpredicted wave amplitude which has a nearly 2.5 percent error. The comparisons suggest $\Delta x = 0.25$ to be a reasonable grid size used in a Cartesian grid domain. Figure 3- 8 illustrates the comparisons of simulated wave profiles at $t = 30$ from cases using different grid sizes in transverse (or y) direction. The grid size includes 0.2, 0.25, and 0.3. Due to the fact of wave propagation along the x direction, the grid size in y direction does not show an apparent effect on the simulated results. The grid size Δy is set to be 0.25 for this study, which is comparable to the grid size chosen along the x direction. Additionally, the effect of the numbers of layers along the z direction on the results obtained from the present three-dimensional model also needs to be evaluated. Figure 3- 9 presents the comparison plots of the free-surface elevations using various grid systems with changes of the numbers of vertical layer. As can be seen in Figure 3- 9, the results indicate that the wave profiles at $t = 30$ under the condition of twenty layers match the peak and phase closely with those from the case with twenty-five layers. The results from using ten or fifteen layers deviate in phase slightly from those with twenty or twenty-five layers used. The percentage difference of the phase of the wave peak between the values using ten, fifteen, and twenty layers and that from the twenty-five layer case are 1.68%, 1.12%, and 0.56%. For the consideration of the accuracy of the modeling results and computational efficiency, twenty layers along the vertical direction are selected.

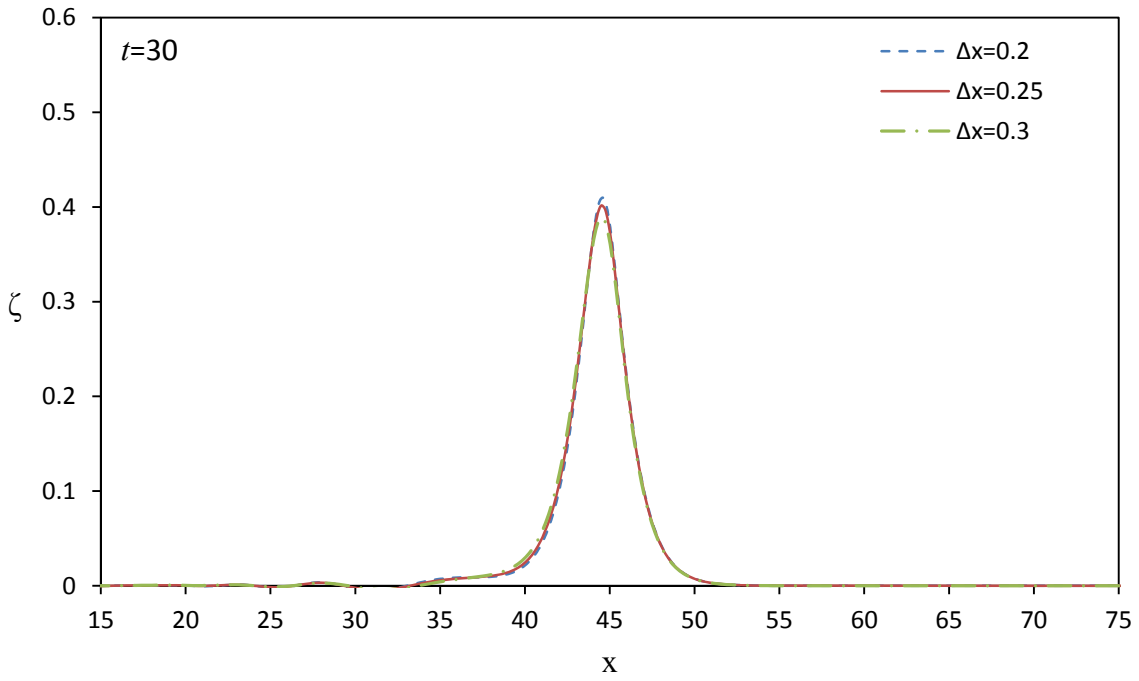

Figure 3- 7 Comparisons of numerical profiles of different grid sizes in x-direction for solitary waves propation with a constant depth ($\Delta t = 0.1$)

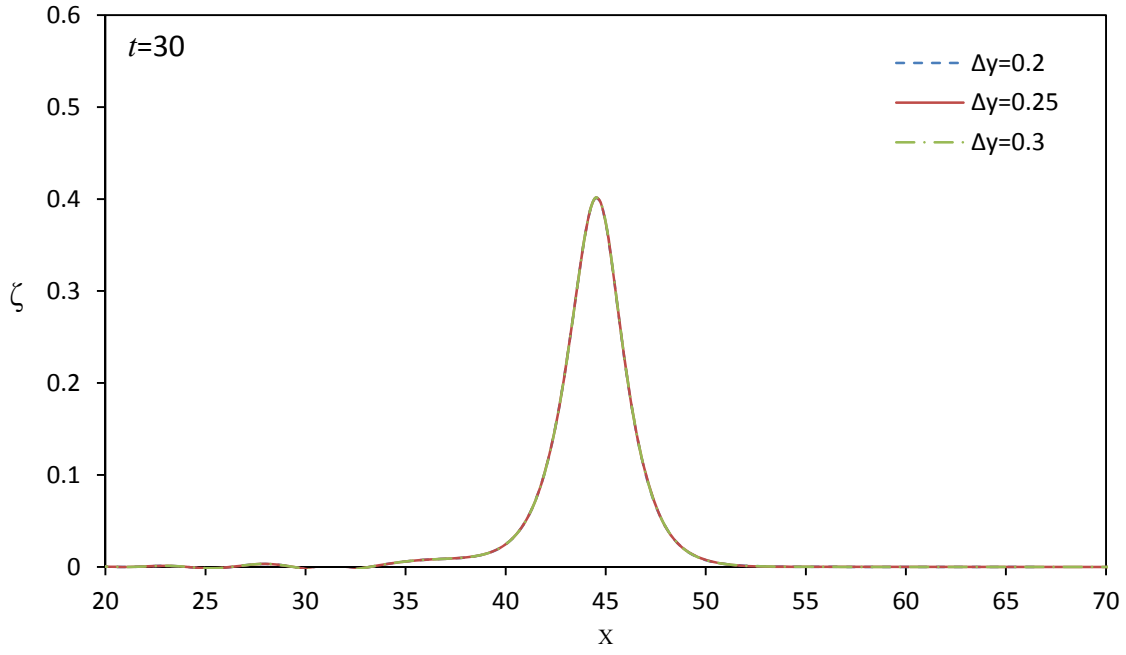

Figure 3- 8 Comparisons of numerical profiles of different grid sizes in y-direction for solitary waves propation with a constant depth ($\Delta t = 0.1$)

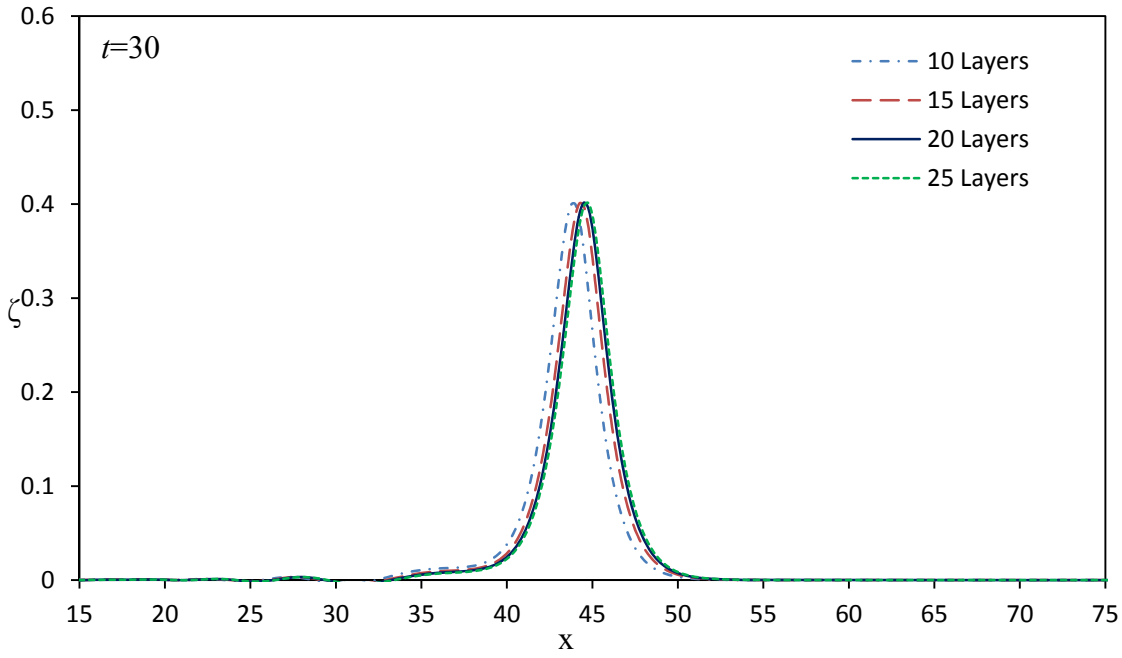

Figure 3- 9 Comparisons of numerical profiles of different grid sizes in x-direction for solitary waves propation with a constant depth ($\Delta x = \Delta y = 0.25, \Delta t = 0.1$)

3.3.2 Mass conservation

Examining the conservation of mass during the process of wave propagation is fundamental way to check the stability and accuracy of a model in numerical simulations. When the principle of mass conservation is satisfied, the excess mass of the wave domain should maintain as a constant value until the wave travels out of the computational domain with a constant fluid density, the excess mass (M) is calculated as an integration of the total fluid volume considering only the contribution of the free-surface elevation at a given instant. Thus, we have

$$M = \iint \zeta dxdy \ . \tag{3- 27}$$

Figure 3- 10 shows the time variation of the excess mass for the case of $\alpha = 0.4$. It is noted from Figure 3- 10 that the calculated total excess mass is kept as a constant value until the time reaches about 54.5 where the leading tail is about to propagate out of the computational domain. Further decrease of the excess mass reflects increase of the wave components propagate out of the downstream boundary. The results suggest the present model is capable of providing accurate and reliable predictions on wave propagation.

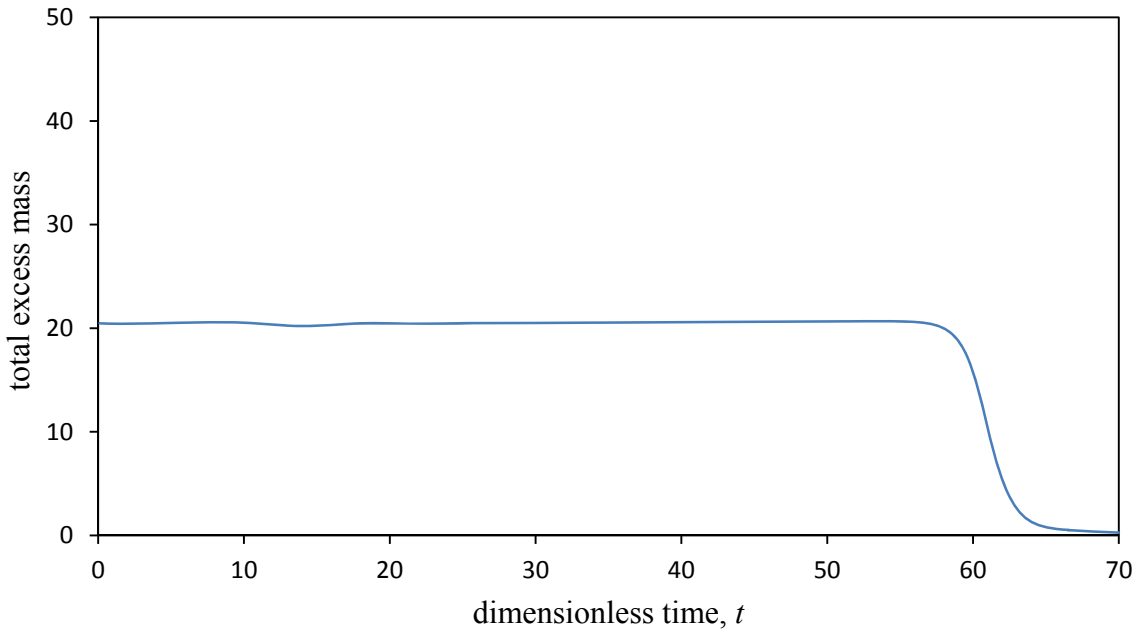

Figure 3- 10 Time variation of total excess mass within the computational domain

3.4 Solitary waves propagating in a curved channel

As described in Chapter 2, the curvilinear coordinate transformation technique can allow its grid system to fit to a domain with irregular boundaries. The present three-dimensional fully nonlinear wave model that developed based on the curvilinear coordinate transformation technique is capable of simulating propagation of waves not only in a standard straight channel but also can in a channel of arbitrary shapes. The application of the present model in simulating a solitary wave propagating through a 180° curved (U-shaped) channel with results showing the variations of free-surface elevations is presented in this chapter. The numerical results calculated by the present model are compared with these from the generalized Boussinesq model for cross checking of the model performance in simulating wave propagation and transformation.

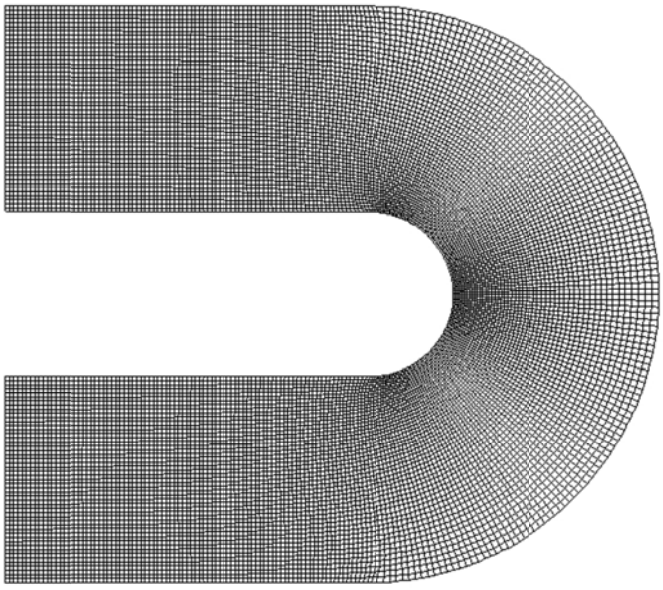

Figure 3- 11 A vertical view of the U-shape curved channel

Shown in Figure 3- 11 is a curvilinear grid system for the modeling domain of a 180° curved channel. The width of the channel is 12.5 whereas the length along the central plane is 95. The radii of the inner wall and the outer wall of the channel at the curved section are 5 and 17.5, respectively. An initial plane solitary wave with peak placed at $x_0 = 10$ is shown in Figure 3- 12. The wave amplitude α is set as 0.3

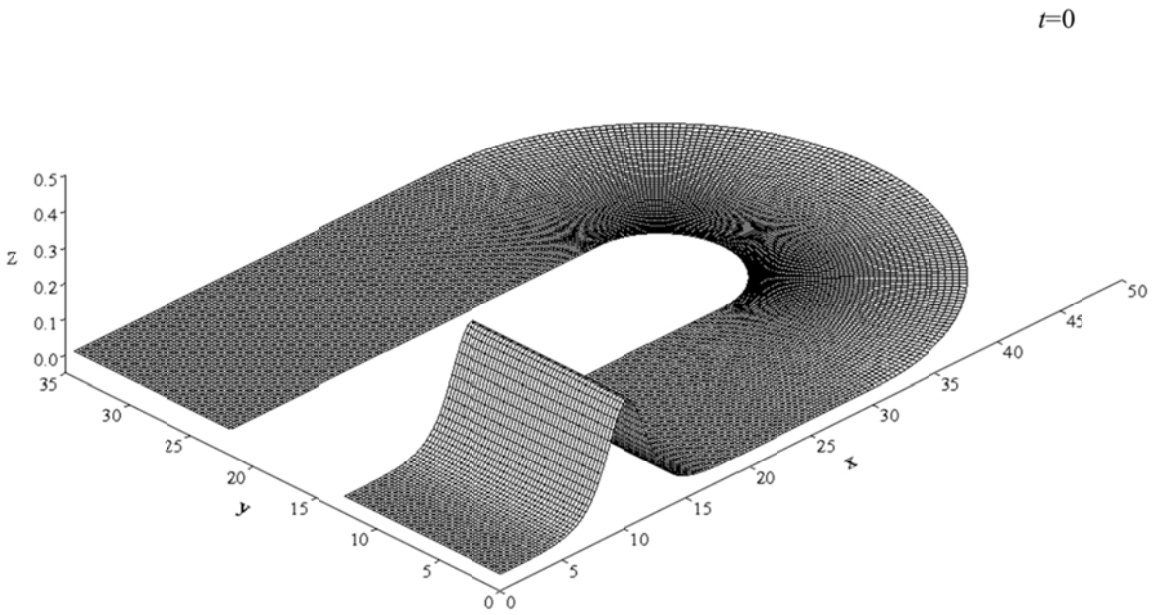

Figure 3- 12 Three-dimensional perspective view plot of an initial solitary wave with $\alpha = 0.3$

A series of three-dimensional perspective view plots and associated contours of the free-surface elevations at 10 selected instants for a solitary wave of $\alpha = 0.3$ propagating through a 180° curved channel are presented in Figure 3- 13. The solid and

dash lines in the contour plots represent respectively the positive and negative values of the wave elevations. From the plots shown in Figure 3- 13, it is noted that the solitary wave maintains as an uniform wave profile before it enters the curved portion of the channel at $t = 15$. As the solitary wave propagates into the curved channel at $t = 25$, the nonuniform distribution of the wave peak across the channel starts to form. Owing to the centrifugal effect, the wave elevation with increased amplitude near the outer wall shows the decreasing trend towards the inner wall of the channel. The wave encountering process on the outer wall is shown in results at $t = 30$ and $t = 35$, where the wave peak on the outer wall continues to increases. The water surface can reach up to about 0.48 at $t = 35$. Due to the length difference between the inner and the outer walls of the bended part of the channel as well as the wave diffraction effect, a curved wave front can be noticed. At $t = 40$ and $t = 45$, during the process of main wave propagates towards the downstream portion of the curved channel, as the effect of wave reflection, the high peak of the wave is observed to move to the center of the channel. Following the above described wave transition, the main wave close to the outer wall encounters the wall again and results in the increase of the free-surface elevation of the main wave near the outer wall at $t = 50$. Two high wave peaks coexist along the main wave crest. From $t = 50$ to $t = 70$, the position of the peak of wave elevation near the outer wave gradually catches up with the peak of the leading wave near the inner wall and the wave form tends to eventually recover as a solitary wave followed with a series of oscillating tails.

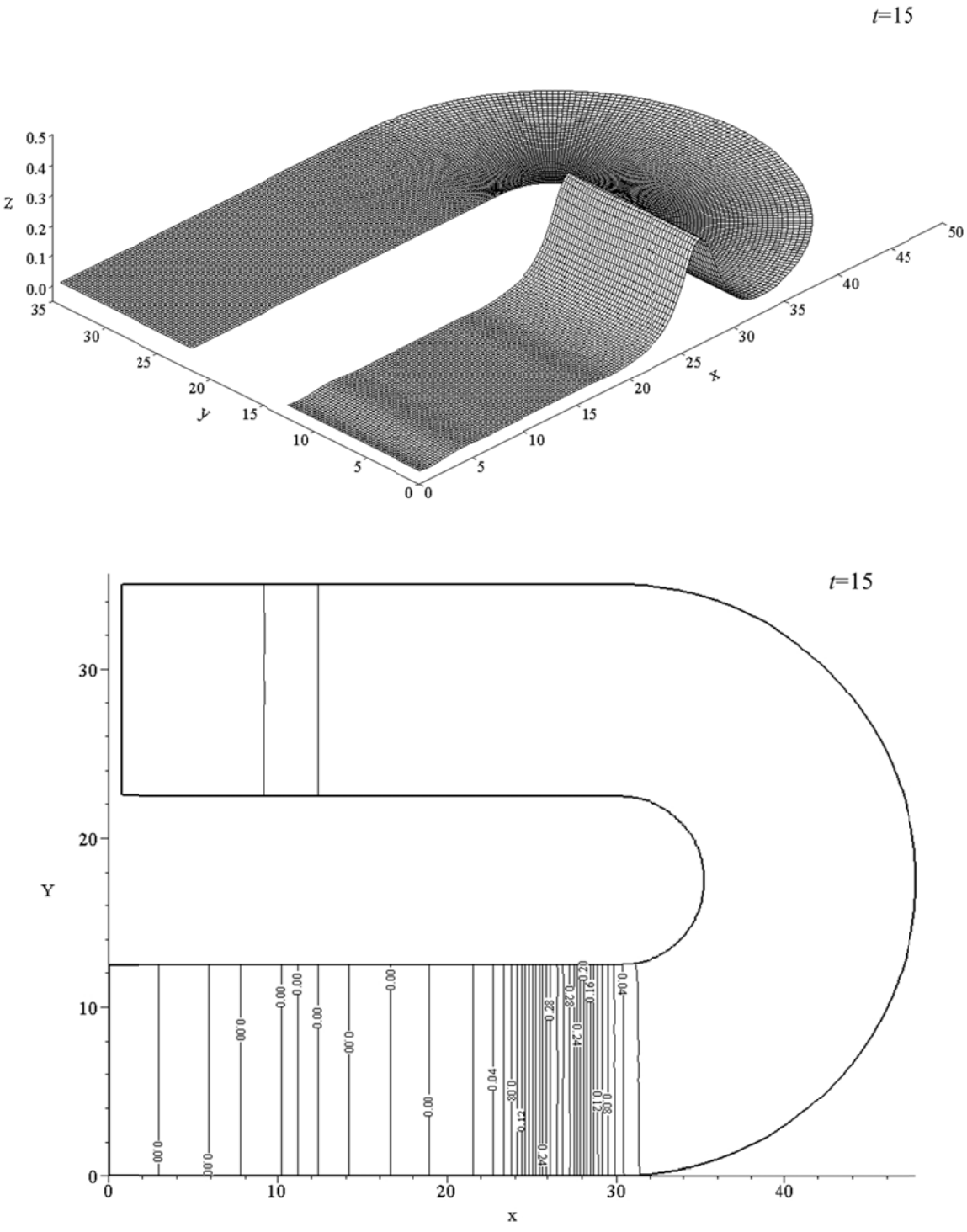

Figure 3- 13 Three-dimensional perspective view and contour plots of free-surface elevation ζ for $\alpha = 0.3$ at different time steps

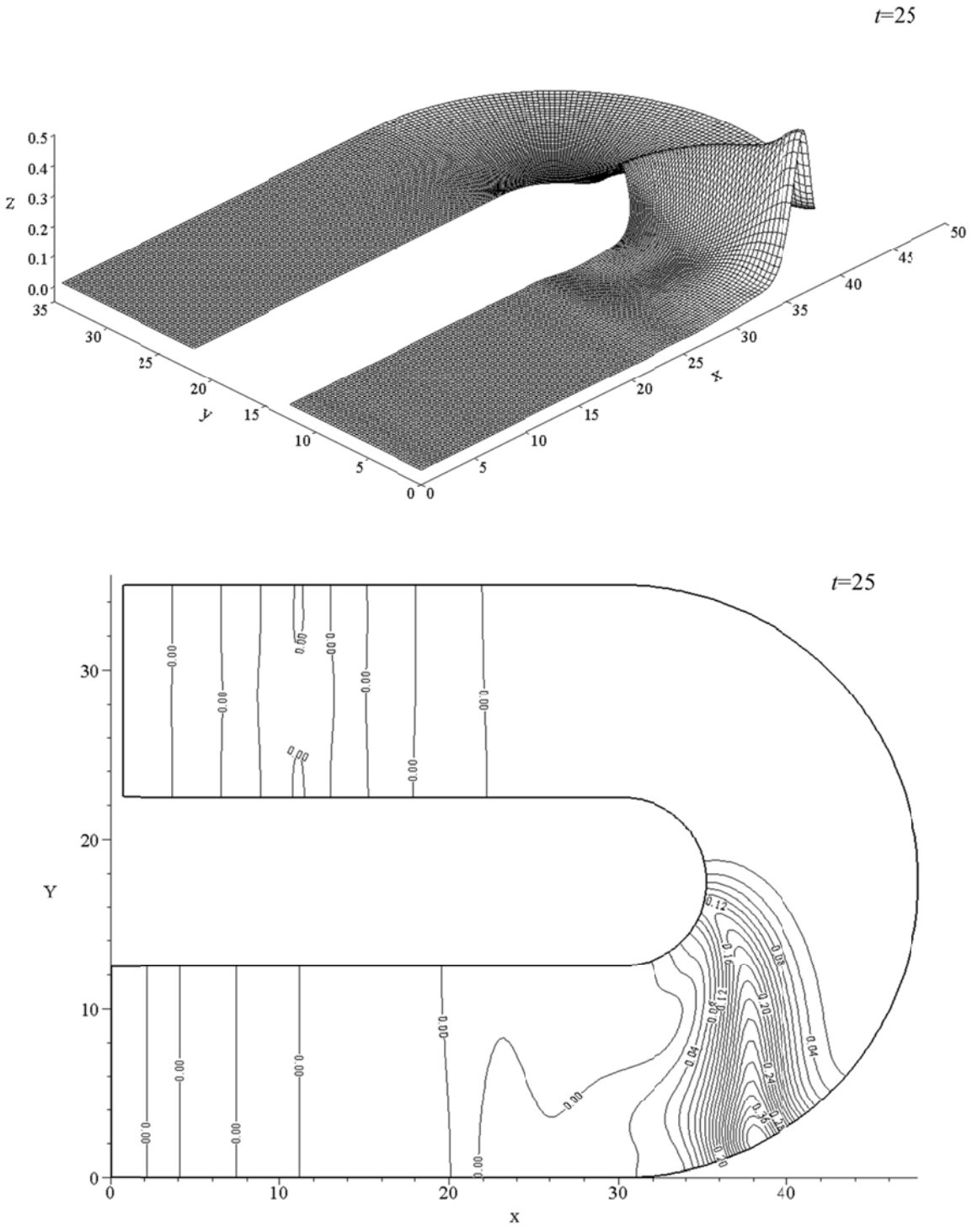

Figure 3- 13 Three-dimensional perspective view and contour plots of free-surface elevation ζ for $\alpha = 0.3$ at different time steps (Continued)

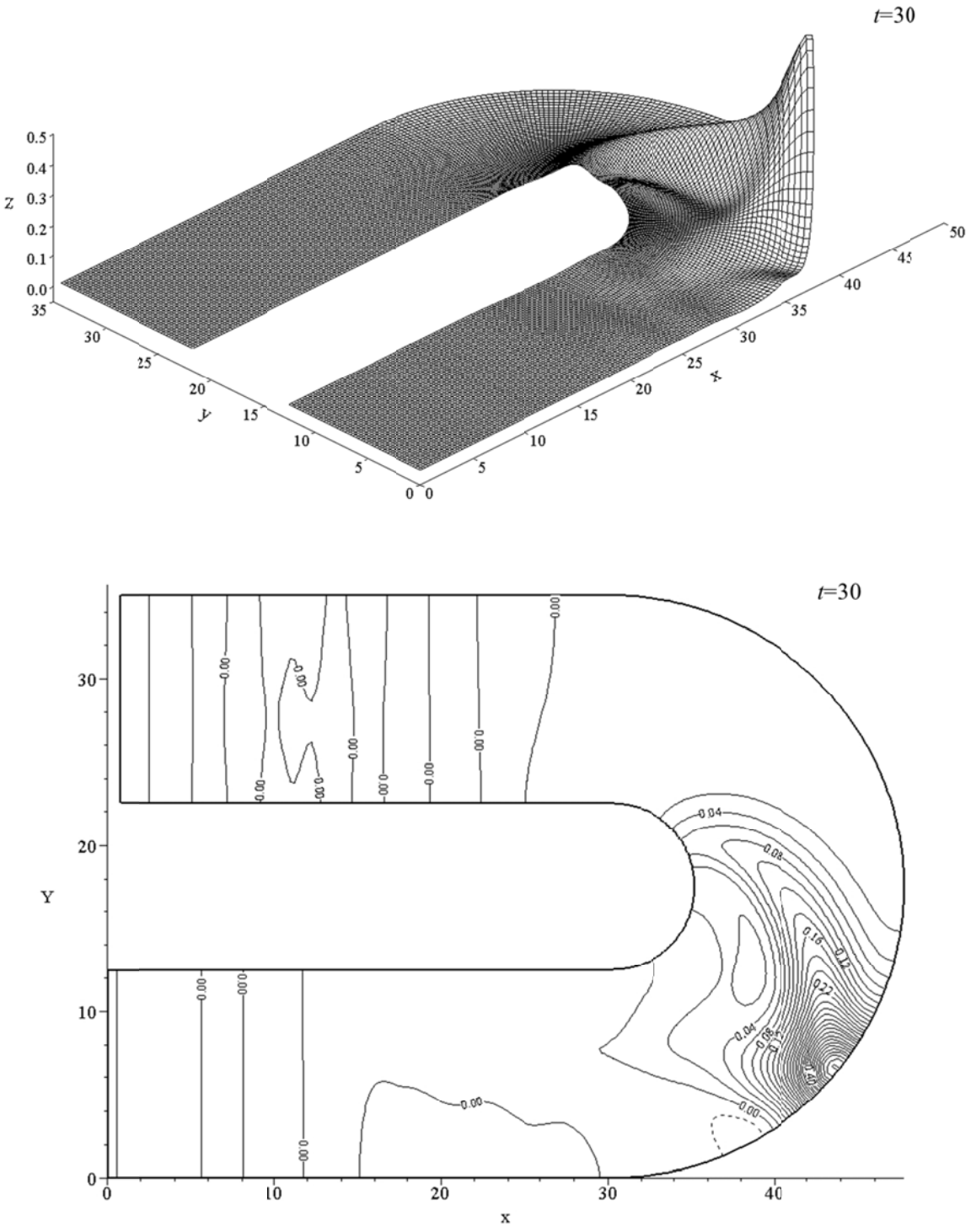

Figure 3- 13 Three-dimensional perspective view and contour plots of free-surface elevation ζ for $\alpha = 0.3$ at different time steps (Continued)

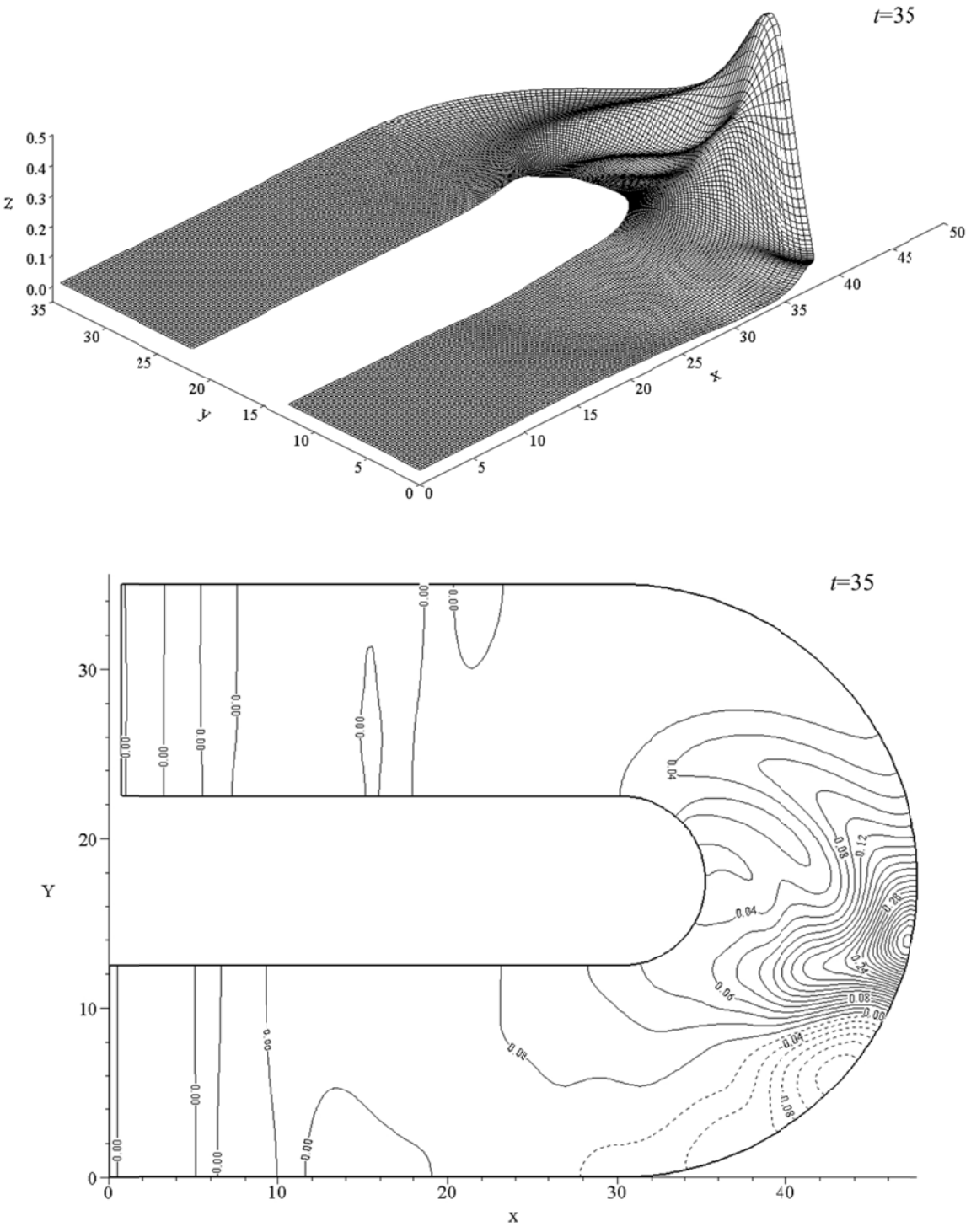

Figure 3- 13 Three-dimensional perspective view and contour plots of free-surface elevation ζ for $\alpha = 0.3$ at different time steps (Continued)

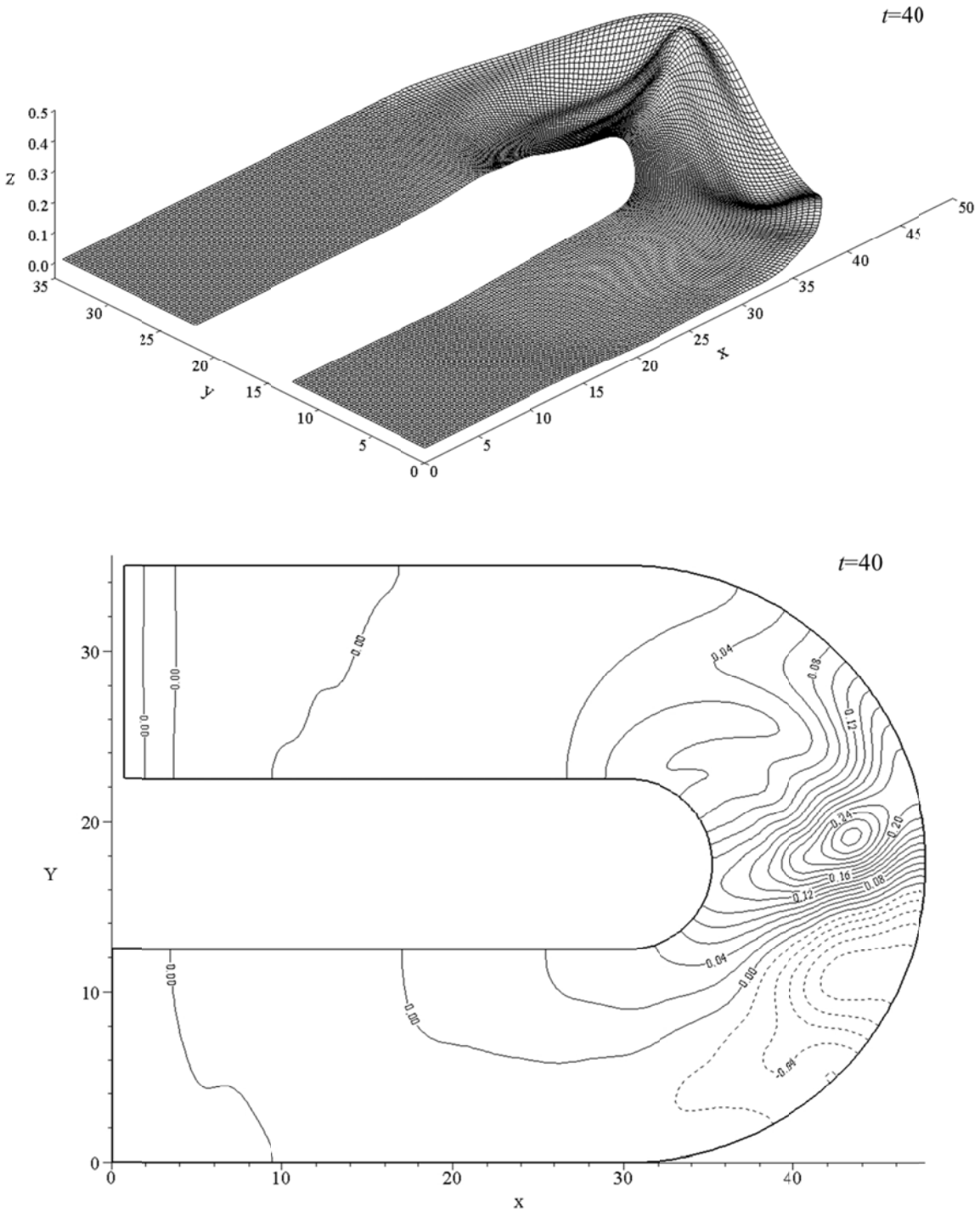

Figure 3- 13 Three-dimensional perspective view and contour plots of free-surface elevation ζ for $\alpha = 0.3$ at different time steps (Continued)

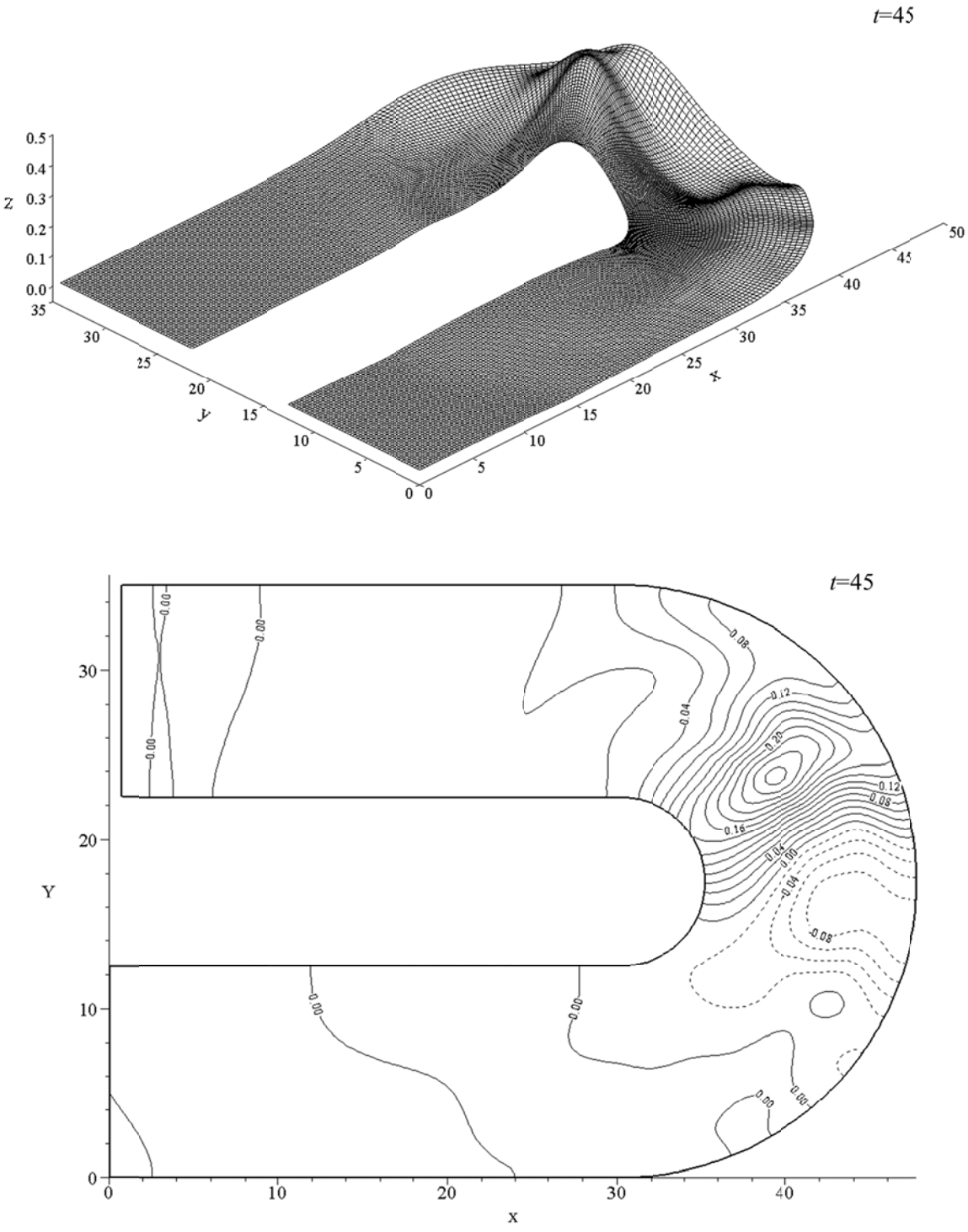

Figure 3- 13 Three-dimensional perspective view and contour plots of free-surface elevation ζ for $\alpha = 0.3$ at different time steps (Continued)

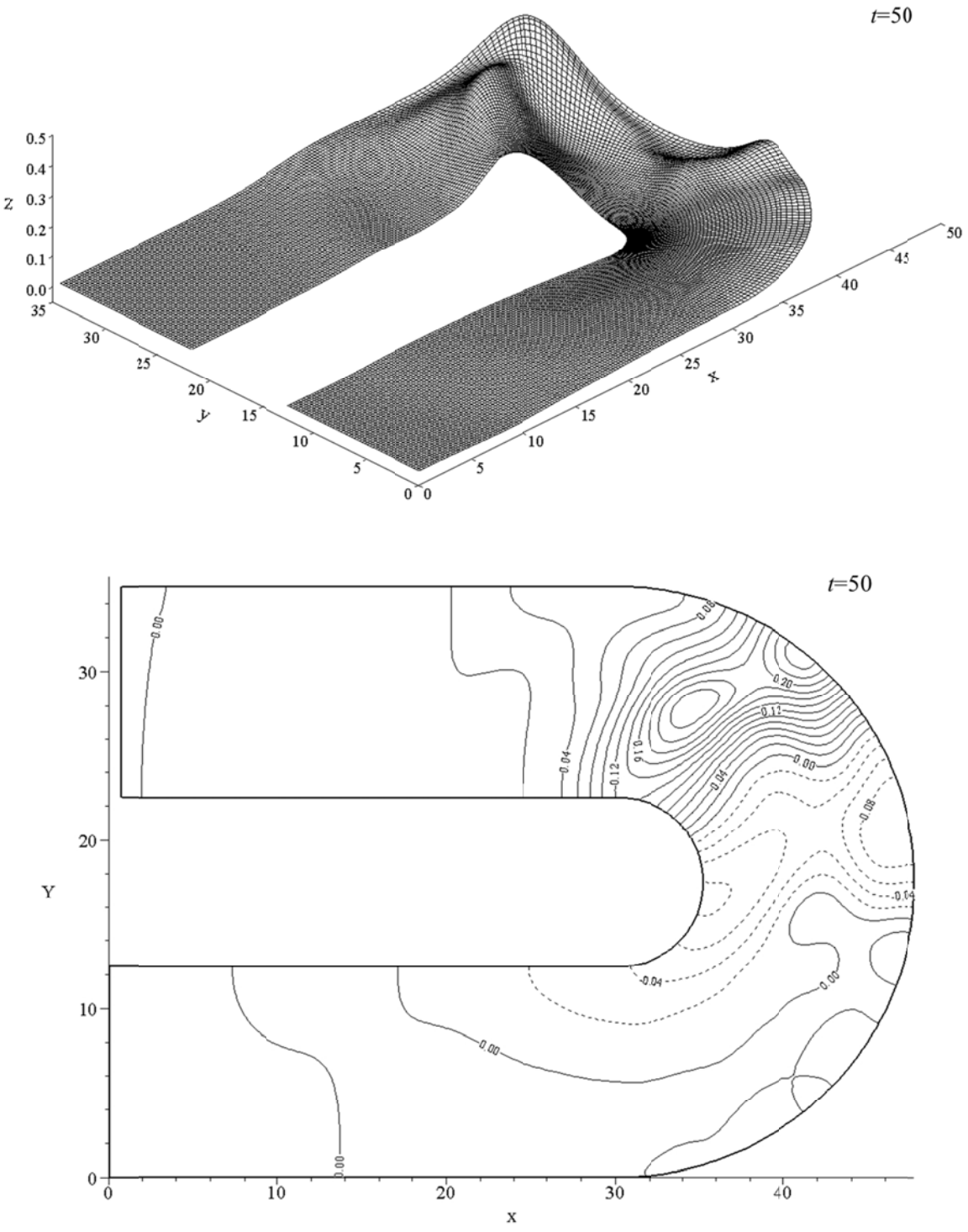

Figure 3- 13 Three-dimensional perspective view and contour plots of free-surface elevation ζ for $\alpha = 0.3$ at different time steps (Continued)

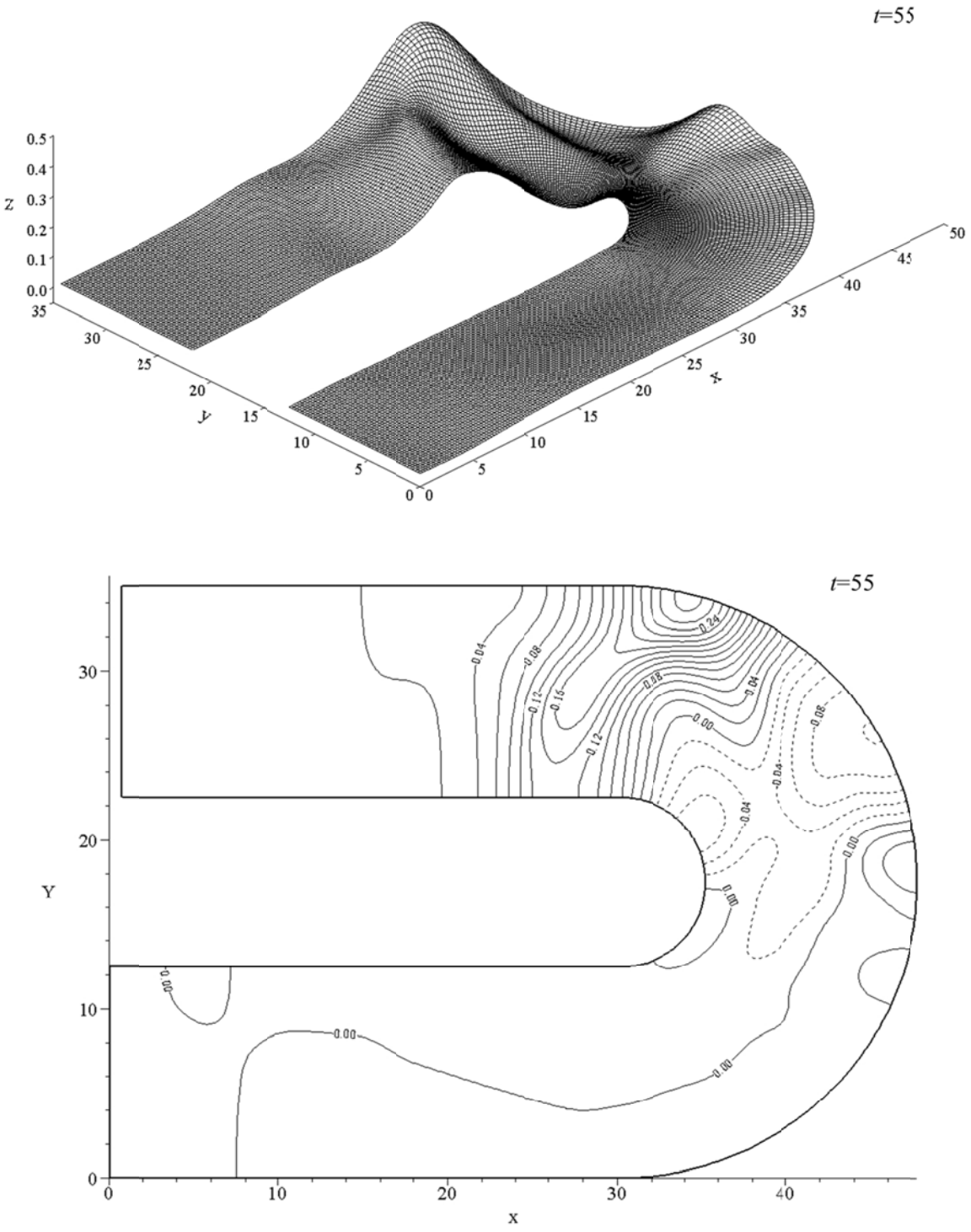

Figure 3- 13 Three-dimensional perspective view and contour plot of free-surface elevation ζ for $\alpha = 0.3$ at different time steps (Continued)

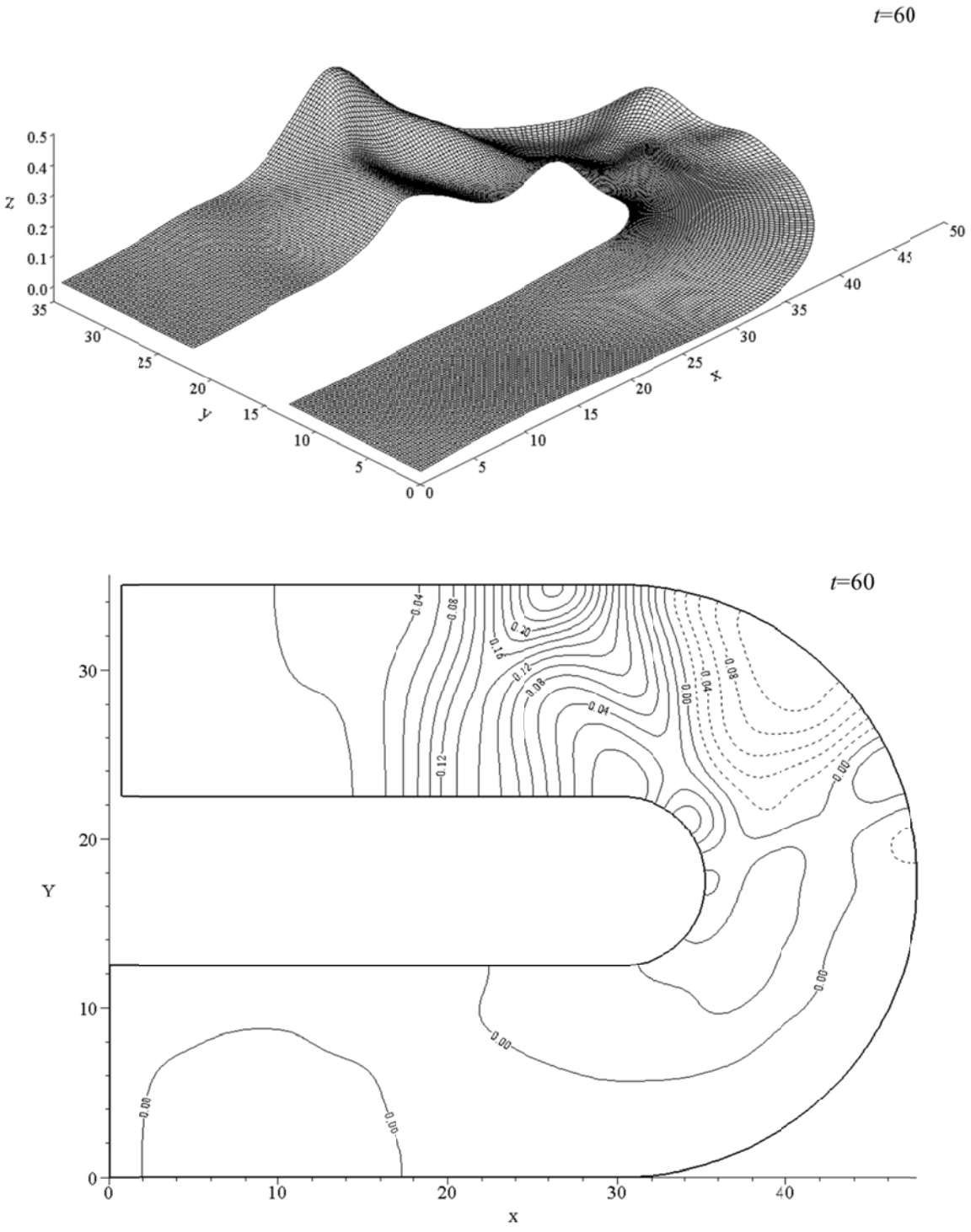

Figure 3- 13 Three-dimensional perspective view and contour plot of free-surface elevation ζ for $\alpha = 0.3$ at different time steps (Continued)

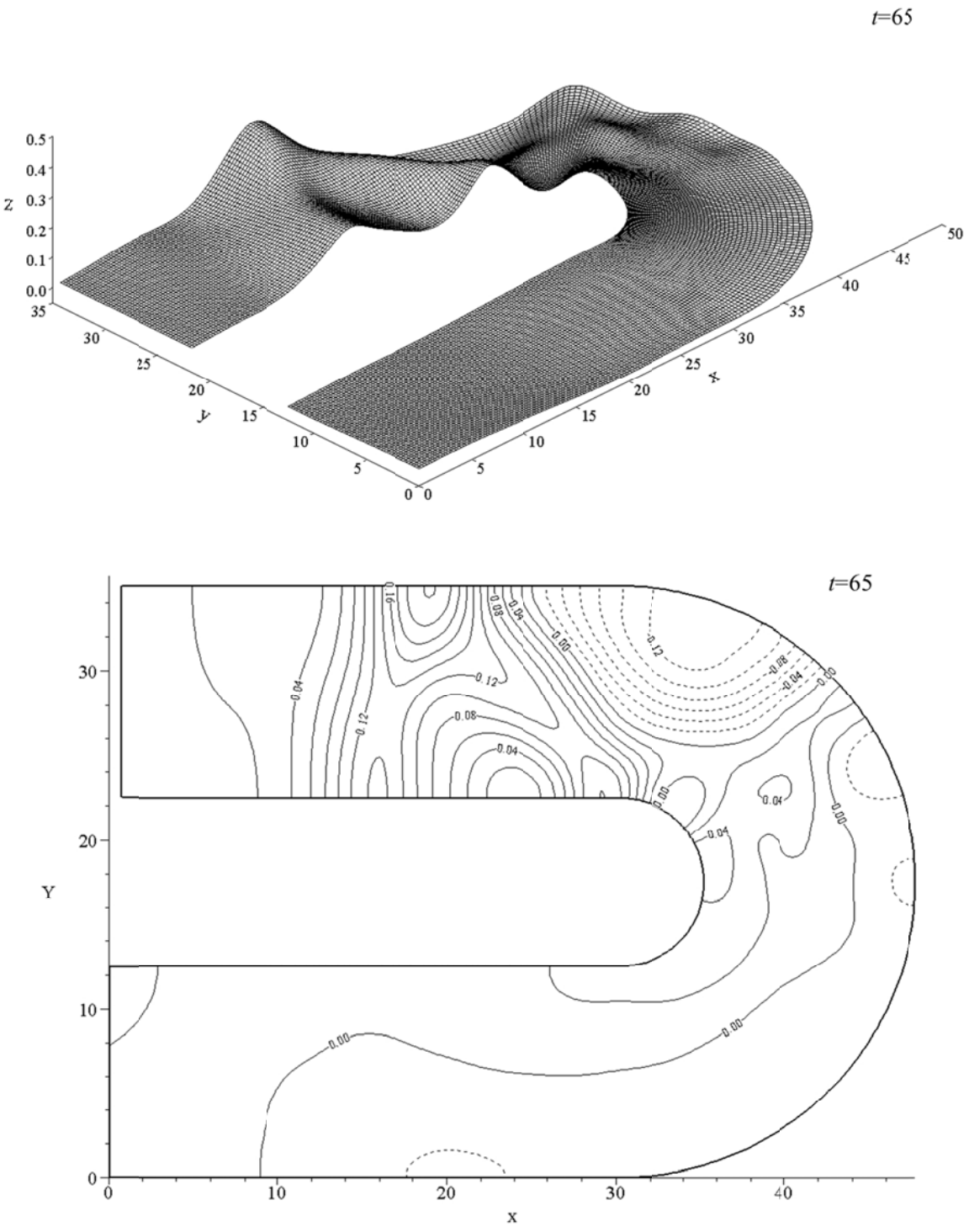

Figure 3- 13 Three-dimensional perspective view and contour plot of free-surface elevation ζ for $\alpha = 0.3$ at different time steps (Continued)

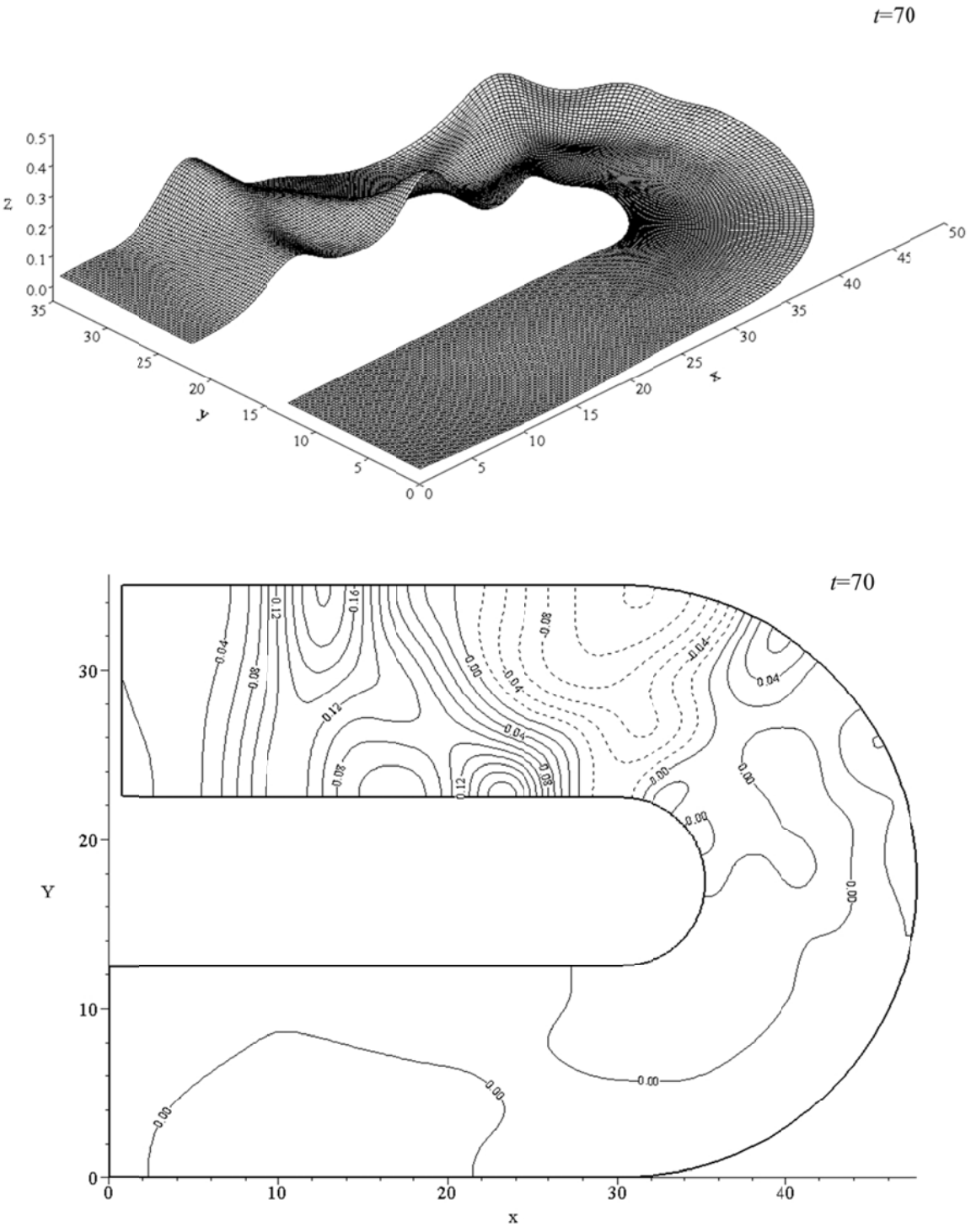

Figure 3- 13 Three-dimensional perspective view and contour plot of free-surface elevation ζ for $\alpha = 0.3$ at different time steps (Continued)

To provide the verification of the solution accuracy of the computed wave profiles along the curved channel as given above using the present three-dimensional fully nonlinear wave model, a well-established generalized Boussinesq (gB) two-equation model (Wang et al., 1992) is applied to calculate wave elevations of the similar case for comparisons. The dimensionless gB equations originally developed by Wu (1979) are capable of modeling propagation and transformation of weakly nonlinear and weakly dispersive waves in a domain of two horizontal dimensions. The gB equations are given below

$$\zeta_t + \nabla \cdot \left[(h+\zeta)\nabla\overline{\phi}\right] = -h_t + \nabla \cdot \left(\left\{ \frac{h}{2}\left[h_t + \nabla \cdot \left(h\nabla\overline{\phi}\right)\right] - \frac{h^2}{3}\nabla^2\overline{\phi} \right\} \nabla h \right) \text{ and} \qquad (3\text{- }28)$$

$$\overline{\phi}_t + \frac{1}{2}\left(\nabla\overline{\phi}\right)^2 + \zeta + p_o = \frac{h}{2}\frac{\partial}{\partial t}\left[h_t + \nabla \cdot \left(h\nabla\overline{\phi}\right)\right] - \frac{h^2}{6}\nabla^2\overline{\phi}_t, \qquad (3\text{- }29)$$

where p_o is the ambient surface pressure, h is the water depth and $\overline{\phi}$ is the layer-mean value of the original velocity potential defined as

$$\overline{\phi}(x,y,t) = \frac{1}{(h+\zeta)}\int_{-h}^{\zeta} \phi(x,y,z,t)\, dz\,. \qquad (3\text{- }30)$$

For the present case, we have $h = 1$ and $p_0 = 0$. Equations (3- 28) and (3- 29) can be simplified as

$$\zeta_t + \nabla \cdot \left[(1+\zeta)\nabla\overline{\phi} \right] = 0 \text{ and} \qquad (3\text{- }31)$$

$$\overline{\phi}_t + \frac{1}{2}\left(\nabla\overline{\phi}\right)^2 + \zeta = \frac{1}{3}\nabla^2\overline{\phi}_t \,. \tag{3- 32}$$

Following the approach introduced by Wang et al. (1992), Equations (3- 31) and (3- 32) are transformed into the curvilinear coordinates system as

$$\begin{aligned} &J_b{}^2\zeta_t + \delta\overline{\phi}_\xi\zeta_\xi - \beta\left(\overline{\phi}_\xi\zeta_\eta + \overline{\phi}_\eta\zeta_\xi\right) + \gamma\overline{\phi}_\eta\zeta_\eta \\ &+ \left(1+\zeta\right)\left(\delta\overline{\phi}_{\xi\xi} - 2\beta\overline{\phi}_{\xi\eta} + \gamma\overline{\phi}_{\eta\eta} + \sigma\overline{\phi}_\eta + \tau\overline{\phi}_\xi\right) = 0 \end{aligned} \tag{3- 33}$$

and

$$\begin{aligned} &J_b{}^2\overline{\phi}_t + \frac{1}{2}\left(\delta\overline{\phi}_\xi^2 - 2\beta\overline{\phi}_\eta\overline{\phi}_\xi + \gamma\overline{\phi}_\eta^2\right) + J_b{}^2\zeta \\ &= \frac{1}{3}\left(\delta\overline{\phi}_{\xi\xi t} - 2\beta\overline{\phi}_{\xi\eta t} + \gamma\overline{\phi}_{\eta\eta t} + \sigma\overline{\phi}_{\eta t} + \tau\overline{\phi}_{\xi t}\right) \end{aligned}, \tag{3- 34}$$

where

$$\delta(\xi,\eta) = x_\eta^2 + y_\eta^2, \tag{3- 35}$$

$$\beta(\xi,\eta) = x_\xi x_\eta + y_\xi y_\eta \,, \tag{3- 36}$$

$$\gamma(\xi,\eta) = x_\xi^2 + y_\xi^2, \tag{3- 37}$$

$$J_b(\xi,\eta) = x_\xi y_\eta - x_\eta y_\xi \,, \tag{3- 38}$$

$$\sigma(\xi,\eta)J = y_\xi\left(\delta x_{\xi\xi\xi} - 2\beta x_{\xi\eta} + \gamma x_{\eta\eta}\right) - x_\xi\left(\delta y_{\xi\xi\xi} - 2\beta y_{\xi\eta} + \gamma y_{\eta\eta}\right), \text{ and} \tag{3- 39}$$

$$\tau(\xi,\eta)J = x_{\xi}\left(\delta y_{\xi\xi\xi} - 2\beta y_{\xi\eta} + \gamma y_{\eta\eta}\right) - y_{\xi}\left(\delta x_{\xi\xi\xi} - 2\beta x_{\xi\eta} + \gamma x_{\eta\eta}\right). \qquad (3\text{-}40)$$

The curvilinear gB two-equation model [Equation (3- 33) and (3- 34)] with the use of a predictor-corrector finite difference scheme developed by Wang et al. (1992) is simulated to calculate the evolution of free-surface elevations for a solitary wave propagating in the 180° curved channel as described above. Computed wave elevations at three positions along each of five selected cross sections (A to E) throughout the channel are compared. The locations of five cross sections are shown in Figure 3- 14. Along each cross sections, three chosen positions as each marked by a black dot are denoted by "inner wall", "center of channel", and "outer wall", respectively. The comparisons of time varying free surface elevations obtained from the present model and from the gB two-equation model at each identified location are presented in Figure 3- 15 to Figure 3- 19.

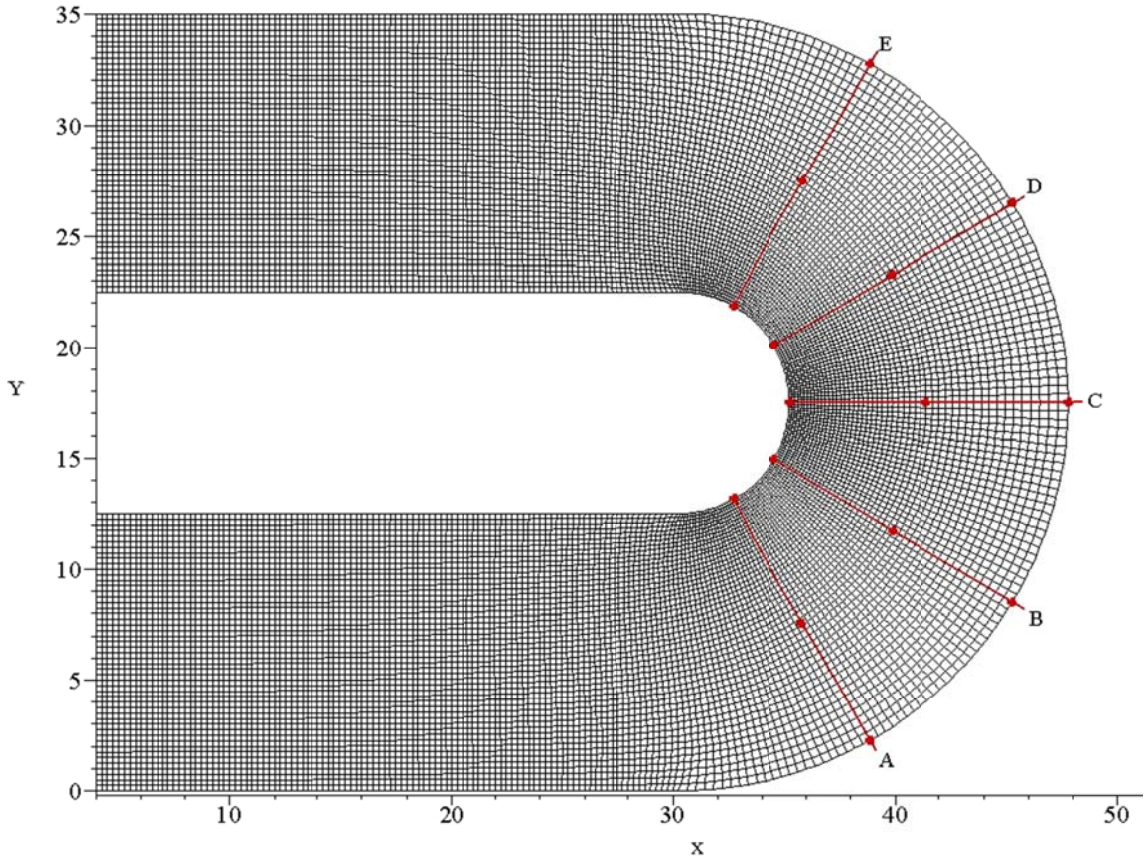

Figure 3- 14 The location of comparisons of time variation of free-surface elevation

Figure 3- 15 illustrates the comparisons of time varying free-surface elevations obtained from gB model and the present three-dimensional fully nonlinear model at the positions of “inner wall”, “center of channel”, and outer wall” in cross section A. The results indicate that both models predict similar wave variations including wave peak throughout the entire wave transformation process in the curved channel. There appears to have a slight phase difference between the computed wave profiles. This is mainly caused by the fundamental difference of the two models where one is the weakly nonlinear and weakly dispersive based gB model and the other is the present fully nonlinear based model. Also, different from the three-dimensional computation, the gB

model utilizes the vertically averaged velocity potential to determine the free-surface elevation. As a result, the two models generated slightly different phase velocities. It can be noticed in Figure 3- 15 that when the solitary wave propagates into the curved section and encounters the outer wall of the channel, the wave profile at the outer wall shows higher amplitude than that at the inner wall. After the solitary wave propagates past the cross section A, the wave amplitude keeps piling up at the outer wall and follows with wave reflection. Two wave peaks occurred at the channel center and inner wall are noticeable in Figure 3- 16 and Figure 3- 17.

As noted in Figure 3- 18 and Figure 3- 19, the continuing process of wave diffraction and reflection between the inner and outer walls at cross sections D and E suggests the occurrence of transverse wave oscillation and as a results generates multiple wave peaks at locations across the channel. Again, from the results presented in Figure 3- 16 to Figure 3- 19, both the gB and present nonlinear wave models obtain consistent and similar wave profiles. The comparison study for simulating a solitary wave propagating in a 180° curved channel further confirms the present three-dimensional fully nonlinear wave model can provide stable and accurate predictions on wave propagation and transformation.

The model is proved to be able to apply for simulating wave and structure interaction related problems. Two cases are investigated. One is a solitary wave interaction with a bottom mounted cylinder and the other is an interaction between a solitary wave and a fixed truncated cylinder. The results are presented in the following two chapters

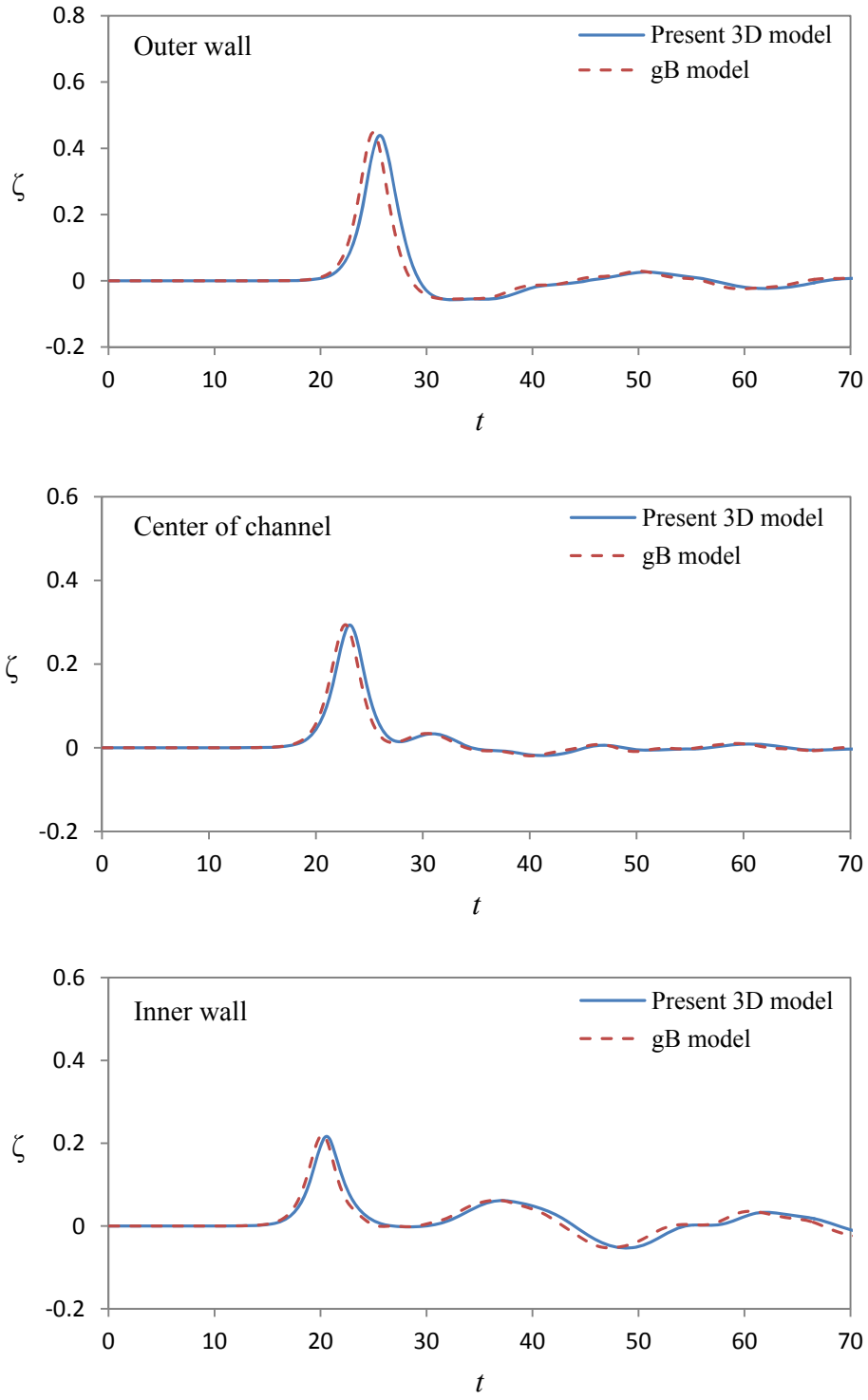

Figure 3- 15 Comparisons of time variations of free-surface elevations obtained from gB model and the present 3D fully nonlinear model at the positions of "outer wall", "center of channel", and "inner wall" in cross section A

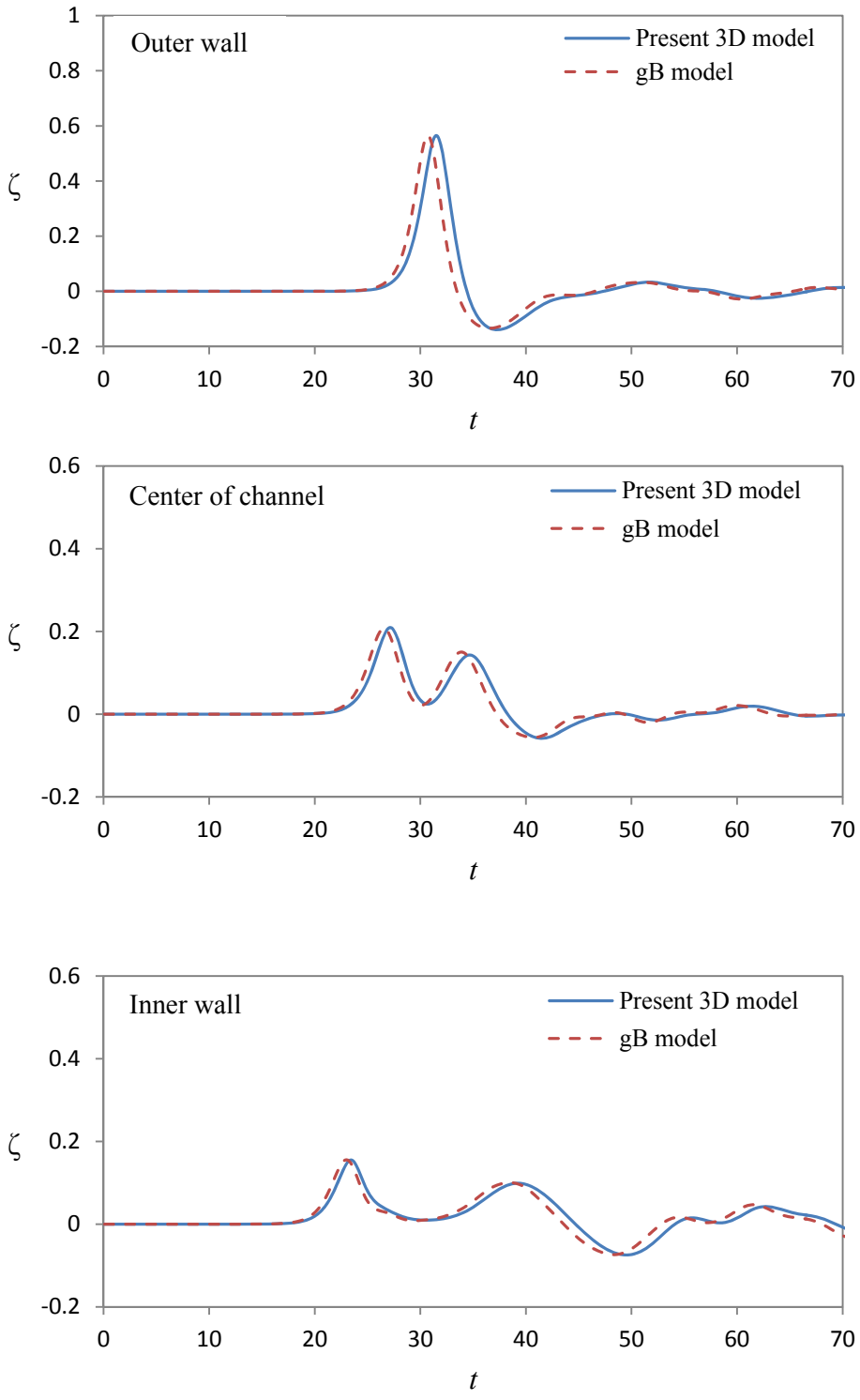

Figure 3- 16 Comparisons of time variations of free-surface elevations obtained from gB model and the present 3D fully nonlinear model at the positions of "outer wall", "center of channel", and "inner wall" in cross section B

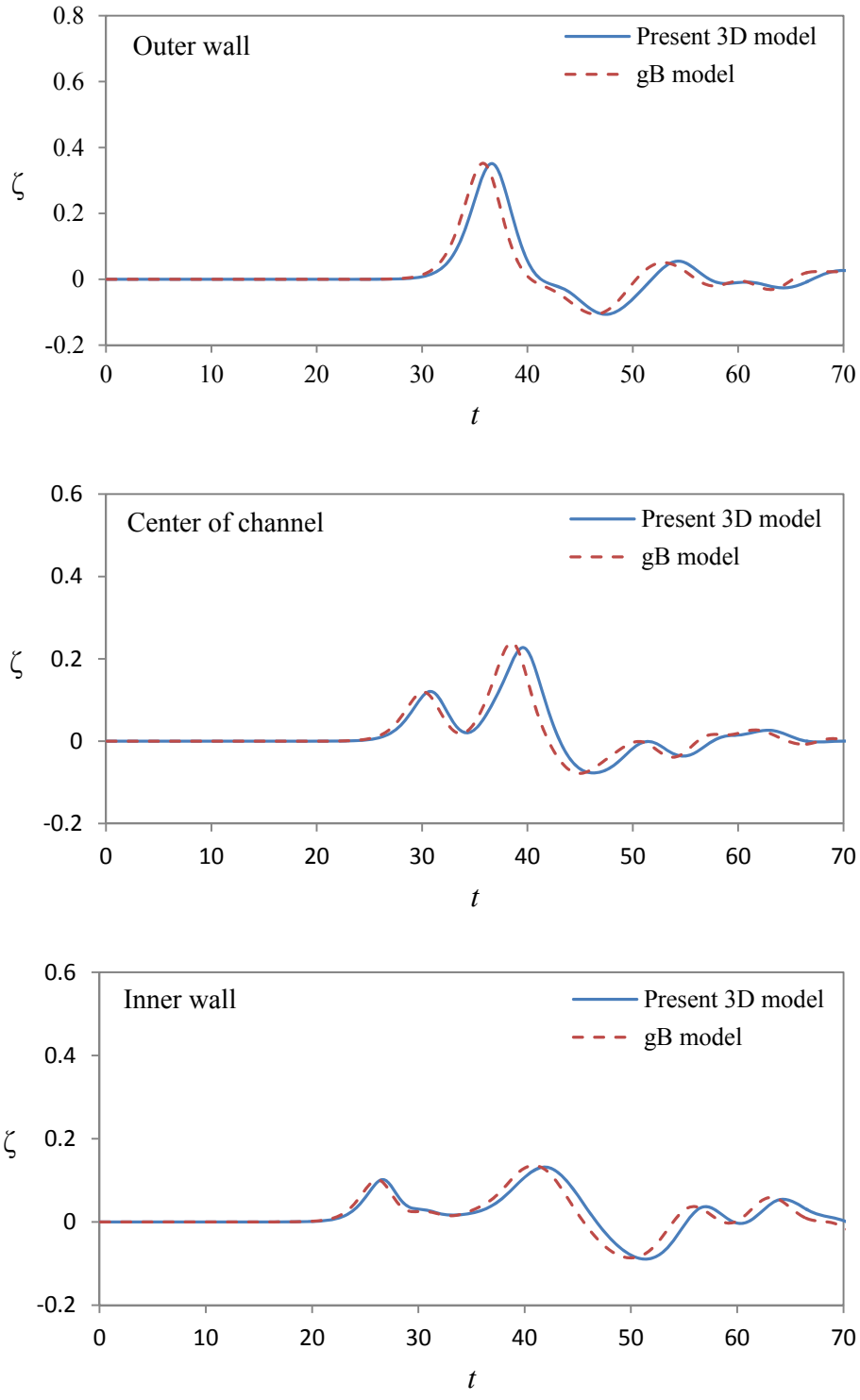

Figure 3- 17 Comparisons of time variations of free-surface elevations obtained from gB model and the present 3D fully nonlinear model at the positions of "outer wall", "center of channel", and "inner wall" in cross section C

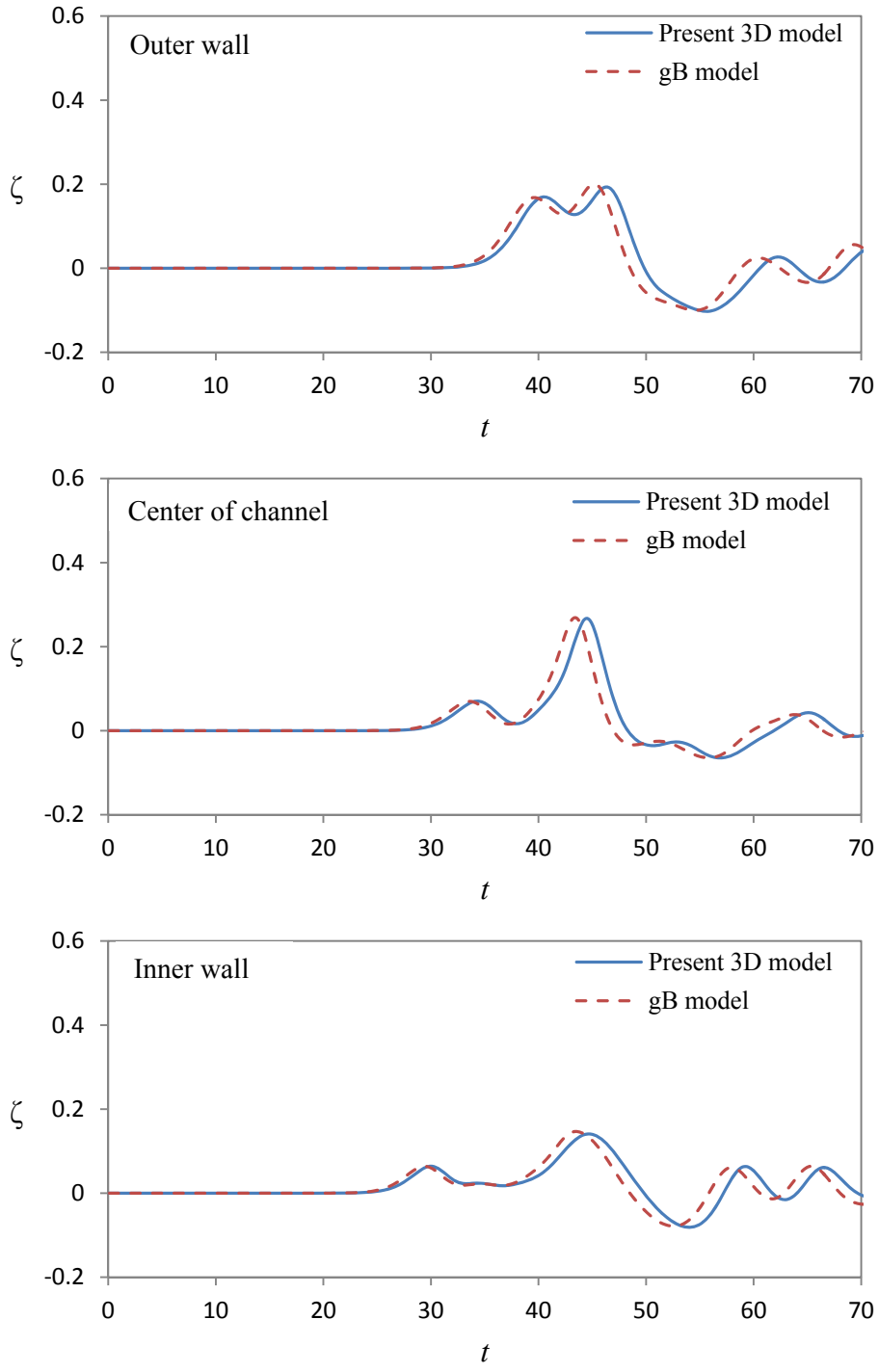

Figure 3- 18 Comparisons of time variations of free-surface elevations obtained from gB model and the present 3D fully nonlinear model at the positions of "outer wall", "center of channel", and "inner wall" in cross section D

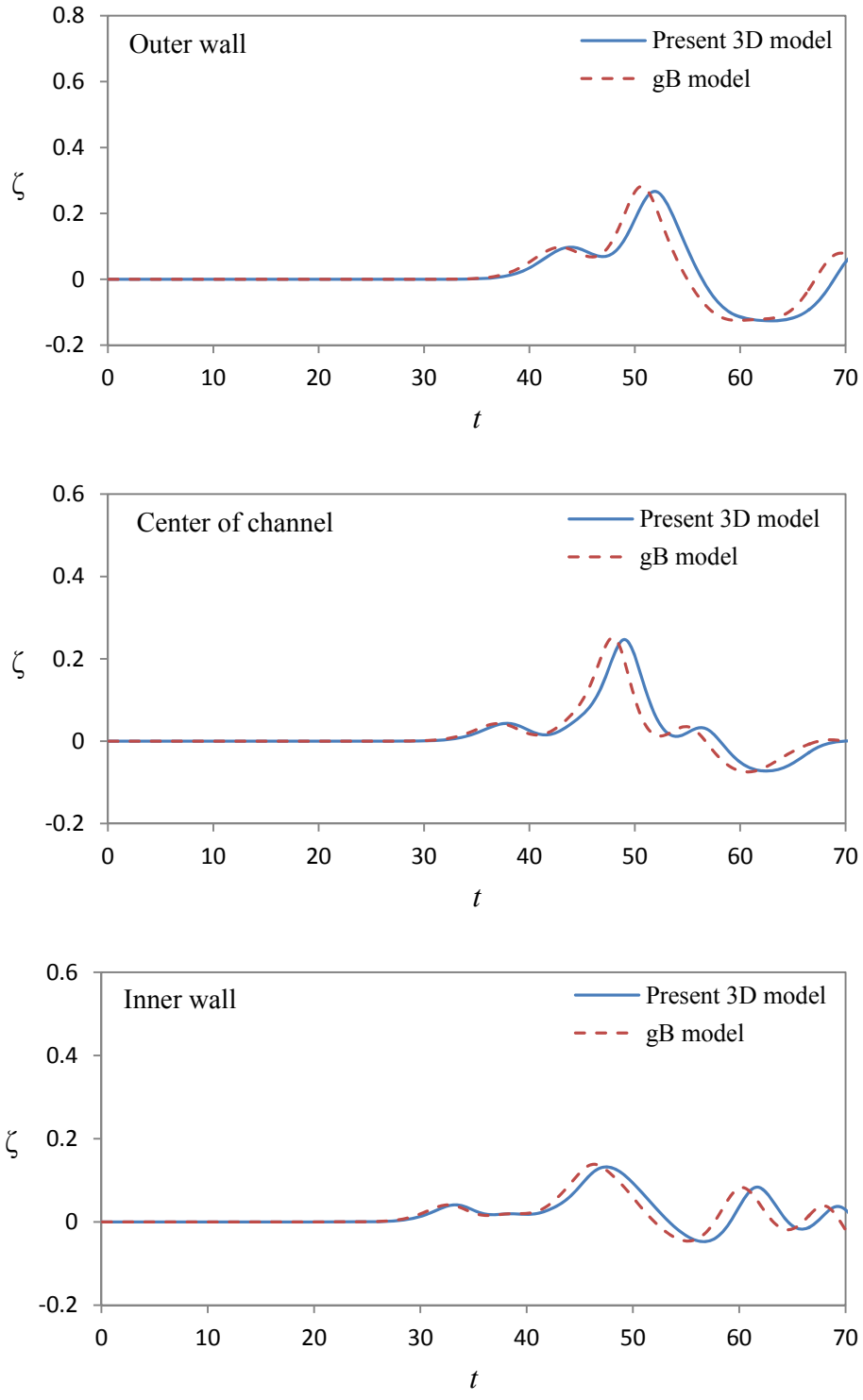

Figure 3- 19 Comparisons of time variations of free-surface elevations obtained from gB model and the present 3D fully nonlinear model at the positions of "outer wall", "center of channel", and "inner wall" in cross section E

Chapter 4

Solitary Waves Interacting with a and Bottom Mounted Surface Piercing Vertical Cylinder

In Chapter 3, as a verification of model performance the newly developed three-dimensional fully nonlinear wave model performed the simulations of a three-dimensional solitary wave propagating in a straight rectangular channel and a 180° curved channel. The studies of a solitary wave interacting with a cylindrical structure are also carried out using this developed model. The case presented in this chapter is a solitary wave encountering with a bottom mounted and surface-piercing vertical cylinder. The results obtained from this model are presented and compared with those from other models and measured data in literatures. The fluid domain with a vertical circular cylinder for this study is shown in Figure 4- 1.

According to the derivation of model equations given in Chapter 2, all variables described here for model simulations are dimensionless. The z-axis points upwards with the plane z=0 being located locates at the undisturbed free-surface. The domain bottom is assumed to be flat and its location is at $z = -1 =$ constant. The dimensionless radius of the cylinder (R) is 1.5875 and the cylinder is fixed at the center of the channel. The amplitude of the incident solitary wave is given as $\alpha = a/h_0^* = 0.4$. The values of the radius of the cylinder and the amplitude of the solitary wave are selected to be the same as those used in the experimental studies conducted by Yates and Wang (1994) for the

purpose of comparing the present numerical results with the experimental measurements. In this case, the two-grid system as introduced in Chapter 3 (Figure 3- 1) is applied for model simulations. The physical domain is $0 \leq x \leq 70$ and $0 \leq y \leq 35$. The sizes of rectangular grids in outer domain are $\Delta x = \Delta y = 0.25$ and the time step is set as $\Delta t = 0.1$. In order to capture the important phenomenon of wave interaction with structures in regions close to the cylinder, finer grids are arranged to cover these critical areas (see Figure 3- 1). The initial peak location of the solitary wave is set at $x_0 = 10$ where its distance to the upstream boundary is sufficient to establish a stable incident wave before encountering the cylinder. The results of time varying free-surface elevation and velocity potential during the interaction process are calculated by the present model for analysis.

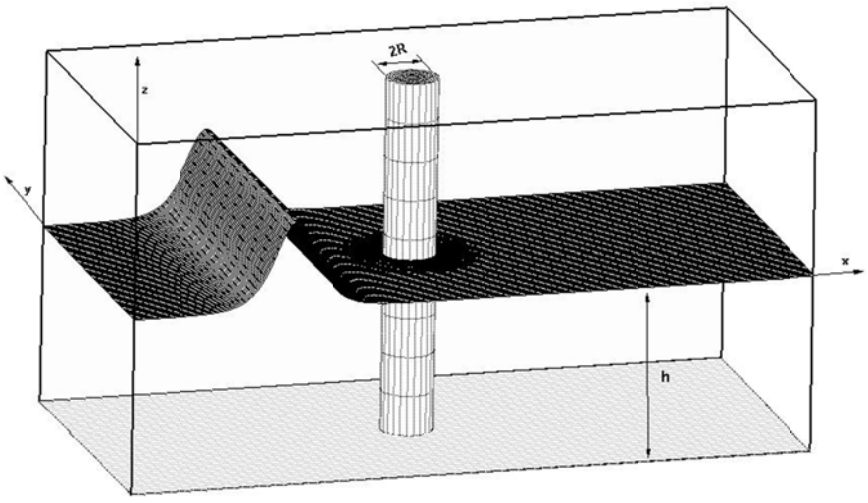

Figure 4- 1 Schematic diagram of initial solitary wave incident upon surface-piercing bottom mounted vertical cylinder

4.1 Interaction Process

Figure 4- 2 shows a time sequence of three-dimensional perspective view plots of the free-surface elevation for a solitary wave with amplitude $\alpha = 0.4$ propagating in a wave channel to impinge on a vertical cylinder. At $t = 10$, a simulated stable solitary wave as the incident wave can be noticed to propagate towards the bottom mounted vertical cylinder. While the peak of the solitary wave impacts on the cylinder at $t = 20$, the solitary wave piles up to the maximum value of the free-surface elevation in front of the cylinder surface. After the primary wave propagates past the cylinder, as shown at $t = 24$, the diffraction initiated backscattering and forward scattering waves are formed around the cylinder. Additionally, as part of the waves emerges as the back-scattered waves, the wave height of the central part of the primary waves is lower than the other parts of the primary waves after its impacting on the cylinder. However, it can still keep the same propagating speed with other primary waves. At $t = 25$, the scattered wave around the cylinder continue propagating outwards and the wave profile of the central part of the primary waves is shown the tendency to recover its initial shape of the incident solitary wave. An apparent secondary scattered wave that follows the leading back-scattered wave is observed propagating outwards at $t = 31$. While the solitary wave propagates over 20 water depths beyond the cylinder at $t = 40$, a group of scattered waves travel further away from the cylinder and expand over the upstream and downstream regions of the cylinder. Moreover, the central part of the primary wave transitions back to nearly its original amplitude and as a whole the wave recovers as a solitary wave propagating downstream. Similar features of wave-cylinder interactions

have also been found in the studies by Wang et al. (1992), Zhong and Wang (2008), and Kang et al. (2015).

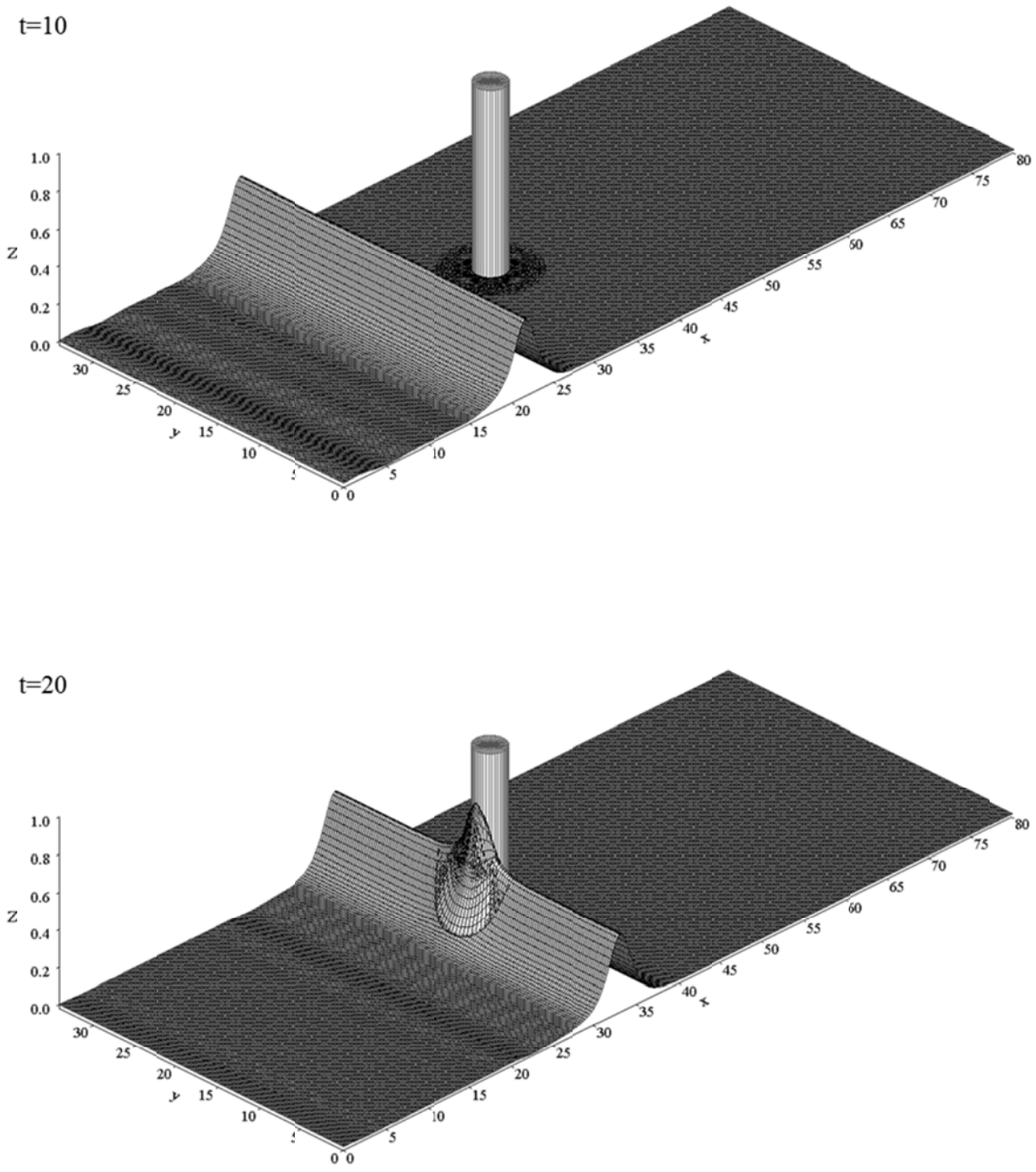

Figure 4- 2 Three-dimensional perspective view plot of free-surface elevation ζ for $\alpha = 0.4$ at selected instants of time

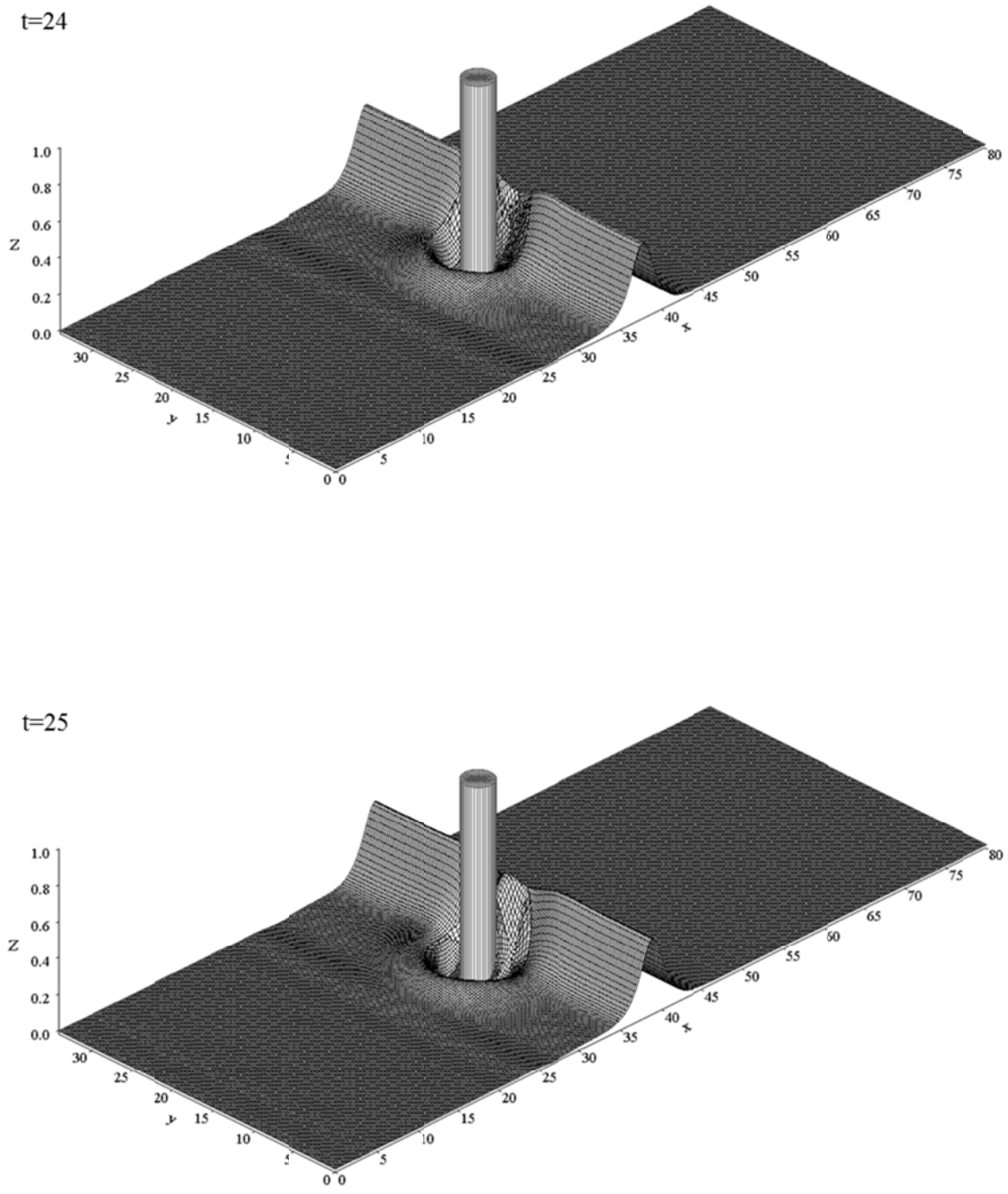

Figure 4- 2 Three-dimensional perspective view plot of free-surface elevation ζ for $\alpha = 0.4$ at selected instants of time (Continued)

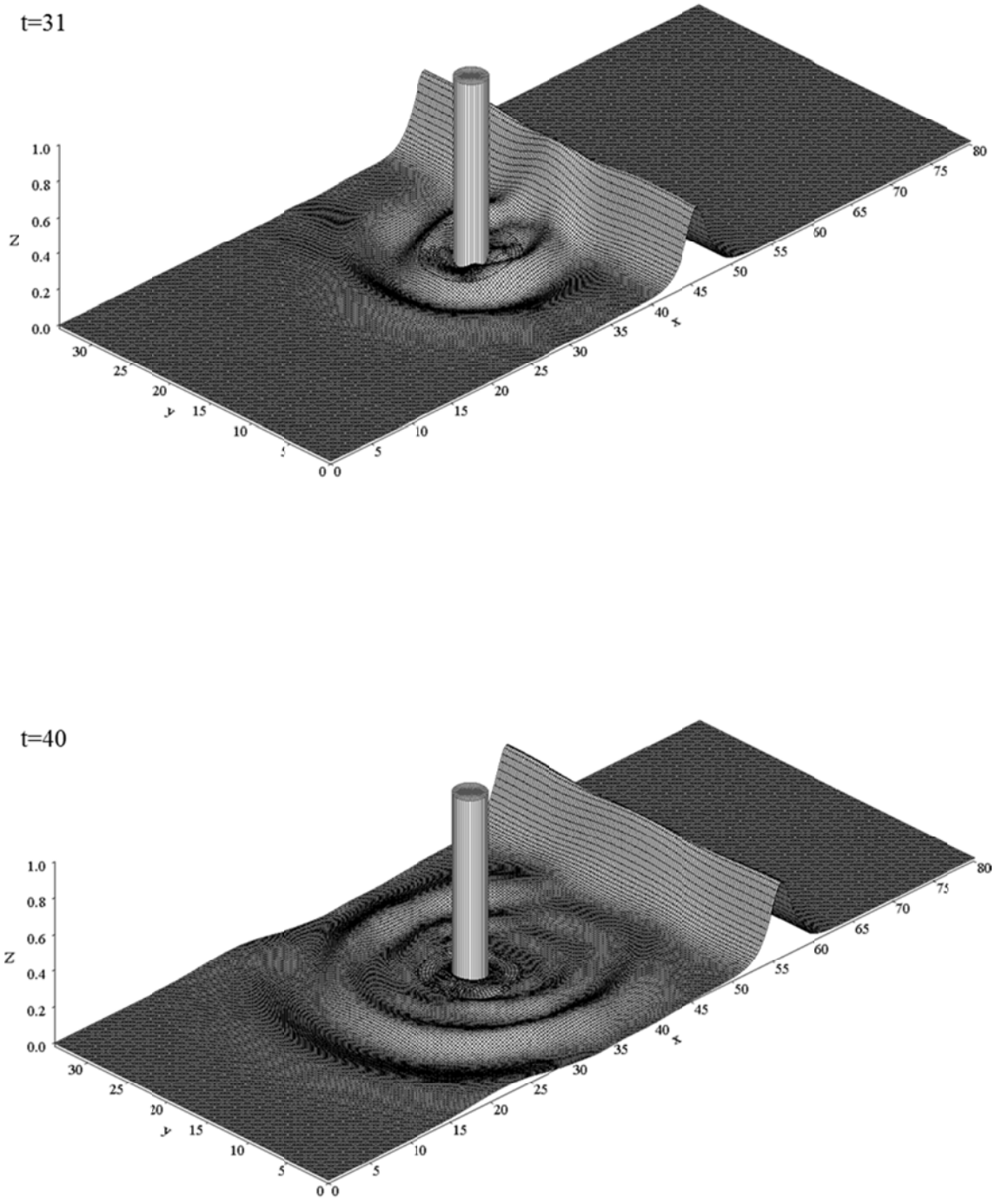

Figure 4- 2 Three-dimensional perspective view plot of free-surface elevation ζ for $\alpha = 0.4$ at selected instants of time (Continued)

Figure 4- 3 illustrates a contour plot of the free-surface elevation to show the diffraction pattern at $t = 40$ where the main solitary wave after the interacting process is in a position further downstream of the cylinder. The solid lines and dash lines in the figure represent the positive and negative values of the free-surface, respectively. From Figure 4- 3, we noticed that a sequence of outward-propagating scattered waves around the cylinder can be clearly observed and are shown to is nearly have the wave patterns similar to the circular belts concentric to the cylinder. In addition, the primary wave is nearly recovered as a pane solitary wave.

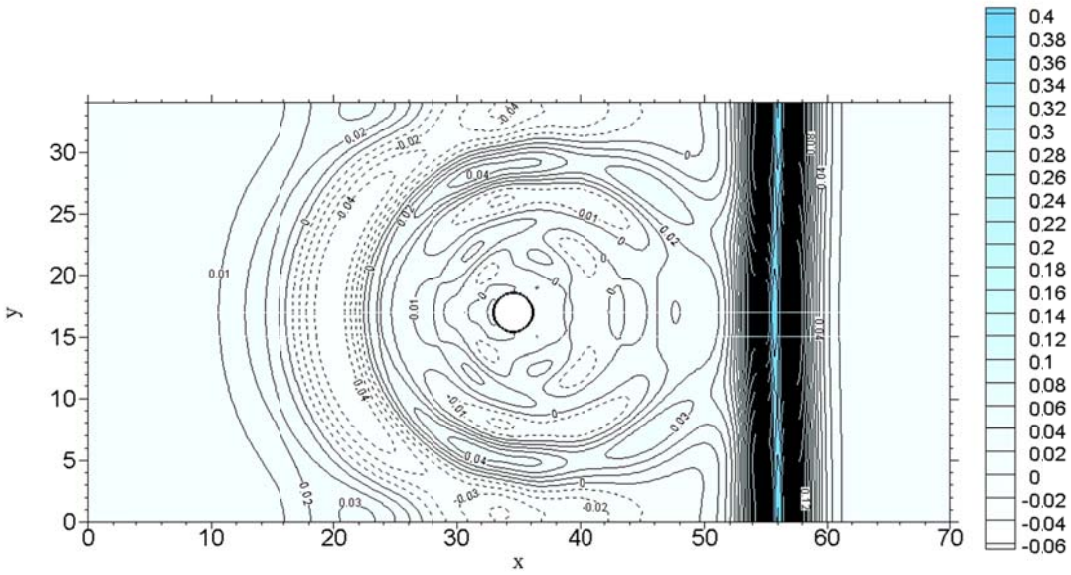

Figure 4- 3 Contour plot of the free-surface elevation for amplitude of a solitary wave α=0.4 and cylinder diameter R =1.5875 at t=40

4.2 Comparisons of the Present Model Results with Other Published Solutions and Experimental Data

The performance of the present model in simulating the interaction between a solitary wave and a bottom mounted and surface-piercing vertical cylinder is examined by comparing the model results with other published solutions and the experimental data. The other published results include the finite difference solutions of the weakly nonlinear and weakly dispersive generalized Boussinesq (gB-FDM) model (Wang et al., 1992), and experimental data from Yates and Wang (1994). The selected locations for the comparisons of free-surface elevation are the same as the gauge locations used in the Yates and Wang (1994) experimental study. The gauge locations are expressed with the polar angle θ, and the dimensionless radial distance r/R, where R is the radius of the cylinder. Figure 4- 4 presents the wave elevations in time series at four selected radial locations along the $\theta = 0°$ line, where $\theta = 0°$ denotes the direction pointing toward the negative x direction. The comparison plots at selected radial locations along $\theta = 60°$, $100°$, $150°$, and $180°$ following the clockwise direction are shown in Figure 4- 5, Figure 4- 6, Figure 4- 7, and Figure 4- 8, respectively.

In Figure 4- 4 (a) to 4-4 (d), the wave profiles at the radial location of r/R =4.5, 2.61, 1.66, and 1.03 are presented. The incident solitary wave with an amplitude of $\alpha = 0.4$ is shown to propagate past the position of $r/R = 4.5$ and is followed with a reflected wave and a train of small oscillatory waves after impacting on the cylinder, [Figure 4- 4 (a) and (b)]. At a position close to the cylinder surface ($r/R = 1.03$), Figure 4- 4(d) reveals that the solitary wave piles up to the maximum amplitude in front of the cylinder and is followed with a negative wave propagating radially outward from the

cylinder surface. It can be noticed that the amplitude of the main wave also shown to increase at $r/R = 1.66$ [Figure 4- 4 (c)], although is less than the value at $r/R = 1.03$. The similar variation trends of the free-surface elevations at the location of $r/R = 3.87$, 2.92, 2.29, and 1.35 and along $\theta = 60°$ direction can also be found in Figure 4- 5 (a) to Figure 4- 5 (d).

The comparisons shown in Figure 4- 4 and Figure 4- 5 indicate that the present model, and the published finite difference gB model produce similar results. Both model predictions are also shown to agree reasonably well with the experimental data, especially the main wave profile. From the figures, it is noticed that the maximum amplitudes can be accurately predicted by the developed three-dimensional fully nonlinear wave model while comparing to the maximum amplitudes of the experimental data at the positions away from the cylinder surface. When at the position nearly on the cylinder surface, both models overestimate the maximum wave amplitude. The present nonlinear wave model can capture well the variation trends of the free-surface profile at position along $\theta = 60°$ direction.

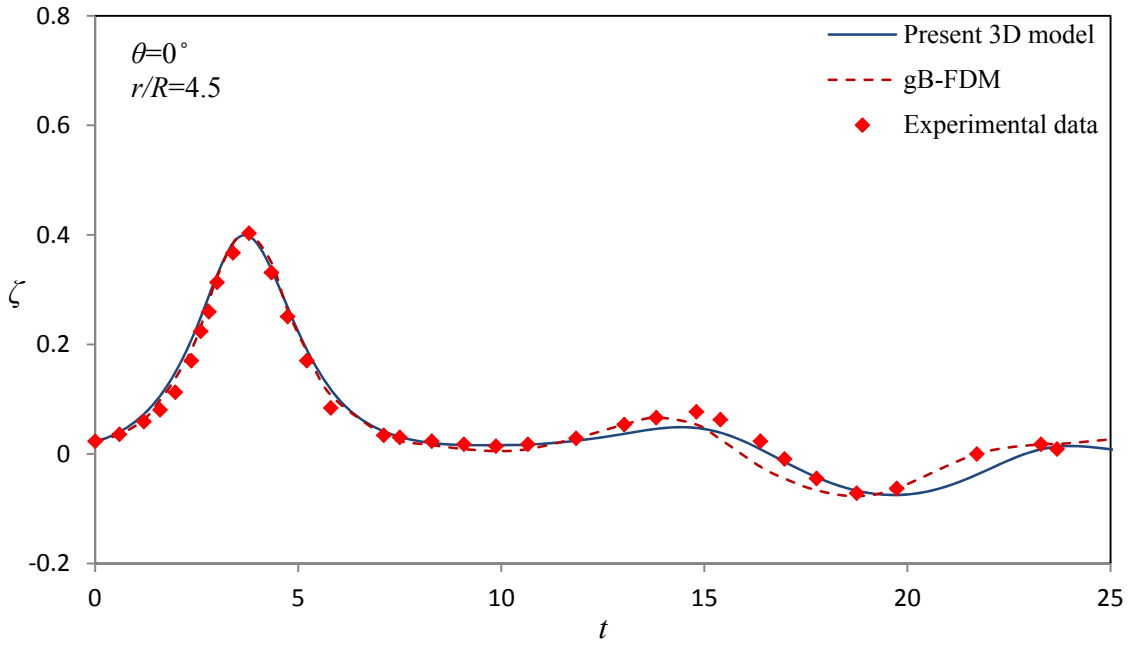

(a)

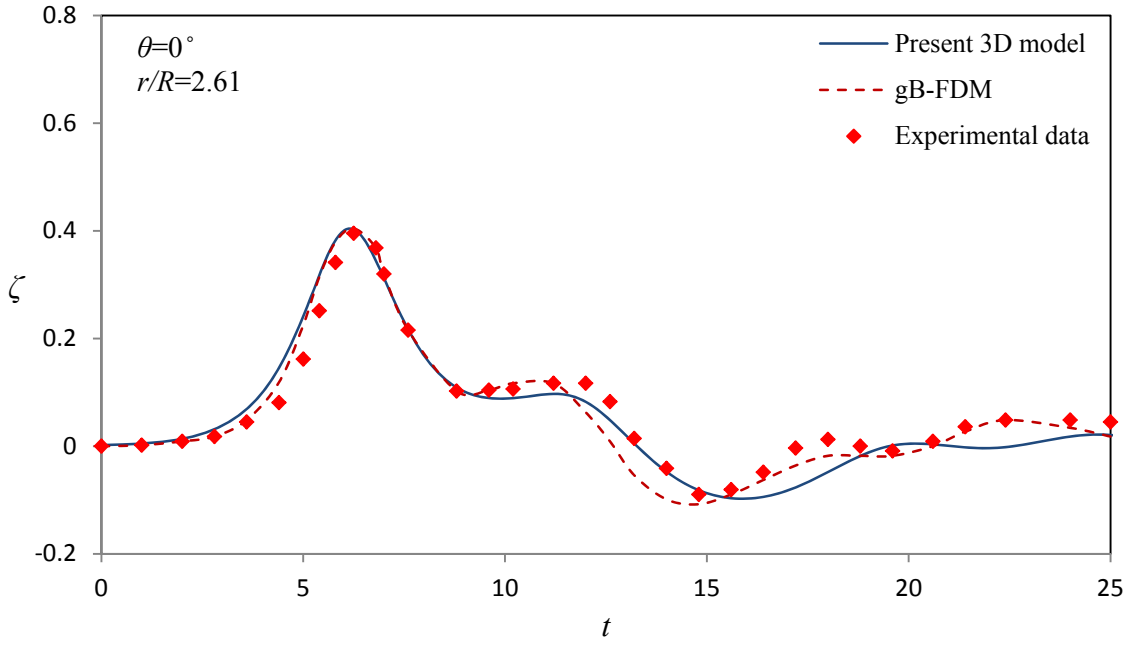

(b)

Figure 4- 4 Comparisons of time variation of free-surface elevation along $\theta = 0^{\circ}$ at (a) r/R=4.5 and (b) r/R=2.61 obtained from the present 3D nonlinear model, the gB-FDM (Wang et al., 1992), and experimental data (Yetes and Wang, 1994)

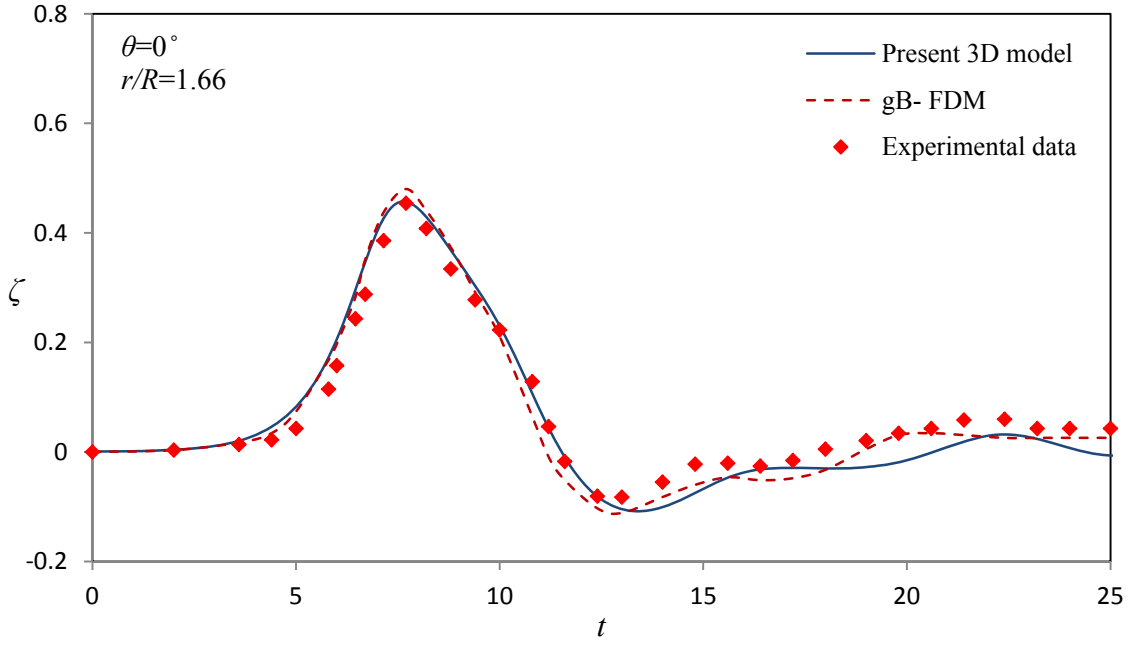

(c)

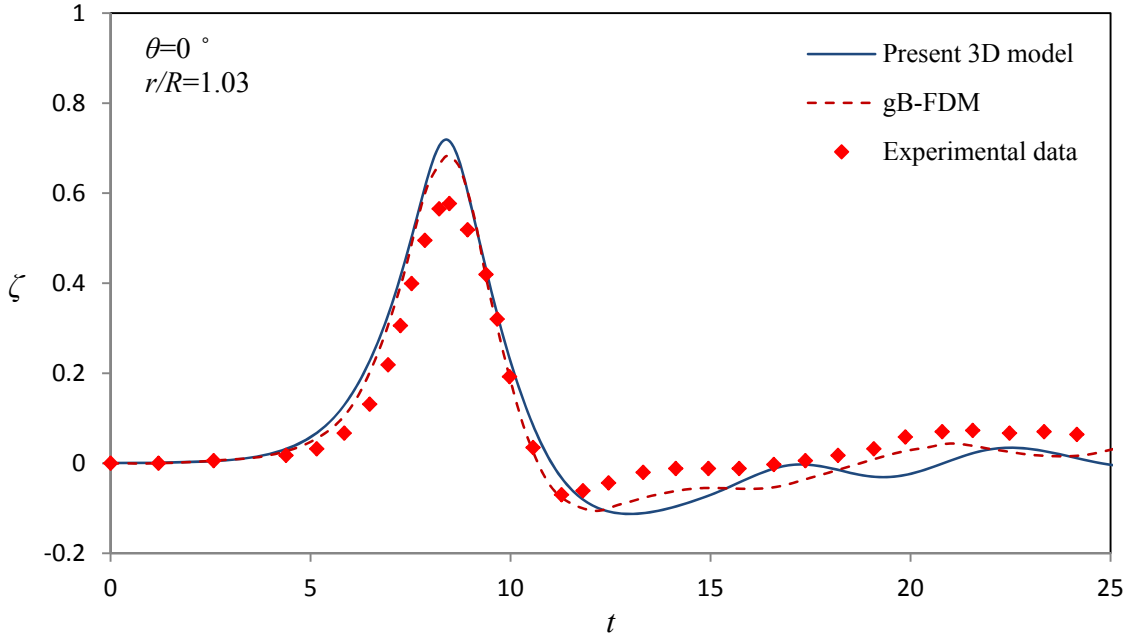

(d)

Figure 4- 4 Comparisons of time variation of free-surface elevation along θ = 0° at (c) r/R=1.66 and (d) r/R=1.03 obtained from the present 3D nonlinear model, the gB-FDM (Wang et al., 1992), and experimental data (Yetes and Wang, 1994) (Continued)

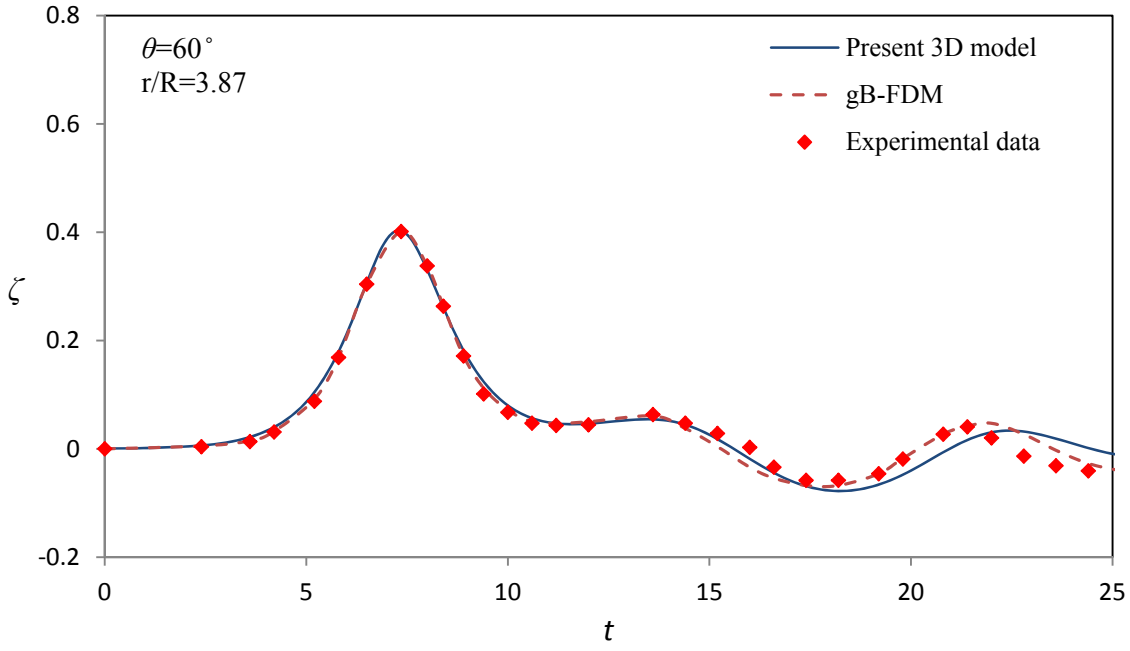

(a)

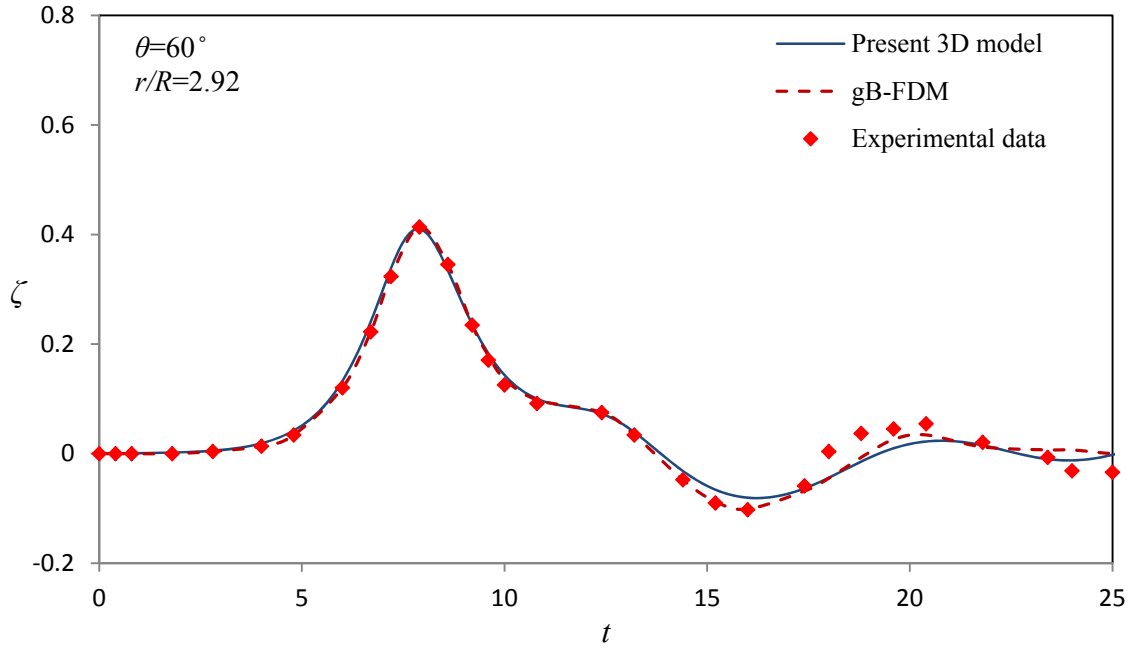

(b)

Figure 4- 5 Comparisons of time variation of free-surface elevation along θ = 60° at (a) r/R=3.87 and (b) r/R=2.92 obtained from the present 3D nonlinear model, the gB-FDM (Wang et al., 1992), and experimental data (Yetes and Wang, 1994)

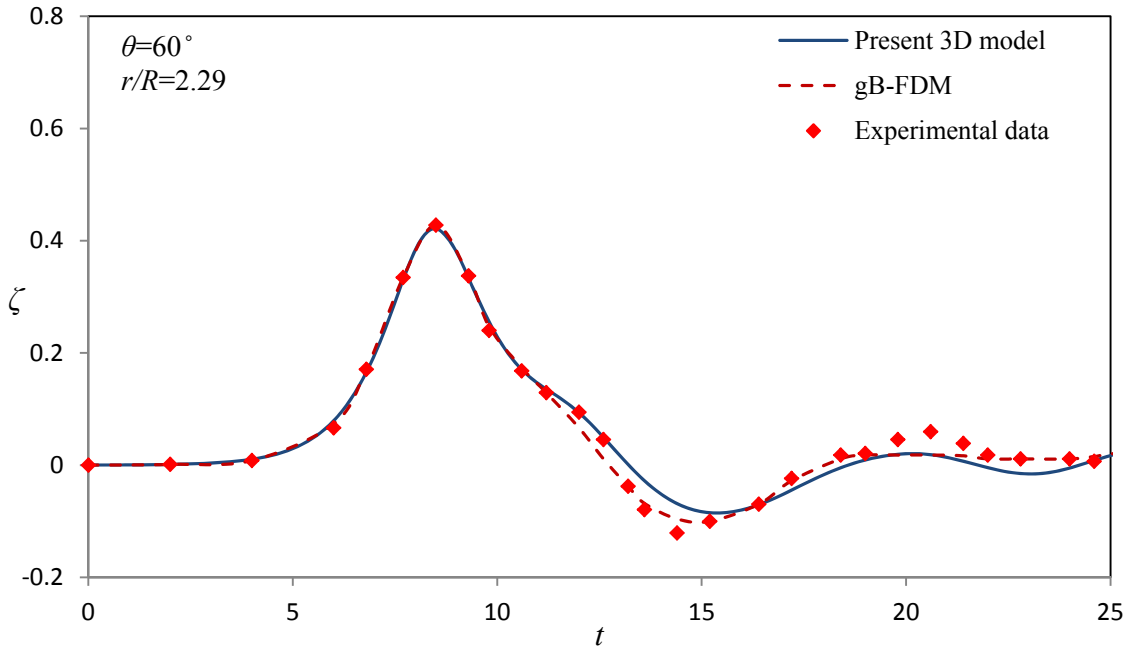

(c)

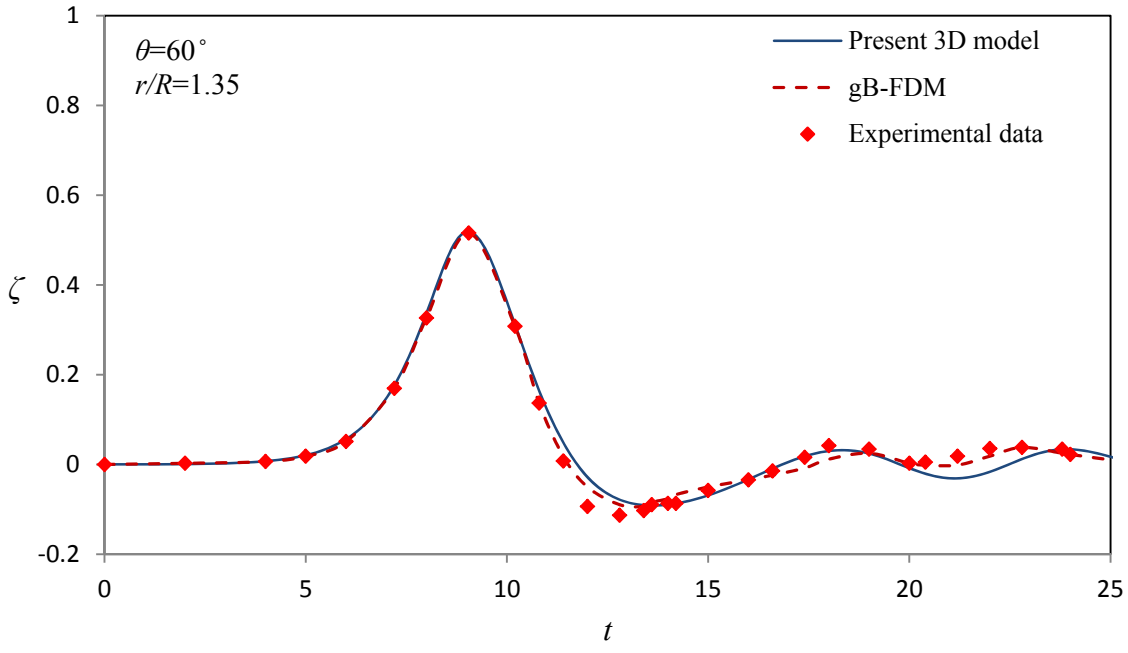

(d)

Figure 4- 5 Comparisons of time variation of free-surface elevation along θ = 60° at (c) r/R=2.29 and (d) r/R=1.35 obtained from the present 3D nonlinear model, the gB-FDM (Wang et al., 1992), and experimental data (Yetes and Wang, 1994) (Continued)

Figure 4- 6 to Figure 4- 8 illustrate the comparisons between the computed and measured free-surface profiles on the rear side of the cylinder. The wave profiles include a main solitary wave followed with a group of forward-scattered waves. Figure 4- 6 shows the variations of the free-surface along the radial line of $\theta = 100°$. The present model predictions agree well with measured data at the location of $r/R = 1.35$, 2.29, and 2.92. At the closest location to the cylinder, namely at $r/R = 1.03$, the present model again produces a reasonably over-estimated wave amplitude. However, the overall variation trends of the wave elevation are similar to the measured data. The similar phenomena in terms of predicted wave profiles can also be found along the directions of $\theta = 150°$ (Figure 4- 7) and at $\theta = 180°$ (Figure 4- 8). The present model can provide good predictions on the wave elevations at locations away from the cylinder. The mismatch of the amplitude predictions for waves at the location almost on the cylinder surface ($r/R = 1.03$) may be caused by the measurement errors and potential viscous and flow separation effects, which are not included in the model formulations. Along the direction of $\theta = 180°$ (Figure 4- 8), it is interesting to note that the present fully nonlinear model can better predict at the general trend of wave variation and the tail part of the main wave. Also shown in Figure 4- 8, when the main wave propagates past the cylinder, the wave amplitude in the region behind the cylinder decreases until later recovers to nearly the original amplitude. It is demonstrated from this comparison study the present three-dimensional nonlinear wave model in general can make similar on or better predictions on free-surface variations of a solitary wave interacting with a bottom-mounted and surface piercing cylinder when compared to the results obtained from gB model.

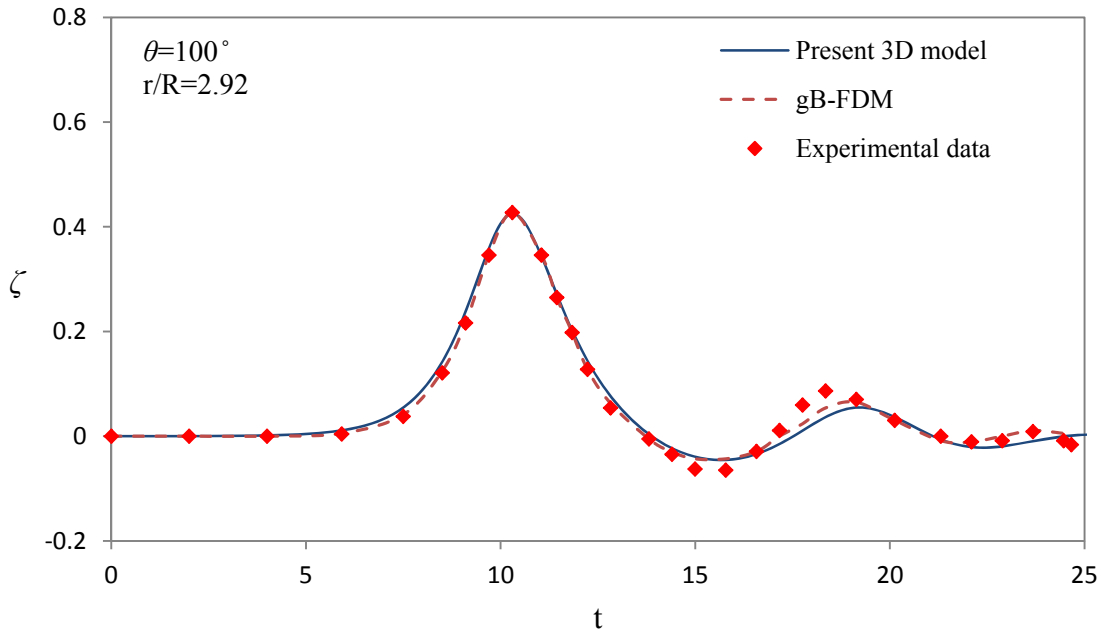

(a)

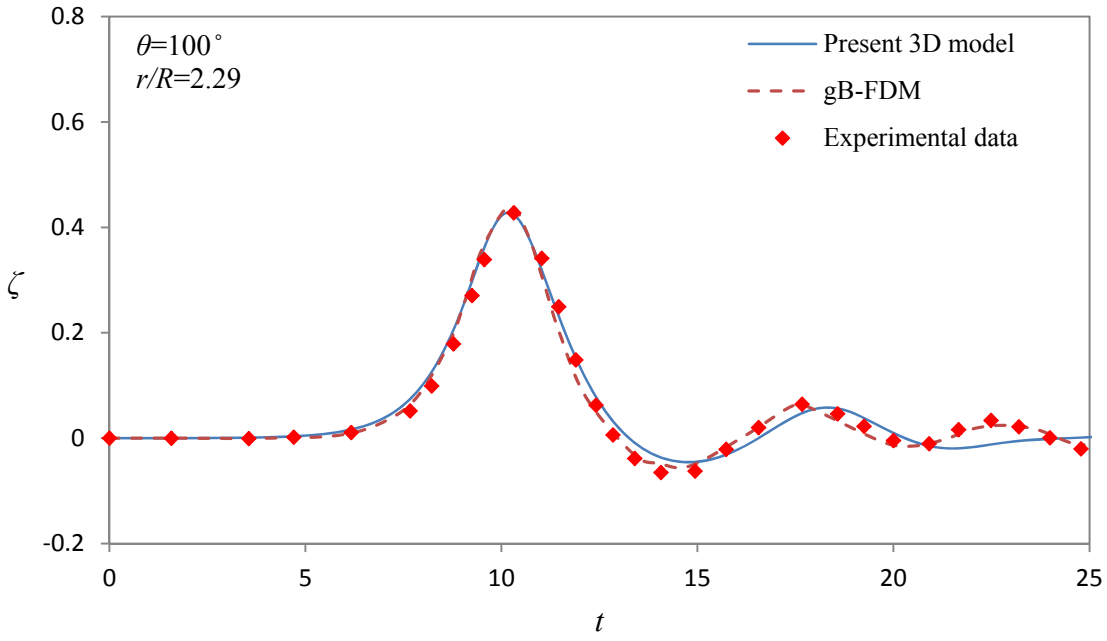

(b)

Figure 4- 6 Comparisons of time variation of free-surface elevation along $\theta = 100^{\circ}$ at (a) r/R=2.92 and (b) r/R=2.29 obtained from the present 3D nonlinear model, the gB-FDM (Wang et al., 1992), and experimental data (Yetes and Wang, 1994)

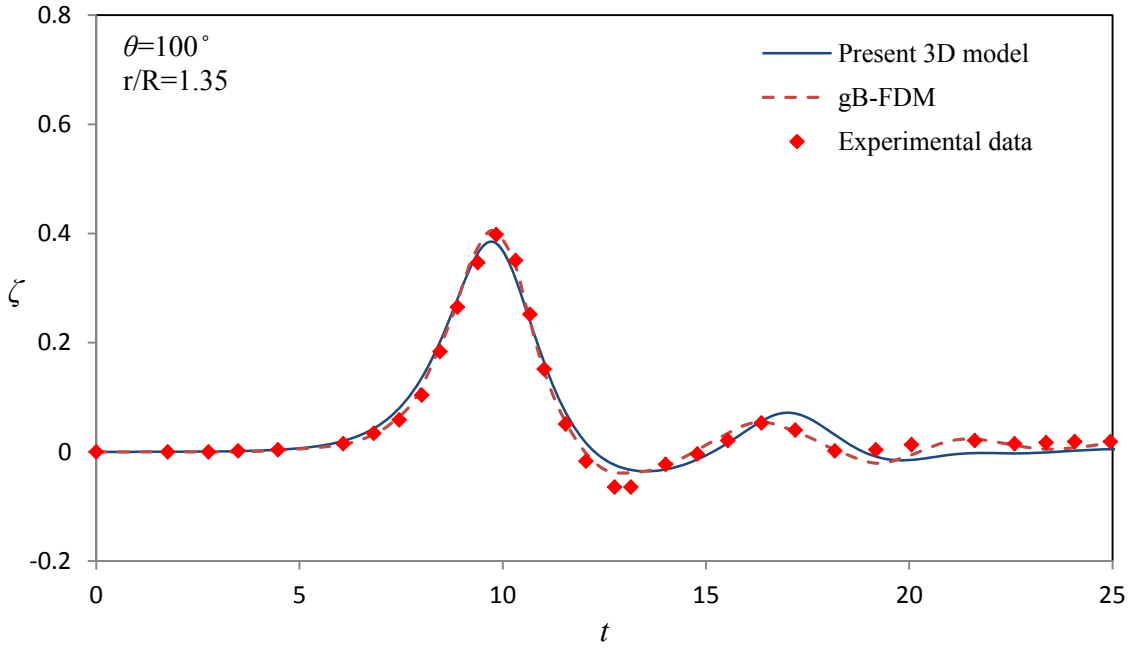

(c)

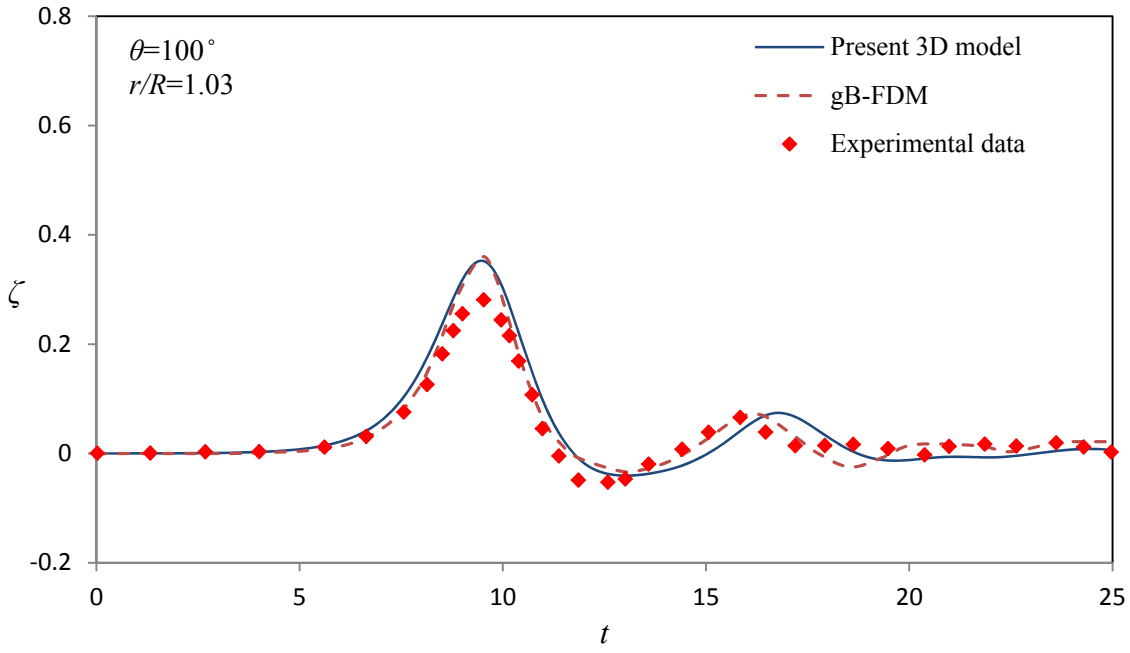

(d)

Figure 4- 6 Comparisons of time variation of free-surface elevation along θ = 100° at (c) r/R=1.35 and (d) r/R=1.03 obtained from the present 3D nonlinear model, the gB-FDM (Wang et al., 1992), and experimental data (Yetes and Wang, 1994) (Continued)

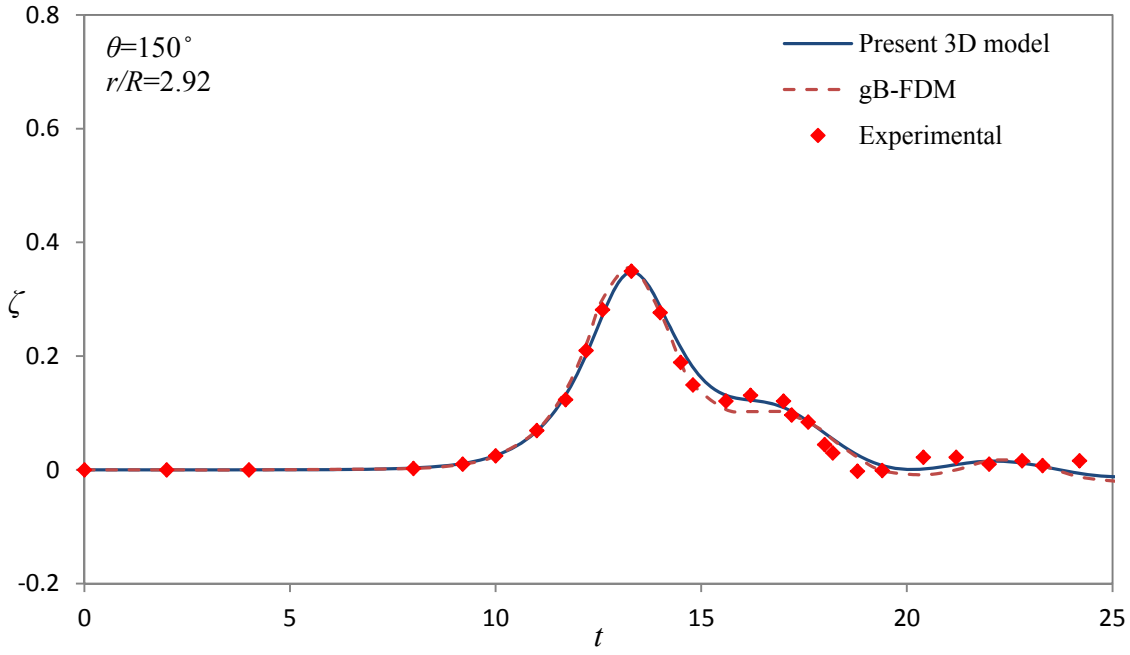

(a)

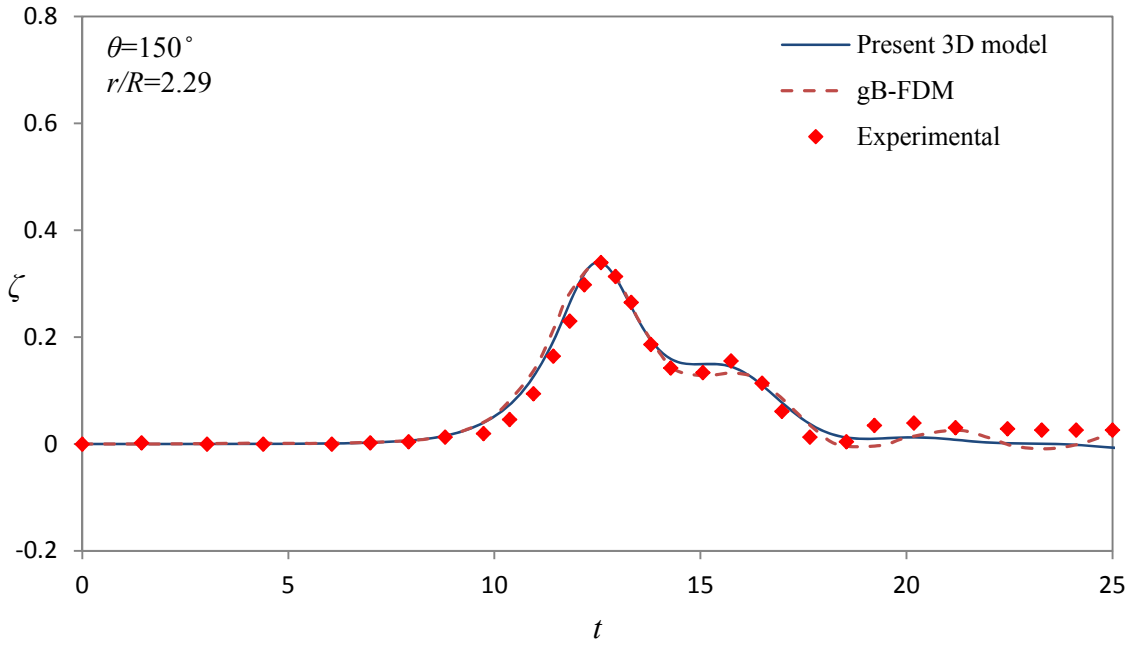

(b)

Figure 4- 7 Comparisons of time variation of free-surface elevation along θ = 150° at (a) r/R=2.92 and (b) r/R=2.29 obtained from the present 3D nonlinear model, the gB-FDM (Wang et al., 1992), and experimental data (Yetes and Wang, 1994)

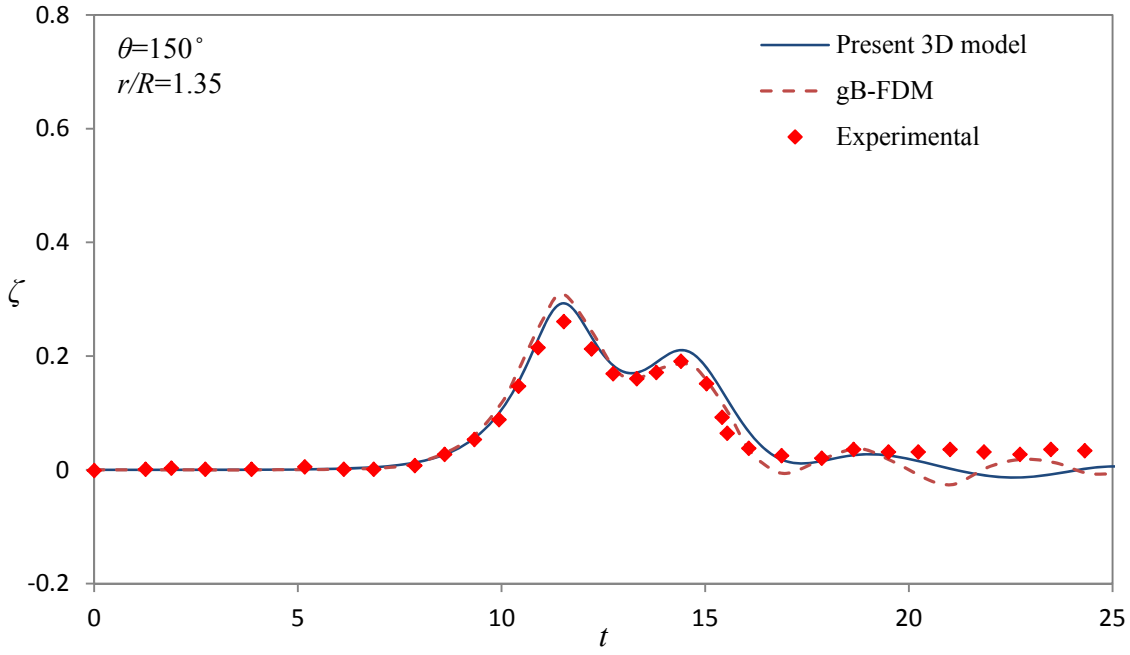

(c)

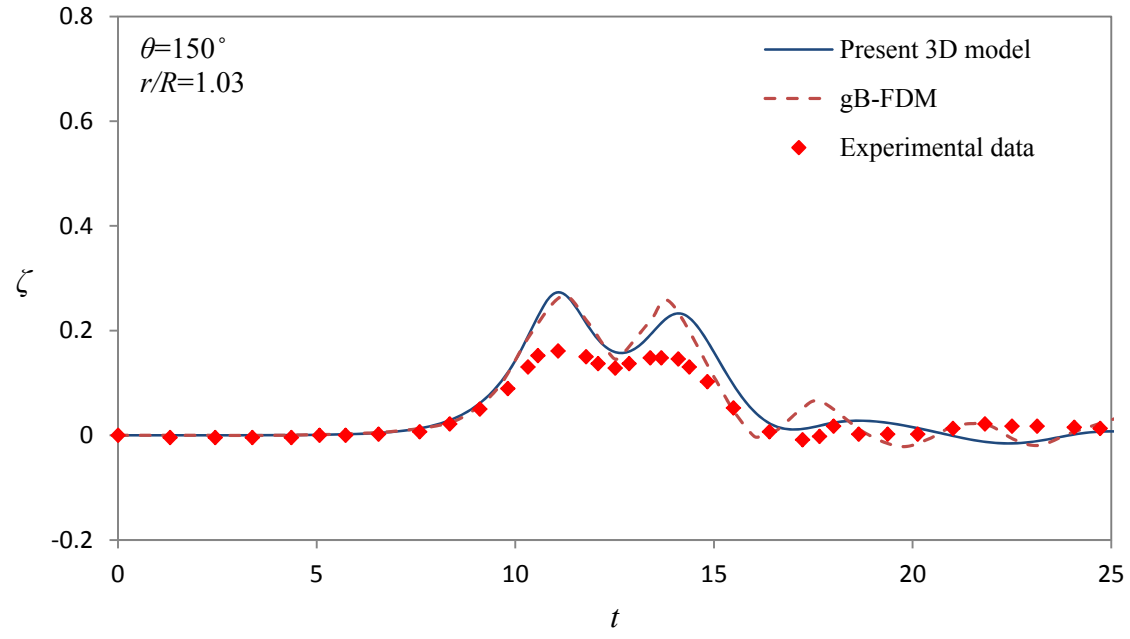

(d)

Figure 4- 7 Comparisons of time variation of free-surface elevation along θ = 150° at (c) r/R=1.35 and (d) r/R=1.03 obtained from the present 3D nonlinear model, the gB-FDM (Wang et al., 1992), and experimental data (Yetes and Wang, 1994) (Continued)

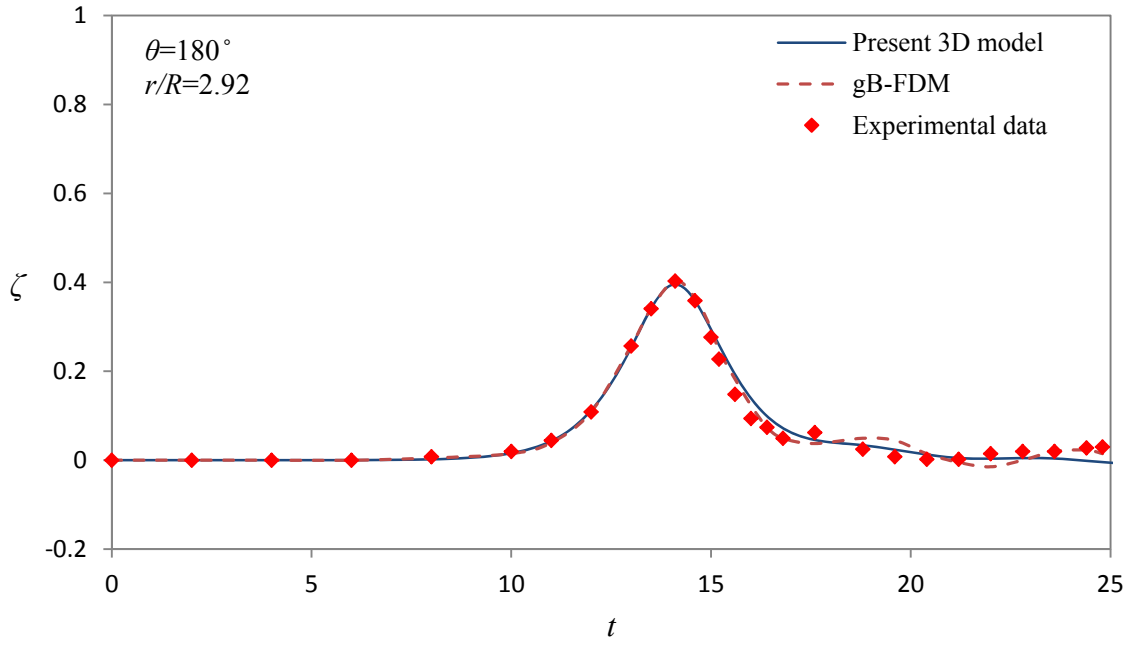

(a)

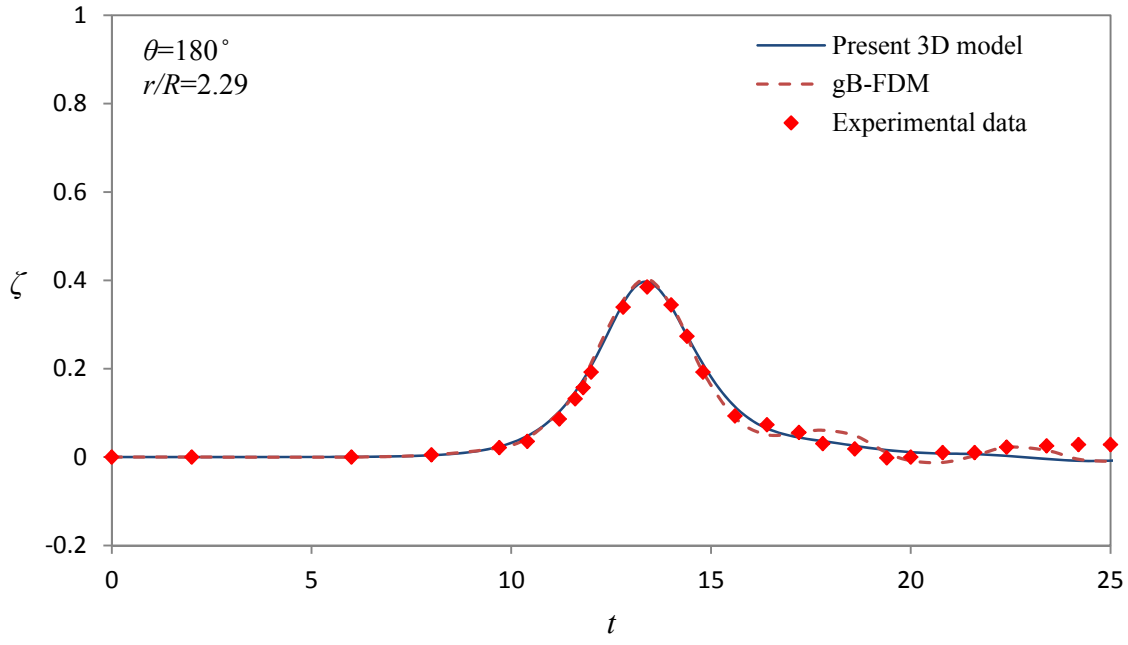

(b)

Figure 4- 8 Comparisons of time variation of free-surface elevation along θ = 180° at (a) r/R=2.92 and (b) r/R=2.29 obtained from the present 3D nonlinear model, the gB-FDM (Wang et al., 1992), and experimental data (Yetes and Wang, 1994)

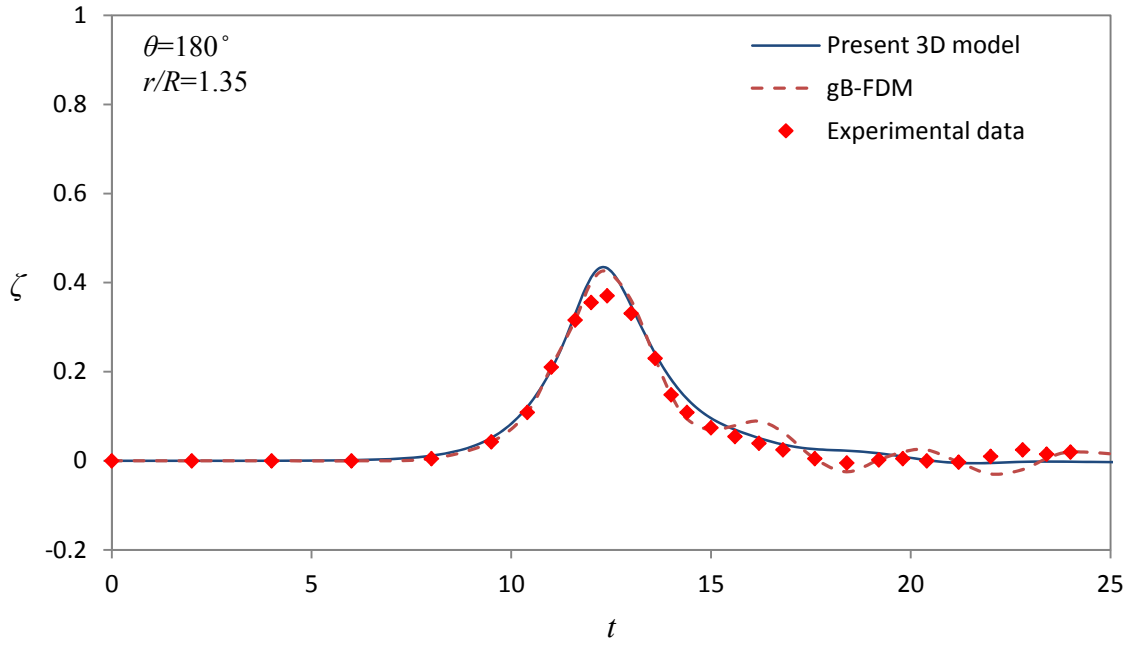

(c)

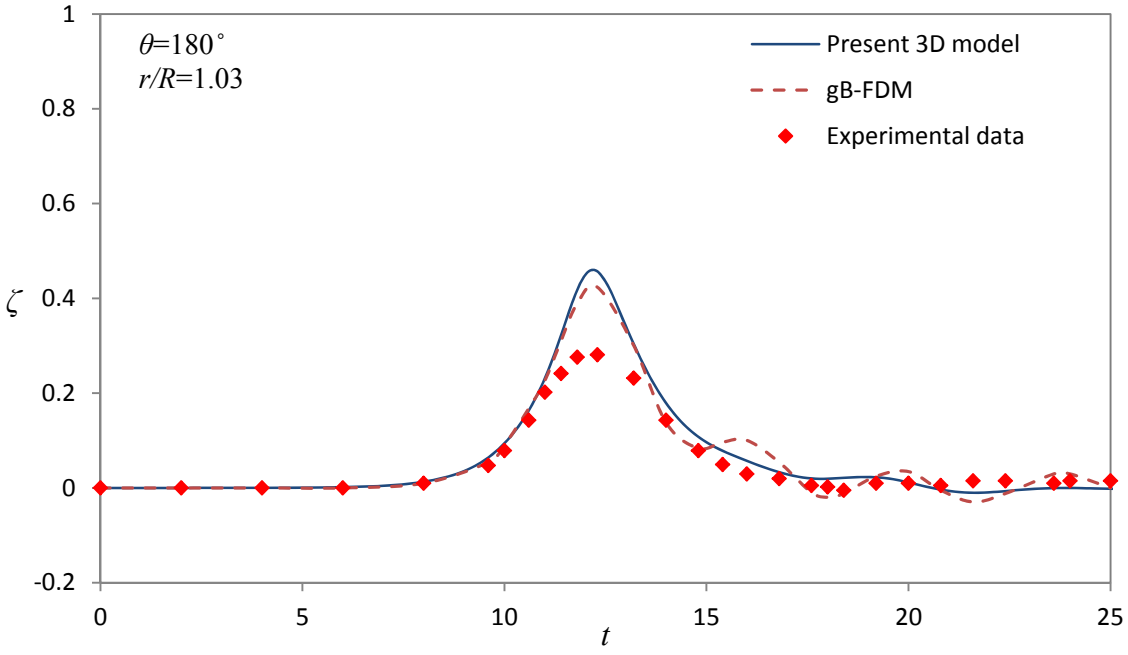

(d)

Figure 4- 8 Comparisons of time variation of free-surface elevation along θ = 180° at (c) r/R=1.35 and (d) r/R=1.03 obtained from the present 3D nonlinear model, the gB-FDM (Wang et al., 1992), and experimental data (Yetes and Wang, 1994) (Continued)

The hydrodynamic forces of solitary waves acting on the surface of cylinder can be determined by integrating the dynamic pressures on the cylinder surface. For the convenience of force comparisons, they are presented as the dimensionless force coefficients calculated by Equation (2- 21). The comparisons of the time varying force coefficients obtained from the present model, gB approach, and experimental measurements for different incident wave amplitude $\alpha = 0.18$, 0.24, 0.32, and 0.4 are given in Figure 4- 9 (a), Figure 4- 9 (b), Figure 4- 9 (c), and Figure 4- 9 (d), respectively. In Figure 4- 9 (a), when $\alpha = 0.18$, we notice the results from both the present three-dimensional model and gB-FDM match closely with the measured forces. Reasonable force predictions for the case of $\alpha = 0.24$ can be found in Figure 4- 9 (b). As the amplitude of the incident wave increases, namely $\alpha = 0.32$ and 0.4, the results in Figure 4- 9 (c) and 4-9 (d) indicate that both the present fully nonlinear wave model and gB-FDM overpredict the maximum force. The smaller measured maximum forces may be caused by the viscous and boundary layer effects and the small gap set between the bottom of the cylinder and the channel bottom for wave force measurements. It is to note the interaction time and associated phase calculated by the present model shows slightly more accurate than that from gB-FDM. In addition, the maximum negative forces determined by the present three-dimensional model are close to the experimental measurements.

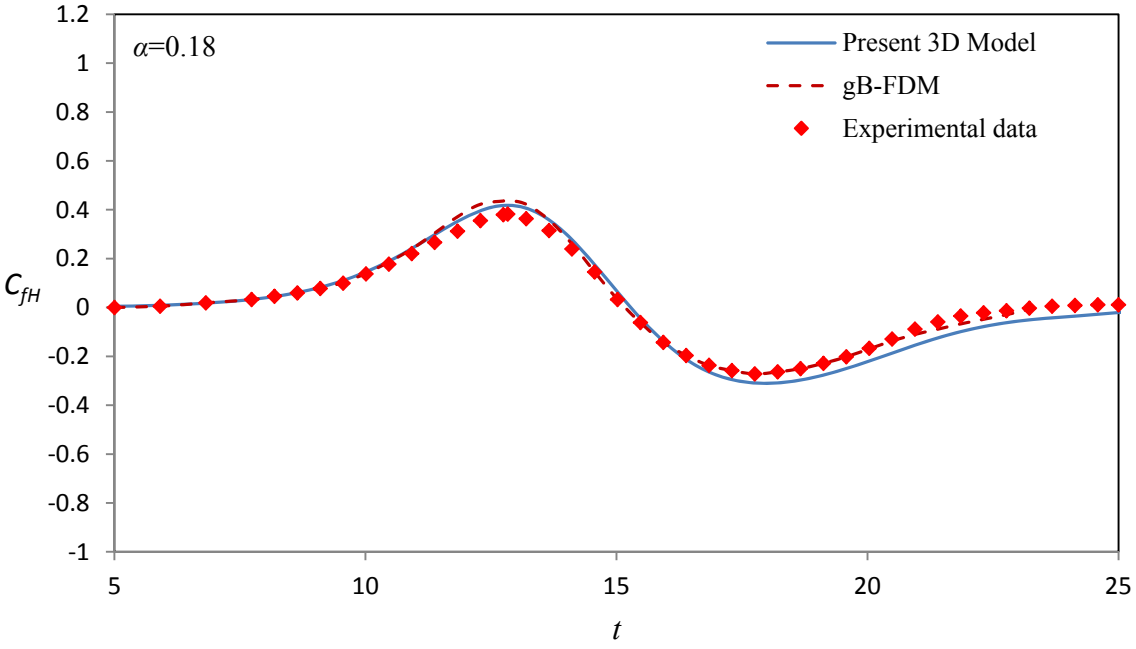

(a)

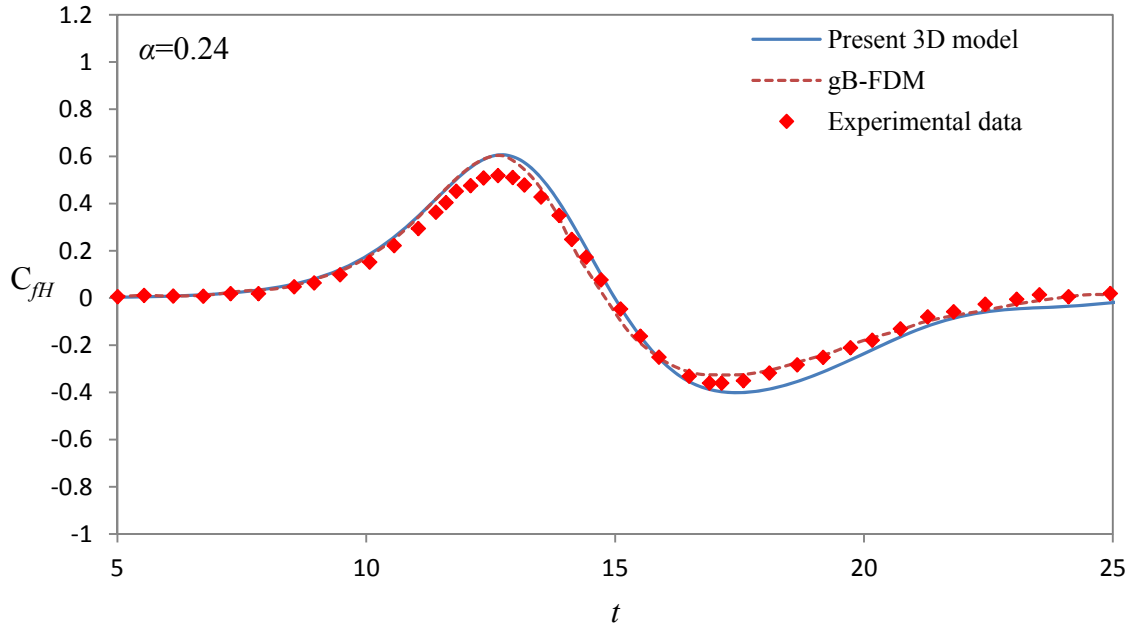

(b)

Figure 4- 9 Comparisons of force coefficient C_{fH} in time sequence, (a) $\alpha = 0.18$, (b) $\alpha = 0.24$, (c) $\alpha = 0.32$, and (d) $\alpha = 0.4$

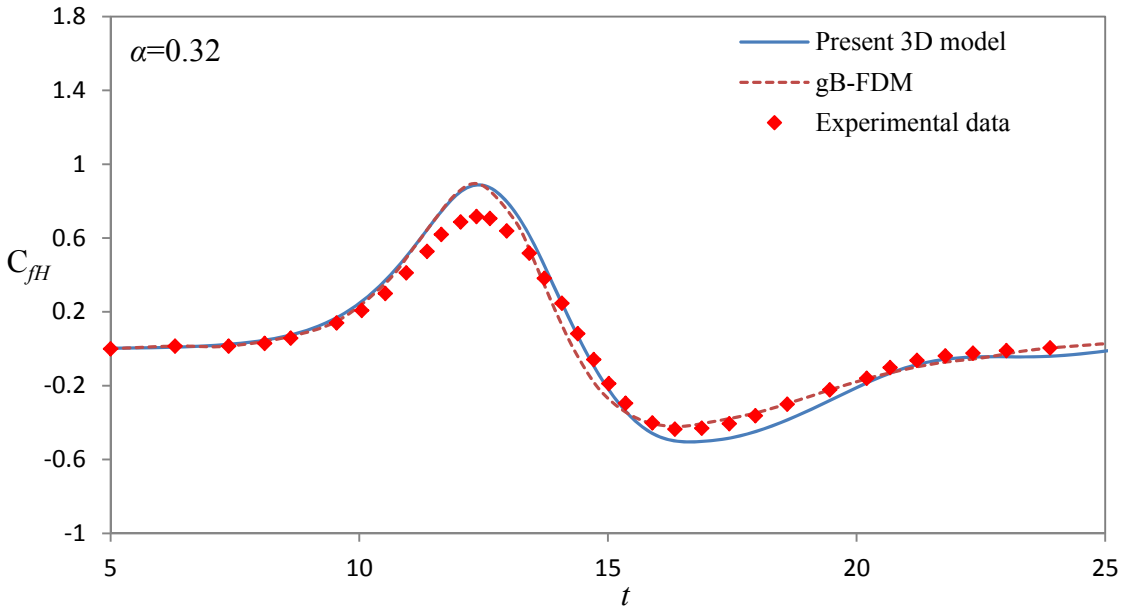

(c)

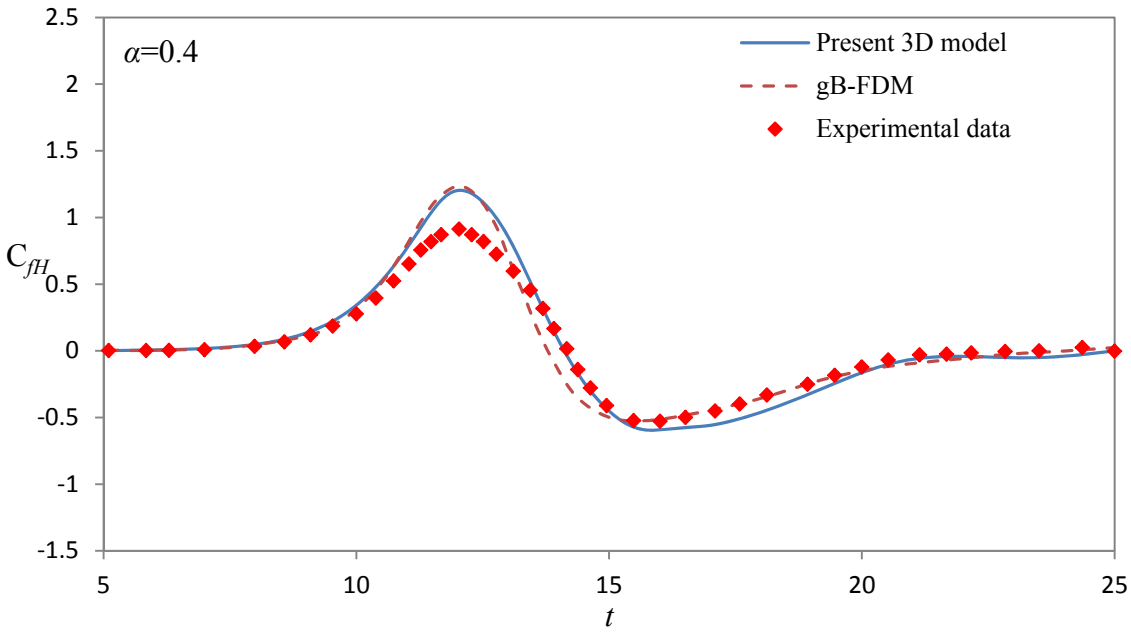

(d)

Figure 4- 9 Comparisons of force coefficient C_{fH} in time sequence, (a) $\alpha = 0.18$, (b) $\alpha = 0.24$, (c) $\alpha = 0.32$, and (d) $\alpha = 0.4$ (continued)

Chapter 5

Solitary Waves Interacting with a Fix Floating Cylinder

In Chapter 4, the present three-dimensional fully nonlinear model is demonstrated to be able to successfully simulate the interaction of a solitary wave with a bottom mounted vertical cylinder. Simulations of waves encountering with Structures having non-uniform boundary condition in z-direction, such as floating structures, where the motion within the region below the structures needs to be calculated separately, can also be carried out by the present model. Thus, this chapter provides the results of the present model simulating a case of a solitary wave interaction with a partially submerged and fixed floating cylinder. For the simulation, all physical variables are dimensionless defined by Equation (2-1) and the schematic diagram is shown in Figure 5- 1. In the figure, the channel has a dimensional constant water depth h_0^* and the dimensionless gap (G) is defined as the space between the bottom of the cylinder and the channel bed. Moreover, two rectangular grid systems and one polar grid system as shown in Figure 3-3 are applied in the simulation. In order to verify the numerical results obtained from the present model, experiments of a solitary wave propagating in a flume and the subsequent interaction with a partially submerged and fixed floating cylinder were performed for comparisons. The setups for the experimental measurement are introduced in the following section.

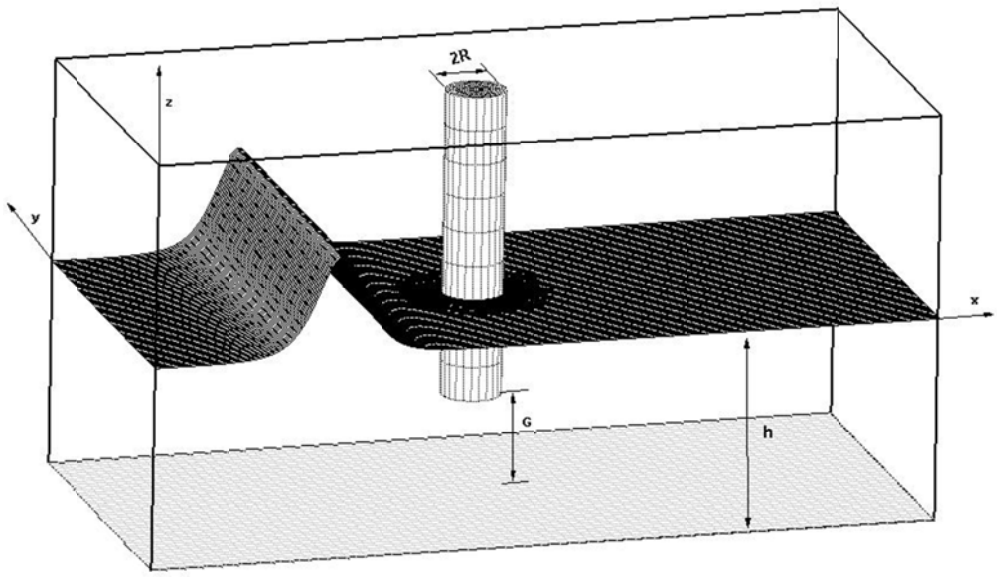

Figure 5- 1 Schematic diagram of initial solitary wave incident upon fixed floating cylinder

5.1 Experimental Measurement

Experimental measurement for a solitary wave passing through a partially immersed and fixed floating cylinder can be used to verify the simulated results from the present three-dimensional fully non-linear model. The experiment was conducted in a glass-walled wave flume having the dimension of length = 762 cm, width = 30.48 cm, and depth = 91.44 cm. A roughly 50cm long expanded downstream section is connected to the wave flume for wave absorption. The experimental setup in the glass-walled flume is shown in Figure 5- 2. A Tolomatic linear actuator drives a piston-type wavemaker to generate a solitary wave propagating in the channel. The amplitude of the solitary wave is controlled by the paddle moving distance input into the control software. Both ends of the flume have energy dissipaters to reduce wave reflection.

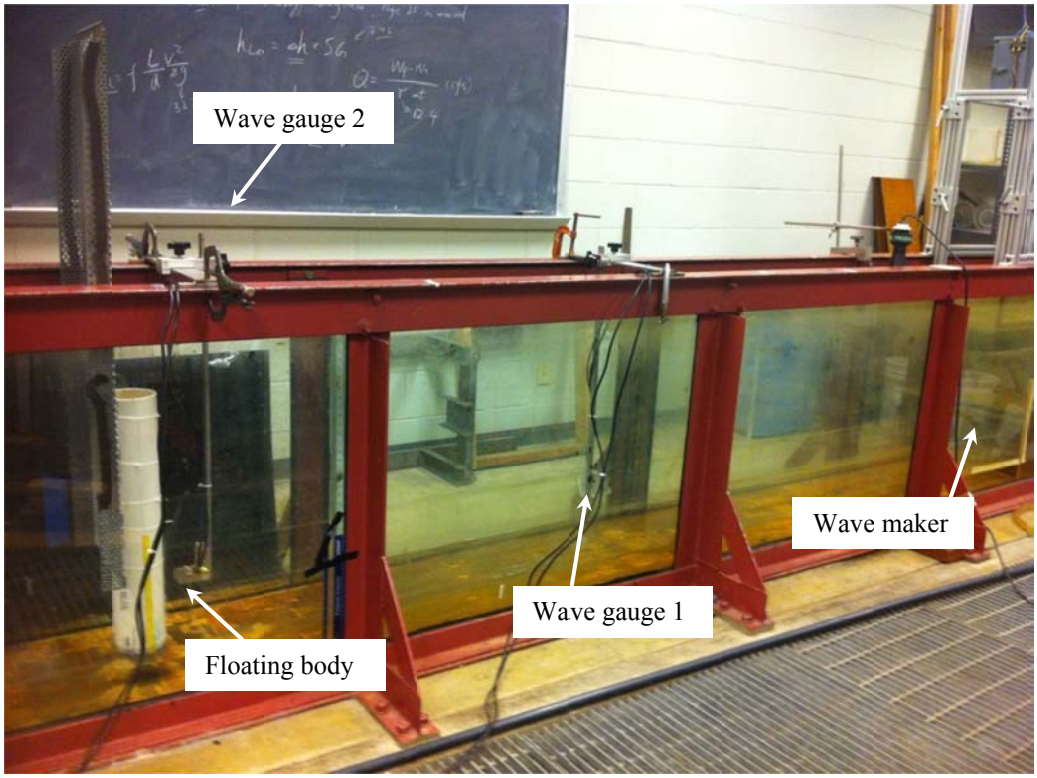

Figure 5- 2 The experimental setup in the glass-walled flume for measuring the wave amplitude in front of the cylinder

Figure 5- 3 illustrates a schematic diagram of the location of the wave gages. Only two resistance type wave gauges are reliable to be used to collect data. Thus, one wave gauge, Gauge 1, was fixed at an upstream location to measure the incident waves. The other wave gauge, Gauge 2, was positioned in the front of the cylinder to measure the changes of the wave elevation at a position close to the cylinder as showed in Figure 5- 3(a). While measuring the variations of the free-surface elevation behind the cylinder, Gauge 2 was moved to the back of the cylinder for the measurements [see Figure 5- 3(b)]. The resistance type wave gauges are constructed by two steal probes with a diameter of 1/16 inches to sense the voltage signals in reference to the free-surface elevations and to

allow the data be recorded in the computer through the LabVIEW data acquisition system. The free-surface elevations were obtained by the linear correlation between the voltage and the free-surface elevation. In order to assure the linear correlation fitting to each gauge, the calibration of the wave gauges between the voltage and the free-surface elevation were performed before the experiments.

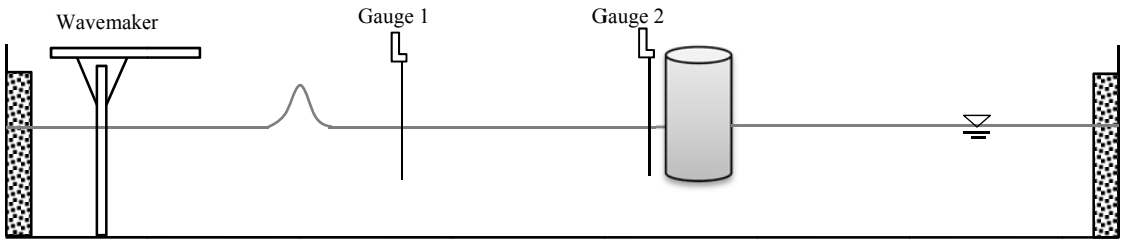

(a)

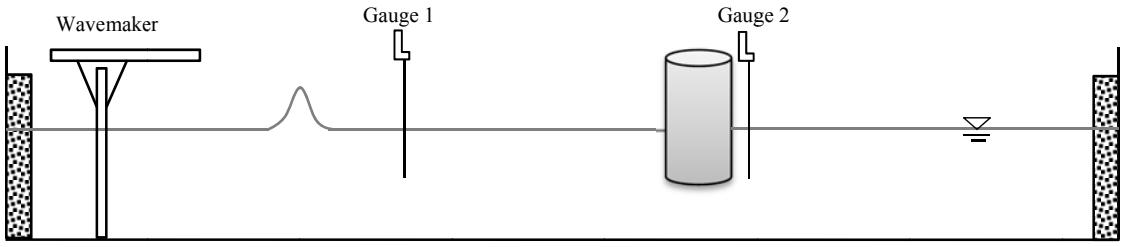

(b)

Figure 5- 3 Schematic diagram of experiment setup: (a) measurement free surface elevation in front of cylinder; (b) measurement free surface elevation in back of cylinder

The undisturbed water depth (h_0^*) set for this experiment was 7.62 cm. The radius of the cylinder, shown in Figure 5- 4, was 5.715 cm ($R = 0.75$) and its center is located at 46.75 water depth far from the wavemaker. The cylinder and the wave gauges set along the centerline of the cylinder. The draft of the cylinder was 3.81 cm, which gives $G = 0.5$ in dimensionless. Since there were only two reliable wave gauges, the experiments with the same wave conditions need to be repeated to measure the free-surface elevations at different locations. Gauge 1 was always set at 30 water depth far downstream from the wavemaker to measure the incident solitary waves. Gauge 2, used to measure the variations of the wave profile around the cylinder, was located at $r/R = 1.88$ in front of or behind the cylinder. The repeat of the incident wave condition for a setting of the wavemaker was checked and the amplitude α of the generated initial solitary wave measured by Gauge 1 was found to be close to 0.31. The experimental measurements based on $\alpha = 0.31$ are used to compare to the solutions obtained from the present three-dimensional fully nonlinear numerical model and the comparisons are presented in the next section.

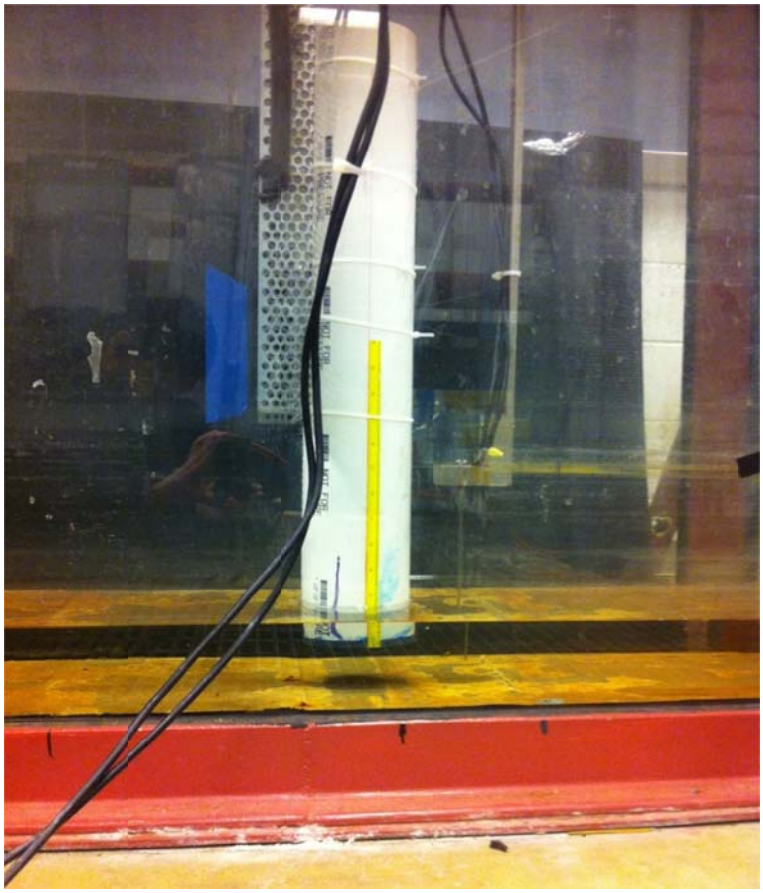

Figure 5- 4 The partially immersed and fixed floating cylinder for experiment

5.2 Comparisons of the Present Model Results with Experimental Measurements and Analysis of the Effect of the Draft

The partially immersed and fixed floating cylinder case is simulated by the present three-dimensional fully nonlinear model and its results are compared with the experimental measurements described in the previous section. The selections of the dimensionless radius of the cylinder, the draft of the cylinder, and the locations of comparison for the present numerical model simulation are based on the setting of the laboratory tests. Again, the dimensionless radius of cylinder is 0.75 and the draft of the

cylinder is $G = 0.5$. The two selected radial locations (r/R) are 1.88 at the $\theta = 0°$ and $180°$ lines respectively. $\theta = 0°$ denotes the direction pointing toward the negative x direction. The amplitude α of the initial solitary wave is set as 0.31 based on the experimental measurements.

Figure 5- 5 illustrates the comparisons of the free-surface elevation that are obtained from the present three-dimensional fully nonlinear wave model and from the experimental measurements at the two identified locations where one is at r/R=1.88 in front of the cylinder [Figure 5- 5 (a)] and the other is with the same distance but at rear side of the cylinder [Figure 5- 5 (b)]. From Figure 5- 5 (a), it is clearly indicated that the wave profile obtained from the present model simulation has a good agreement with the measured data, especially the main including the peak and trough of the free-surface elevation. On the rear part of the cylinder, the present model as shown in Figure 5- 5 (b) can also predict reasonably well the varying free-surface elevations when compared to the experimental measurements. The good agreement between the present numerical solutions and experimental data again suggests that the present model can capture the variation trend of the wave elevations during the interaction process, especially at the locations close to the front and rear surfaces of the cylinder. Therefore, the comparison studies presented above demonstrate that the present three-dimensional fully nonlinear wave model is capable of making a good prediction on the time varying free-surface variations during an encountering process of a solitary wave and a partially immersed and fixed floating cylinder.

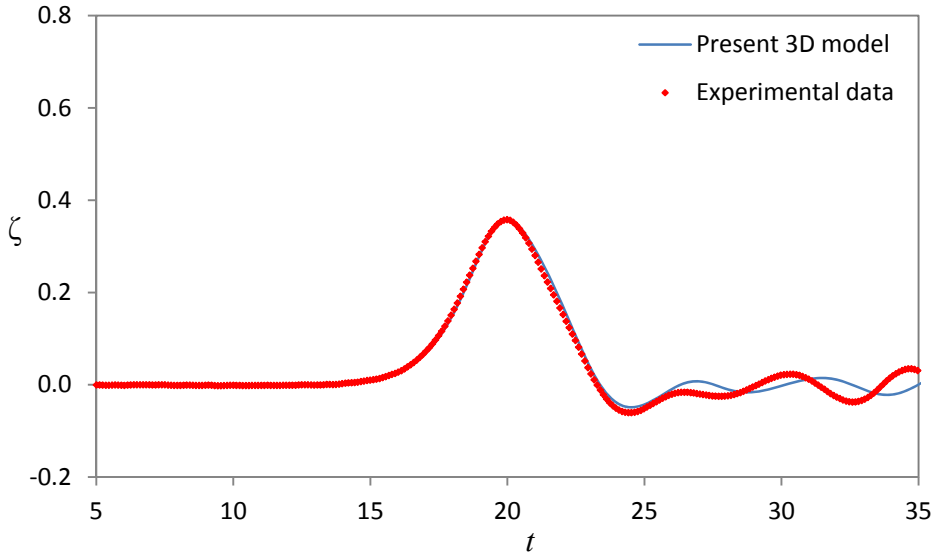

(a)

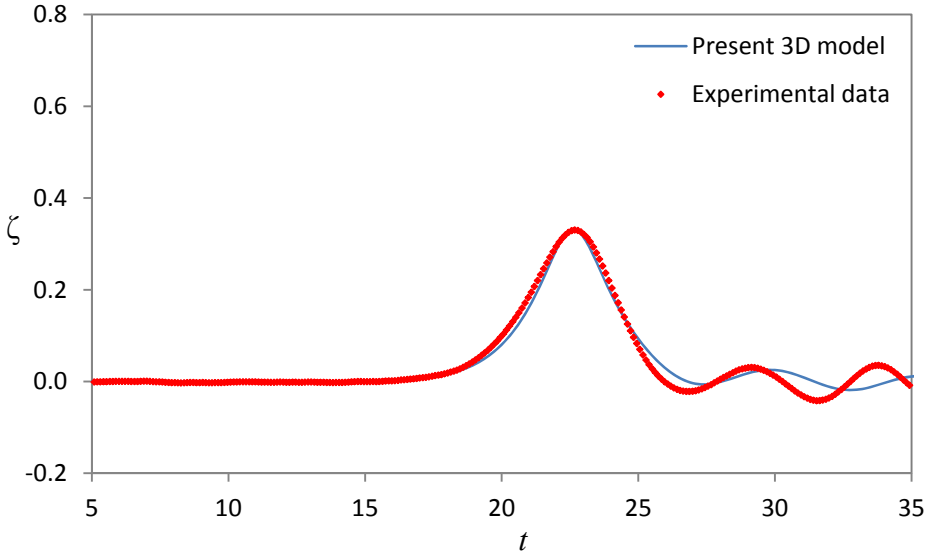

(b)

Figure 5- 5 Comparisons of time variation of free surface elevation obtained from numerical and experimental measurement: (a) in front of the cylinder ($\theta = 0°$) and (b) in back of the cylinder ($\theta = 180°$)

Figure 5- 6 and Figure 5- 7 shows the comparisons of the time variation of the free-surface elevation for three different draft conditions at respectively the locations ($r/R = 1.88$) in front of and at the back of the cylinder with the initial wave amplitude $= 0.31$. From Figure 5- 6, it can be observed that the free-surface elevations especially at the peak location increase as the gap decreases. When the gap decreases, the cylinder has more blockage area in the fluid domain to cause the wave to have a higher run-up. At the rear side of the cylinder [Figure 5- 7], the difference between the free-surface elevations of the different drafts are not significant. The reason of it is that the blockage of the cylinder does not produce obvious effect on waves at the region behind the cylinder, especially when the cylinder radius is small.

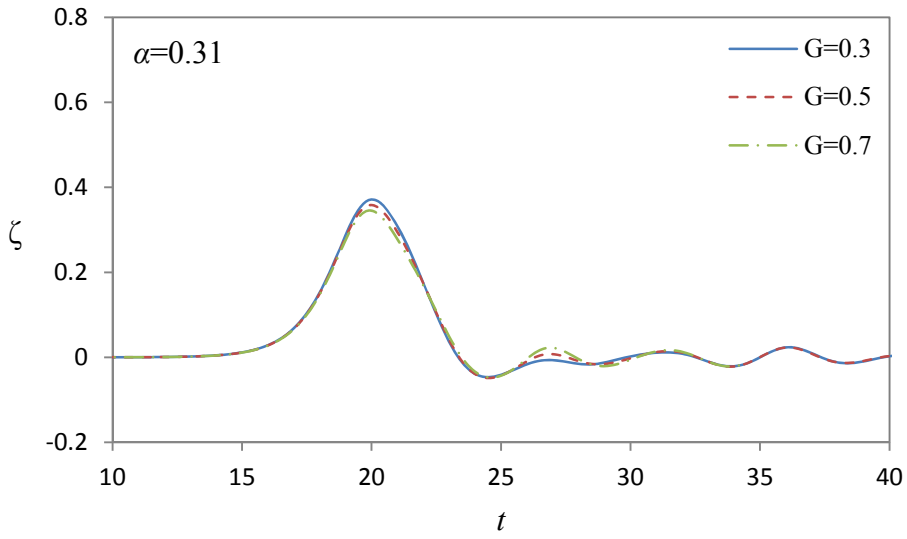

Figure 5- 6 Comparisons of time variation of free surface elevation obtained from the present model with gap G = 0.3, 0.5, and 0.7: in front of the cylinder ($\theta = 0°$)

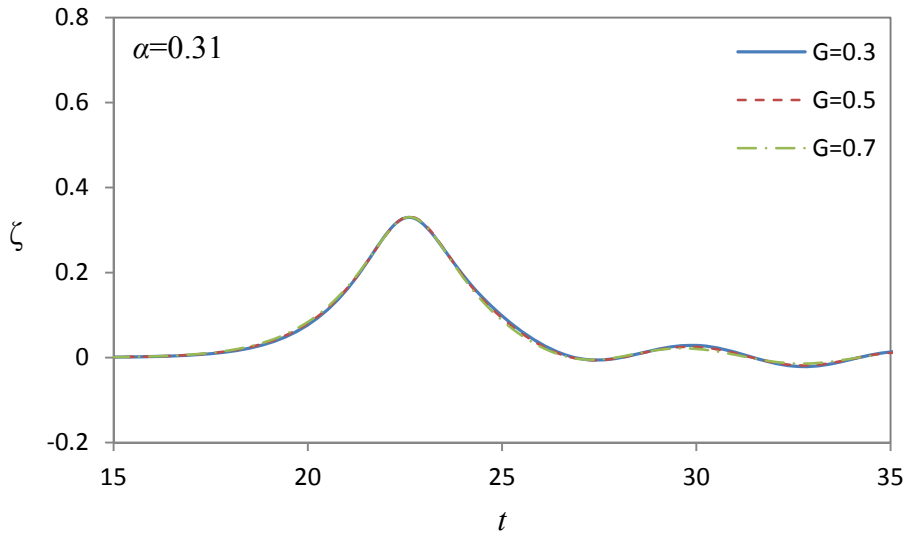

Figure 5- 7 Comparisons of time variation of free surface elevation obtained from the present model with gap G = 0.3, 0.5, and 0.7: at the back of the cylinder ($\theta = 180°$)

5.3 Forces on a Partially Immersed and Fixed Floating Cylinder

Two different hydrodynamic forces, namely the horizontal and vertical forces, acting on a partially immersed and fixed floating cylinder can be calculated by the present three-dimensional fully nonlinear model according to Equation (2- 21) and Equation (2- 22), respectively. In this section, the hydrodynamic forces, induced by the interaction between a solitary wave of $\alpha = 0.31$ and a cylinder with a dimensionless diameter of 1.5 are presented.

In addition to the complete approach by integrating the pressures over a structural surface for force calculation, Morison et al. (1950) introduced an empirical formula to estimate without considering the diffraction effect the time varying wave forces on

structures. The formula as it combines the inertia and drag forces to obtain the total horizontal wave forces acting on a cylindrical structure are expressed as

$$F_H = F_D + F_I \ ,$$

$$= \int_{-d}^{0} \frac{1}{2} C_D \rho A u |u| \, dz + \int_{-d}^{0} C_M \rho V \frac{Du}{Dt} \, dz \ , \qquad (5\text{-}1)$$

where F_I, F_D, C_D, and C_M are the inertia force, drag force, drag coefficient, and inertia coefficient, respectively. In order to calculate the total wave force acting on a cylinder, the proper coefficients, C_D and C_M, need to be chosen. For the given wave and cylinder conditions, the estimated $Kc = 0.82$, $\mathrm{Re} = 1.11 \times 10^4$, and $D/\lambda < 0.2$, where Kc is Keulegan-Carpenter number, Re is Reynolds number, D = diameter, and λ : wave length. According to the summarized C_D and C_M values suggested by Hogben et al (1977), the hydrodynamic force of a solitary wave with $\alpha = 0.31$ acting on the surface of a cylinder with a diameter of 1.5 is in the inertia force dominant zone while using the Morrison equation. In other words, the C_M is equal to two and the C_D can be neglected. Hence, we have

$$F_H = \int_{-d}^{0} \rho \, A \, u \, |u| \, dz \ . \qquad (5\text{-}2)$$

For convenience of force comparisons with the present model, the forces calculated by the Morison equation are also normalized as force coefficient, C_{fH}. Although Morison equation provides empirically based estimations of the force coefficients, it is selected as

commonly used in engineering applications to calculate wave induced horizontal forces for comparisons with the present model solutions.

Figure 5- 8 shows the horizontal force coefficients C_{fH} calculated from the present three-dimensional model and the Morison equation in time sequence. It is noticeable that the time variations of the force coefficients calculated by the present model and the Morison equation are similar. However, as the forces from the Morison equation include the part of linearized inertia forces, a symmetric profile of force coefficients can be noticed in Figure 5- 8. In addition, the nonlinear effect from the present model leads to larger positive force coefficients and smaller negative force coefficients than the results from the Morison equation. The hydrodynamic force coefficients in vertical direction with time variation are shown in Figure 5- 9. It illustrates that the hydrodynamic forces in the vertical direction vary with the propagation of a solitary wave and are all positive. Thus, the shape of the vertical hydrodynamic force basically follows the solitary wave profile.

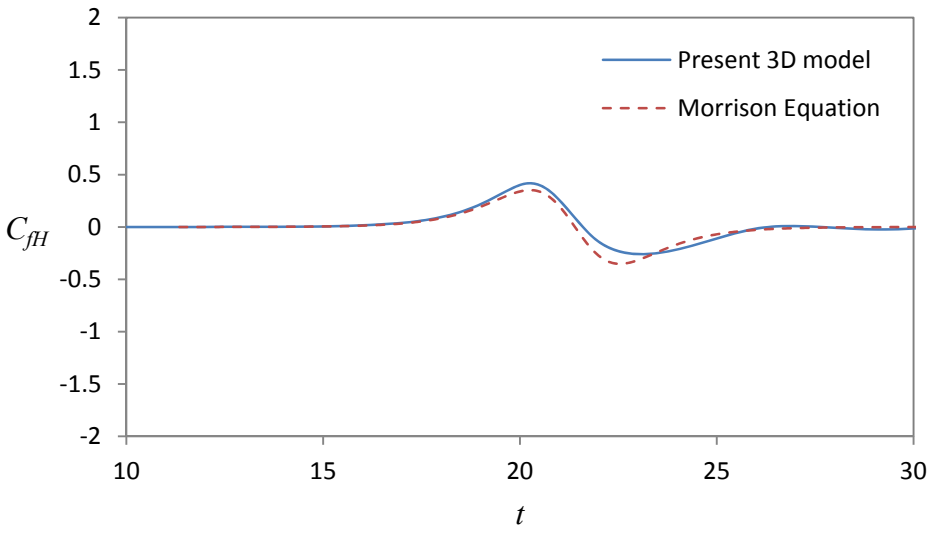

Figure 5- 8 Comparisons of force coefficient, C_{fH}, calculated by the present three-dimensional model and Morison equation in time sequence

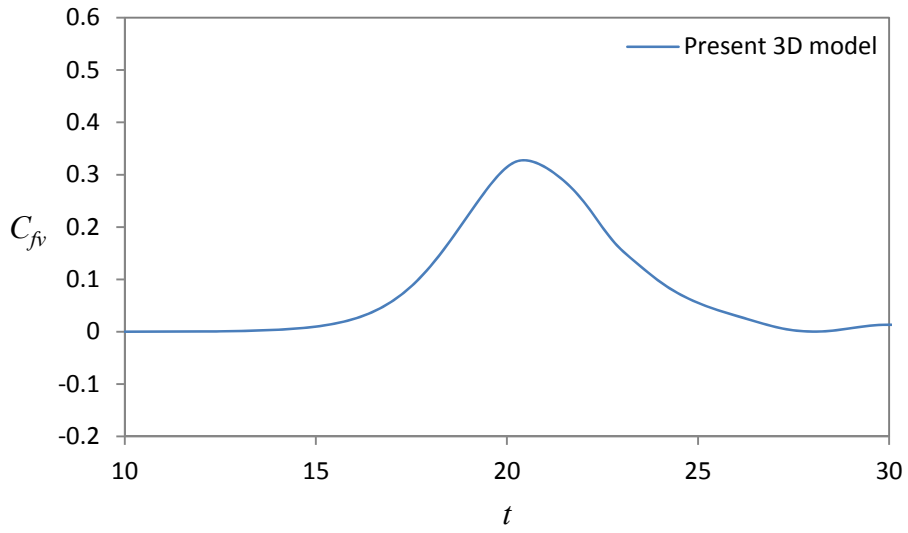

Figure 5- 9 Vertical force coefficient C_{fV}, calculated by the present three-dimensional model in time sequence

5.4 Interaction Process

The comparison study for point measurements and computed free-surface elevations described above concludes that the present three-dimensional fully nonlinear model can successfully and accurately simulate the interaction between a solitary wave and a partially submerged fixed floating cylinder. In order to show the detailed process of the interaction between a solitary wave and a partially submerged fixed floating cylinder, a larger cylinder with a radius of two water depths is considered for model simulation. The cylinder is set at the center of a computational domain, where the ranges along the x and y directions are $0 \leq x \leq 70$, and $0 \leq y \leq 35$. Again, the computational domain is covered with two rectangular grid systems and an overlapped polar grid system. One of the rectangular grid systems with $\Delta x = \Delta y = 0.25$ is used for the outer domain and the other is applied underneath the cylinder where the grid sizes in both x and y directions are set as 0.1. In the z direction, the grid sizes changing with time are derived from Equation (3- 26). The initial solitary wave peak is set at $x_0 = 10$ to allow the solitary wave establishing to a stable wave amplitude before impacting the cylinder.

Figure 5- 10 shows a time sequence of three-dimensional perspective view plots of the free-surface elevation during the interaction process. At $t = 10$, a stable incident solitary wave with amplitude of $\alpha = 0.3$ is shown to propagate towards a fixed floating cylinder with a draft of 0.5 (G=0.5). The solitary wave approaches the front surface of the cylinder at $t = 20.6$ and the free-surface elevation increases to the maximum value. A backscattering wave initiated by the diffraction starts to propagate radially outwards at $t = 25$ while the main solitary wave have just passed the cylinder. It can also be noticed the central part of the free-surface elevation behind the cylinder, due to the blockage of

the existing cylinder, is lower than the other parts of the primary wave. In spite of the difference of the free-surface elevation of the main wave, the whole main wave as a coherent structure still keeps the same propagating speed. The central part of the main wave gradually recovers to nearly its original solitary wave amplitude at $t = 33$. Additional secondary scattered waves propagating outwards and following the leading scattered wave can be observed at $t = 33$ and $= 38$. At $t = 42$, the main wave nearly recovers to its initial solitary wave shape and amplitude, and a group of the scatter waves propagating radially outwards from the cylinder expand over the whole fluid domain around the cylinder. Moreover, the scattering process with much smaller oscillations produced around the cylinder continues. From these figures, the evolution of a solitary wave interacting with a fixed floating cylinder is found to be similar to that of a solitary wave encountering a bottom mounted and surface piercing cylinder, however, with a series of less pronounced scattered waves.

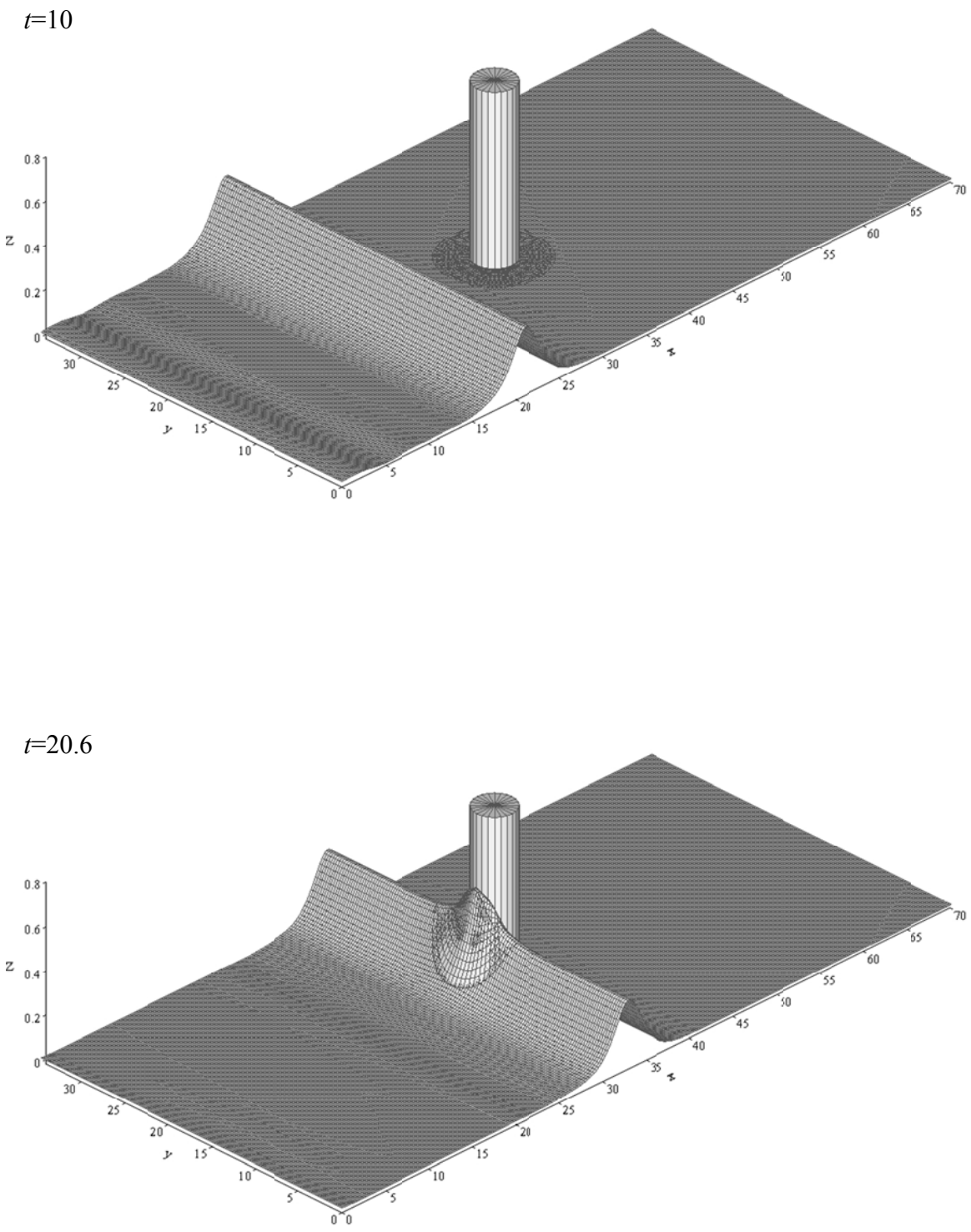

Figure 5- 10 Three-dimensional perspective view plot of free-surface elevation ζ for $\alpha = 0.3$ at selected instants of time (partially submerged cylinder case)

t=25

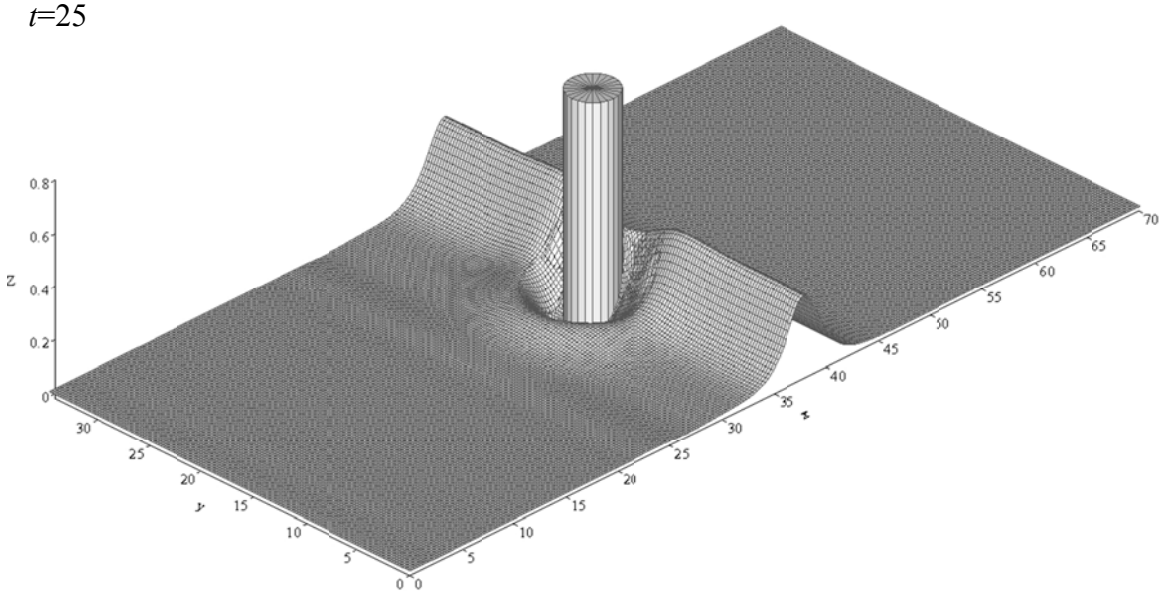

t=33

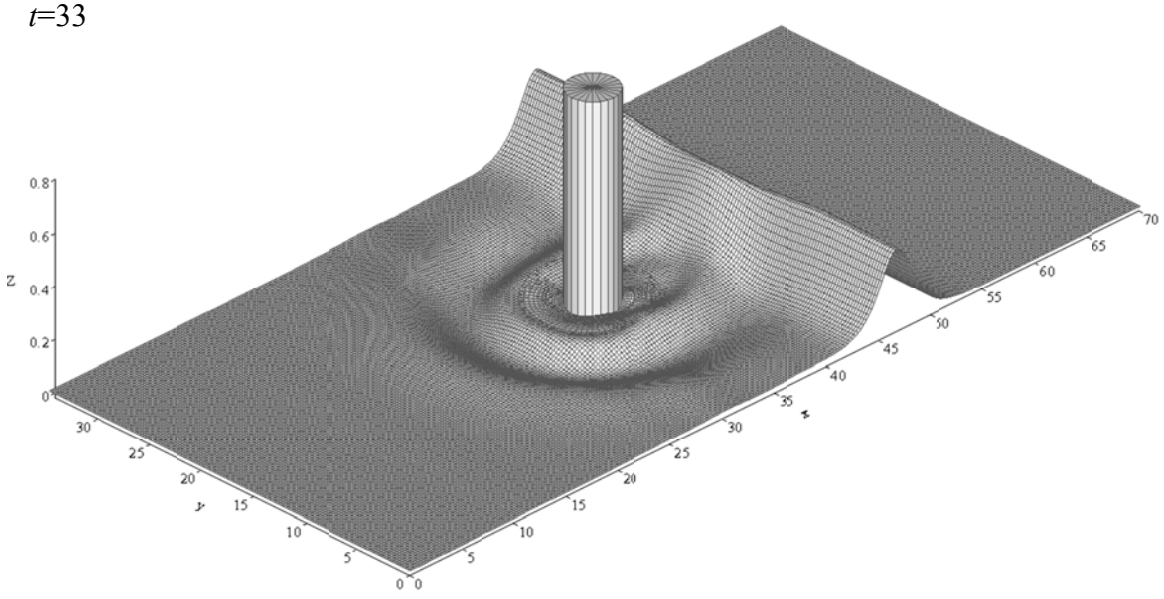

Figure 5- 10 Three-dimensional perspective view plot of free-surface elevation ζ for $\alpha = 0.3$ at selected instants of time (partially submerged cylinder case) (Continued)

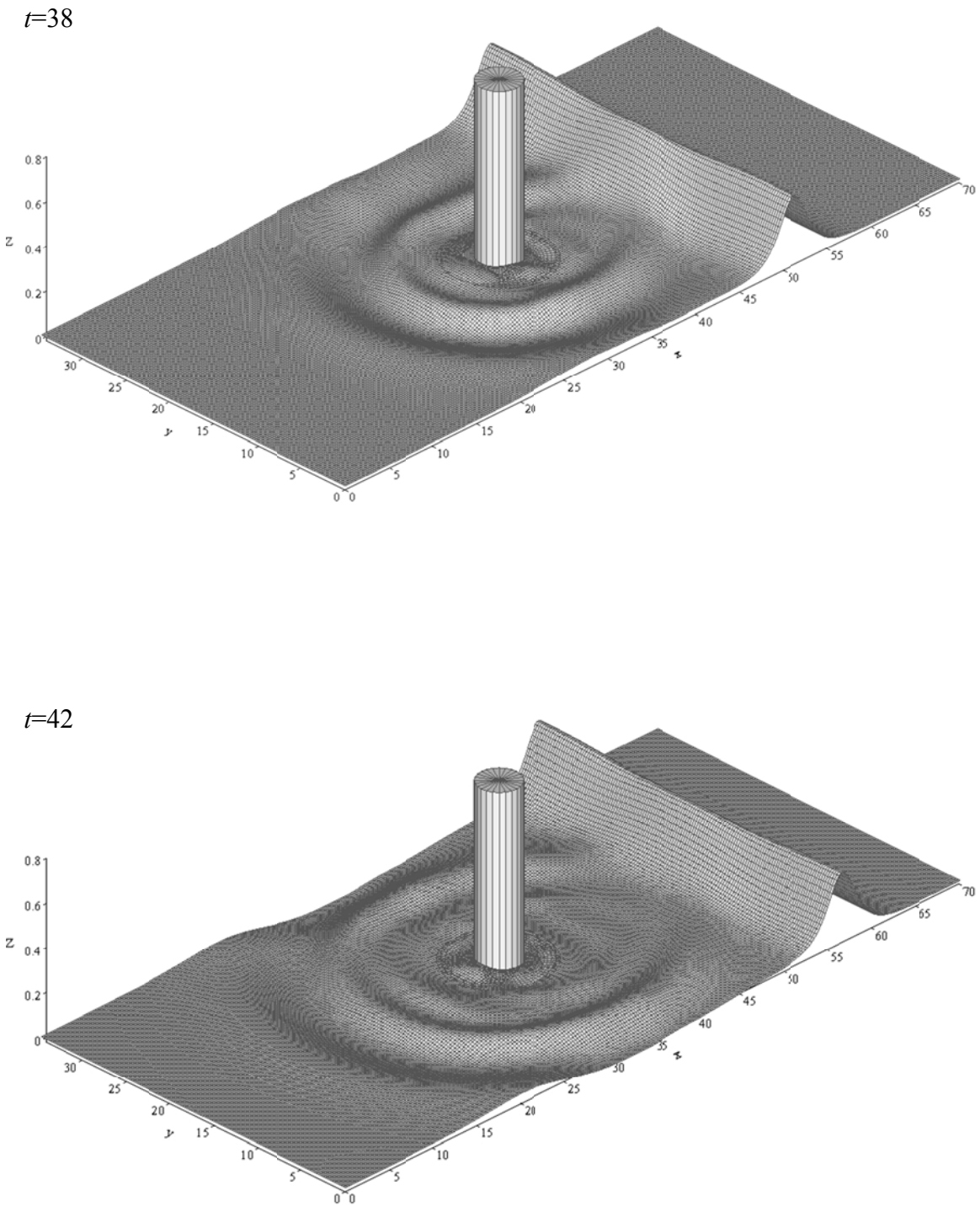

Figure 5- 10 Three-dimensional perspective view plot of free-surface elevation ζ for $\alpha = 0.3$ at selected instants of time (partially submerged cylinder case) (Continued)

In Figure 5- 11, a contour plot shows the pattern of the scattered waves after the solitary wave propagates pass the cylinder at $t = 42$. Solid lines represent positive values of the free-surface elevation, and negative values of the free-surface elevation are represented by dash lines. The circular scattered waves which are concentric to the cylinder cover most fluid fields. The scattered waves with smaller amplitude also can be observed nearby the cylinder. In addition, the main wave has nearly recovered back to the initial solitary wave shape.

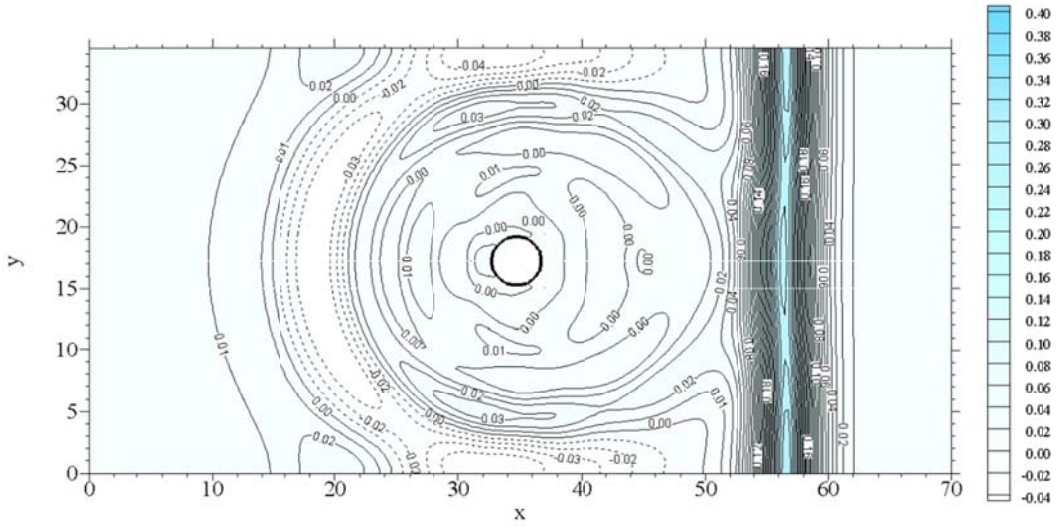

Figure 5- 11 Contour plot of the free-surface elevation for amplitude of the solitary wave $\alpha = 0.4$ and cylinder diameter $R = 2.0$ at $t = 42$

Chapter 6

Summary and Conclusions

This dissertation presents the development and numerical applications of a three-dimensional fully nonlinear wave model with the use of a transient curvilinear coordinate transformation technique to study the different scenarios of nonlinear wave propagation and their interactions with cylindrical structures. The present three-dimensional model improves the limitation of the vertical averaged two-dimensional models, such as the Boussinesq model, which is unable to solve the problems related to the boundary variations in the vertical direction. Furthermore, the present model includes a set of three-dimensional transient curvilinear coordinate transformation of the governing equations and the boundary conditions derived to fit the irregular boundaries in the physical domain. For the modeling cases of the interaction between nonlinear waves and structures, the present model applies multigrid systems to construct the computational domains. A mixed implicit and explicit finite difference scheme is adopted for solving the three-dimensional governing equations and boundary conditions.

Simulating a solitary wave propagating in a straight rectangular channel is performed as sensitivity tests to decide the grid sizes and time step used for the present modeling studies. The results of sensitivity tests demonstrate the present model under the selected parameter setting is able to simulate stably the propagation of a solitary wave in a fluid domain. After proving the stability of the present model, it is applied to simulate a solitary wave propagating in a 180° curved channel to demonstrate its capability of

modeling waves propagating in an arbitrary shape channel. From the results of the simulation, it is noticeable that the wave peak changes to a nonuniform distribution across the channel and the free-surface elevation increases near the outer wall due to the centrifugal effect while a solitary wave propagates into the curved region of the channel. In the curved part of the channel, the main wave reflects back and forth between the inner and outer walls during the process of a solitary wave propagating towards the downstream of the channel. The waves reaching the downstream of the channel tends to eventually recover as a main solitary wave followed with a series of oscillating tails. From the comparisons of the time variations of the free-surface elevations at the selected locations, the predicted wave patterns in the curved channel obtained from the present model have good agreement with those calculated from the generalized Boussinesq two-equation model. Thus, the present three-dimensional fully nonlinear wave model can provide stable and accurate predictions on nonlinear waves propagation in a channel with irregular boundary.

The present three-dimensional fully nonlinear wave model is extended to solve the interaction of waves and structures problems. The first simulation scenario is a solitary wave encountering with a bottom mounted and surface piercing vertical cylinder. During the interaction process, the solitary wave gradually piles up to a maximum value of the free-surface elevation while the main wave approaches the cylinder. After the main wave passes the cylinder, the center part of the free-surface elevation behind the cylinder is lower than other parts of the primary wave because of the blockage of the existing cylinder. When the solitary wave propagates beyond the cylinder over 20 water depths, the main wave nearly recovers back to a whole solitary wave with the original wave

amplitude. Moreover, it is clear that a group of scatter waves propagates out from the cylinder and expands over the upstream and downstream regions around the cylinder. The predicted free-surface elevations with time variation at the selected locations obtained by the present model and generalized Boussinesq model have reasonable agreement with the experimental measurements except at the positions nearly on the cylinder surface, where both models overestimate the maximum wave amplitudes. Moreover, the hydrodynamic force predictions obtained from either the present model or generalized Boussinesq model match closely with the measured forces for the cases with small incident wave amplitude. When the amplitude of the incident wave increases, the predicted forces are larger than the measured values. These overestimated predications may be caused by the measurement errors, and potential viscous and flow separation effects.

The present three-dimensional fully nonlinear wave model is further applied to simulate the interaction of a solitary wave with a partially submerged and fixed floating cylinder. To verify the accuracy of the present model simulations, the experiments of a solitary wave propagating past a partially submerged and fixed floating cylinder were conducted in a wave tank. The comparisons of model results with the experimental measurements indicate the present model is able to make a fairly good prediction on the time varying free-surface elevations, especially at a position in front of the cylinder, during the encountering process of a solitary wave and a partially immersed and fixed floating cylinder. The wave evolution patterns for a solitary wave interacting with a fixed floating cylinder are similar to those of the solitary wave encountering a bottom mounted and surface piercing cylinder but with less pronounced scattered wave field. The free-

surface elevation of the main wave piles up in front of the cylinder. Then, the center part of the main wave has lower amplitude due to the blockage of the cylinder and recovers gradually to its initial solitary wave shape and amplitude as the main wave propagates away from the cylinder. In addition, the scattered waves propagate radially outwards from the cylinder and expand over the whole fluid domain around the cylinder. It is again demonstrated the successful application of the present three-dimensional fully nonlinear wave model in simulating the interaction of a nonlinear wave and a fixed floating structure and making good predictions of the variations of the free-surface elevation during the process of wave-structure interaction.

The present three-dimensional fully nonlinear wave model can solve the problems with boundary variation in vertical direction. However, the governing equation is based on the assumption of incompressible and inviscid fluid and the motion irrotational. Thus, the present model is limited to the study of wave simulation in a domain with viscous fluid. In addition, for simulating cases with open sea, due to the rigid boundary condition applied on the side wall in the present model, the wall boundary conditions need to be extended to include the lateral open boundary conditions.

For future research, the present three-dimensional fully nonlinear wave model can be expanded for wider applications. In this study, the present model only simulates the interaction between a solitary wave and a fixed cylinder. More complicated structures or different nonlinear waves, such as an array of floating cylinders, cnoidal waves, or even steeper Stokes waves, may be considered for future simulation studies using the present model. For the model development point of view, the present model can be further extended by combining with the solver of equation of motion to simulate the interaction

between nonlinear waves and movable floating structures. Moreover, in the future, the laboratory experiments of a floating cylinder subject to the wave action are recommended to be performed in a large wave tank to collect more detailed wave elevation data in areas surrounding a cylinder to further the confirmation of the performance of the developed wave model.

References

Agnon, Y., Madsen, P.A., Schaffer, H.A., 1999, "A New Approach to High-order Boussinesq Models," *J. Fluid Mech*., 399, pp. 319-333.

Ai, C., and Jin, S., 2010, "Non-Hydrostatic Finite Volume Model For Non-Linear Waves Interacting With Structures," *Computers & Fluids*, 39, pp. 2090-2100

Ambrosi, D., and Quartapelle, L., 1998, "A Taylor-Galerkin Method for Simulating Nonlinear Dispersive Water Waves," *J. Comput. Phys.*, 146, pp. 546-569.

Antunes do Carmo, J.S., Seabra Santos, F.J. and Barthelemy, E., 1993, "Surface Waves Propagation in Shallow Water: A Finite Element Model," *Int. J. Numer. Methods Fluids*, 16, pp. 447-459.

Asmar, E.W., and Nwogu, O., 2007, "Finite Volume Solution of Boussinesq-Type Equations on an Unstructured Grid," Proc. 30th Int. Conf. Coastal Eng., pp. 73-85.

Bai, W. and Eatock Taylor, R., 2009, "Fully Nonlinear Simulation of Wave Interaction with Fixed and Floating Flared Structures," *Ocean Engineering*, 36, pp. 223-236

Basmat, A., Ziegler, F., 1998, "Interaction of a Plane Solitary Wave with a Rigid Vertical Cylinder," Zeitschrift fuer Angewandte Mathematik und Mechanik, ZAMM, *Applied Mathematics and Mechanics*, 78(8), 535-543.

Boo SY., 2002, "Linear And Nonlinear Irregular Waves and Forces in a Numerical Wave Tank," *Ocean Engineering*; 29:475–493.

Choi, D.Y., and Yuan, H., 2012, "A Horizontally Curvilinear Non-Hydrostatic Model for Simulating Nonlinear Wave Motion in Curved Boundaries," *Int. J. Numer. Meth. Fluids*, 69, PP. 1923-1938.

Choi, D.Y., Wu, C.H., Young, C.C., 2011, "An Efficient Curvilinear Non-Hydrostatic Model for Simulating Surface Water Waves," *Int. J. Numer. Methods Fluids*, 66, pp. 1093–1115

Chwang, A. T., and Wu, J., 1994, "Wave Scattering by Submerged Porous Disk," *J. Engrg. Mech., ASCE*, 120(12), pp. 2575-2587

Drimer, N., Agnon, Y., Stiassnie, M., 1992, "A Simplified Analytical Model for A Floating Breakwater in Water of Finite Depth," *Applied Ocean Research*, 14, pp. 33-41

Eatock Taylor, R., Wu, G.X., Bai, W., Hu, Z.Z., 2008, "Numerical Wave Tanks Based on Finite Element and Boundary Element Modeling," *J. offshore Mech. Arct. Eng*., 130, pp. 031001.1-0.1001.8

Fang, K.Z., Zou, Z., Liu, Z.,Yin J., 2012, "Boussinesq Modeling of Nearshore Waves Under Body Fitted Coordinate," *J. Hydrodynamics*, 24(2), pp. 235-243.

Garrett, C. J. R., 1971, "Wave Forces on a Circular Dock." *J. Fluid.Mech*., 46, 129- 139.

Gobbi, M.F., Kirby, J.T., and Wei, G., 2000, "A Fully Nonlinear Boussinesq Model for Surface Waves, Part 2. Extension to $O(kh)^4$," *J. Fluid Mech.*, 405, pp. 181-210.

Hogben, N., Miller, B. L., Searle, J. W., Ward, G., 1977, "Estimation of Fluid Loading On Offshore Structures," Proc. Instn. Civ. Engrs., Part2, 63, pp. 515-562.

Isaacson, M. de St Q., 1982, "Nonlinear-Wave Effects on Fixed and Floating Bodies." *J. Fluid Mech.*, 120, 267-281.

Isaacson, M. de St Q., 1983, "Solitary Wave Diffraction around Large Cylinders." *J. Wtrwy., Port, Coastal, and Ocean. Engrg., ASCE*, 109(1), 121-127.

Isaacson, M., and Cheung, K. F., 1990, "Time-Domain Solution for Second-Order Wave Diffraction," *J. Wtrwy., Port, Coastal, and Ocean. Engrg., ASCE*, 116(2), pp. 191- 210.

Isaacson, M., and Cheung, K. F., 1991, "Second-Order Wave Diffraction around Two-Dimensional Bodies by Time-Domain Method," *Appl. Oc. Res.*, 13(4), PP. 175-186.

Isaacson, M., and Cheung, K. F., 1992, "Time-Domain Second-Order Wave Diffraction in Three Dimensions," *J. Wtrwy., Port, Coastal, and Ocean. Engrg., ASCE*, 118, pp. 496- 516.

Kagemoto, H., and Yue, D.K.P., 1986, "Interactions among Multiple Three-Dimensional Bodies in Water Waves: An Exact Algebraic Method," *J. Fluid Mech*, *1*66, pp. 189-209.

Kang, A., Lin, P., Lee, Y. J., Zhu,B., 2015, "Numerical Simulation of Wave Interaction with Vertical Circular Cylinders of Different Submergences Using Immersed Boundary Method," *Computer and Fluids*, 106, pp. 41-53.

Katopodes, N.D., and Wu, C.-T., 1987, "Computation of Finite-amplitude Dispersive Waves," *J. Wtrwy., Port, Coastal, and Ocean. Engrg., ASCE,* 113(4), pp. 327-346.

Kawahara, M., and Cheng, J.Y., 1994, "Finite Element Method for Boussinesq Wave Analysis," *Int. J. Comput. Fluid Dyn.*, 2, pp. 1-17.

Kim, J.W., Kyoung, J.H., Ertekin, R.C., Bai, K.J., 2006, "Finite-Element Computation of Wave-Structure Interaction between Steep Stokes Waves and Vertical Cylinders," *J. Wtrwy., Port, Coastal, and Ocean. Engrg., ASCE,* 132, pp. 337-347.

Kim, M.H., 1993, “Interaction of Waves with N-Vertical Circular-Cylinders,” *J. Wtrwy., Port, Coastal, and Ocean. Engrg., ASCE,* 119(6), pp. 671-689.

Kim, M.H., Celebi, M.S., Kim, D.J., 1998, “Fully Nonlinear Interactions of Waves with A Three-Dimensional Body in Uniform Currents,” *Applied Ocean Research*, 20, pp. 309-321.

Kirby, J.T., Dalrymple, R.A., Kaku, H., 1994, “Parabolic Approximations for Water Waves in Conformal Coordinate Systems,” Costal Engineering, 23, PP. 185-213.

Lin, P., 2006, "A Multiple-layer σ-coordinate Model for Simulation of Wave-structure Interaction," *Computers & Fluids*, 35, pp. 147-167.

Liu, Y., Xue, M., Yue, D.K.P., 2001, “Computations of Fully Nonlinear Three-Dimensional Wave-Wave and Wave-Body Inwteractons, Part 2. Nonlinear Waves and Forces On A Body,” *J. Fluid Mech*., 438, pp. 41-66

Lu, X., 2011, “Hydrodynamic Interactions of Nonlinear Shallow Water Waves with a Fixed Floating Structure,” Ph.D Dissertation, University of Houston, Houston, Texas.

Lu, X., Wang, K.H., 2015, “Modeling a Solitary Wave Interaction with a Fixed Floating Body Using an Integrated Analytical-Numerical Approach,” *Ocean Engineering*, 109, pp. 691-704.

Löhner, R., Morgan, K., and Zienkiewicz, O.C., 1984, “The Solution of Non-Linear Hyperbolic Equation Systems by the Finite Element Method,” *Int. J. Numer. Meth.in Fluids*., 4, PP. 1043-1063.

Ma, Q.W., Wu, G.X., Eatock Taylor, R., 2001, “Finite Element Simulation of Fully Non-Linear Interaction between Vertical Cylinders and Steep Waves — Part 1:

Methodology and Numerical Procedure," Int. *J. Numer. Methods Fluids*, 36, pp. 265–285.

Ma, Q.W., Wu, G.X., Eatock Taylor, R., 2001, "Finite Element Simulation of Fully Non-Linear Interaction between Vertical Cylinders and Steep Waves — Part 2: Numerical Results and Validation," *Int. J. Numer. Methods Fluids*, 36, pp. 287–308.

MacCamy, R. C., Fuchs, R. A., 1954, "Wave Forces on Piles: A Diffraction Theory," Technical Memorandum, No. 69, Beach Erosion Board.

Madsen, P.A., Bingham, H.B., Liu, H., 2002, "A New Boussinesq Method for Fully Nonlinear Waves from Shallow to Deep Water," *J. Fluid Mech*., 462, pp. 1-30.

Mavrakos, S.A., 1985, "Wave Loads on a Stationary Floating Bottomless Cylindrical Body with Finite Wall Thickness," Applied Ocean Research, 7, pp. 213-224.

Miles, J. W., and Gilbert, J. F., 1968, "Scattering of Gravity Waves by a Circular Dock," *J. Fluid Mech.*, 34, pp. 783-793.

Molin, B., 1979, "Second-Order Diffraction Loads Upon Three-Dimensional Bodies," *Appl. Ocean Res.*, 1(4), pp. 197-202.

Morison, J. R., O'Brien, M. P., Johnson, J. W., and Schaaf, S. A., 1950, "The Force Exerted By Surface Waves on Piles," Petrol. Trans., AIME, 189, pp. 149-154.

Nachbin, A., and Da Silva Simões, V., 2012, "Solitary Waves in Open Channels with Abrupt Turns and Branching Points," *J. Nonlinear Math. Phys.*, 19, PP. 116-136.

Nwogu, O., 1993, "Alternative Form of Boussinesq Equations for Near-shore Wave Propagation," *J. Wtrwy., Port, Coastal, and Ocean. Engrg., ASCE,* 119(6), pp. 618-638.

Orlanski, I., 1976, "A Simple Boundary Condition for Unbounded Hyperbolic Flows," *J. Comput. Phys.*, 21, pp. 251-269.

Park, J.C., Kim, M.H., Miyata, H., 2001, "Three-Dimensional Numerical Wave Tank Simulations on Fully Nonlinear Wave-Current-Body Interactions." J. Mar. Sci. Technol., 6:70-82.

Peregrine, D.H., 1967, "Long Waves on a Beach," *J. Fluid Mech*., 27, pp. 815-882.

Rostafinski, W., 1972, "On Propagation of Long Waves in Curved Ducts," *J. Acoust.Soc. Am.*, 52, pp.1411-1420.

Sabuncu, T. and Gören, Ö., 1985, "Second-Order Vertical and Horizontal Wave Forces on a Circular Dock," Ocean Engng., 12, pp. 341-361

Shi, A, Teng, M.H., Wu, T.Y., 1998, "Propagation of Solitary Waves through Significantly Curved Shallow Water Channels," *J. Fluid Mech.*, 362, pp. 157-176.

Shi, A., and Teng, M.H., 1996, "Propagation Of Solitary Wave in Channels of Complex Configurations," In Proc. 2nd Intl Conf. on Hydrodynamics, Hong Kong, PP. 349-354

Shi, A., Teng, M.H., Sou, I.M., 2005, "Propagation of Long Water Waves through Branching Channels," *J. of Engineering Mechanics*, 131, pp. 859-871.

Shi, F., Dalrymple, R.A., Kirby, J.T., Chen, Q., Kennedy, A., 2001, "A Fully Nonlinear Boussinesq Model in Generalized Curvilinear Coordinates," *Coastal Engineering*, 42, PP. 337-358.

Siddorn, P., Eatock Taylor, R., 2008, "Diffraction and Independent Radiation by an Arry of Floating Cylinders," *Ocean Engineering*, 35, pp.1289-1303.

Sun, J.L., Wang, C.Z., Wu, G.X., Khoo, B.C., 2015, "Fully Nonlinear Simulations of Interactions between Solitary Waves and Structures Base On the Finite Element Method," *Ocean Engineering*, 108, PP. 202-215.

Thompson, J.F., Thame, F.C., and Mastin, C.W., 1974, "Automatic Numerical Generation of Body-Fitted Curvilinear Coordinate System for Fields Containing Any Number of Arbitrary Two-Dimensional Bodies," *J. computational Phys.*, 15, pp. 299-319

Thompson, J.F., Thame, F.C., and Mastin, C.W., 1977, "TOMCAT- A Code for Numerical Generation of Boundary-Fitted Curvilinear Coordinate System on Fields Containing Any Number of Arbitrary Two-Dimensional Bodies," *J. computational Phys*., 24, pp. 374-302

Wang, C.Z., Wu, G.X., Drak, K.R., 2007, "Interactions between Nonlinear Water Waves and Non-Wall-Sided 3D Structures." *Ocean Engineering*, 34, pp. 1182-1196.

Wang, K.H., 1993, "Diffraction of Solitary Waves By Breakwaters," *J. Wtrwy., Port, Coastal, and Ocean. Engrg., ASCE,* 119(1), pp. 49-69.

Wang, K.H., 1994, "Characterization of Circulation and Salinity Change In Galveston Bay," *J. of Engineering Mechanics*, 120(3), pp. 557-579

Wang, K.H., and Jiang, L., 1994, "Solitary Wave Interactions with an Array of Two Vertical Cylinders," *Applied Ocean Research*, 15(6), 337-350.

Wang, K.H., and Ren, X., 1999, "Interactions of Cnoidal Waves with Cylinder Arrays," *Ocean Engineering*, 26, pp. 1-20.

Wang, K.H., Wu, T.Y., and Yates, G.T., 1992, "Three Dimensional Scattering of Solitary Waves by Vertical Cylinder*," J. Wtrwy., Port, Coastal, and Ocean. Engrg., ASCE,* 118(5), 551-566.

Wei, G., Kirby, J.T., 1995, "A Time-dependent Numerical Code for the Extended Boussinesq Equations," *J. Wtrwy., Port, Coastal, and Ocean. Engrg., ASCE,* 121(5), pp. 251-161.

Williams, A.N., Li, W., Wang, K.H., 2000, "Water Wave Interaction with a Floating Porous Cylinder," *Ocean Engineering*, 27, pp. 1-28.

Woo, S.-B., and Liu, P. L.-F., 2004, "Finite-Element Model for Modified Boussinesq Equations. I: Model Development," *J. Wtrwy., Port, Coastal, and Ocean. Engrg., ASCE,* 130(1), pp. 1-16.

Wood, A., and Wang, K.H., 2015, "Modeling Dam-Break Flows in Channels with 90 Degree Bend Using an Alternating-Direction Implicit Based Curvilinear Hydrodynamic Solver," *Computer & Fluids*, 114, pp.254-264.

Wu, C., Watanabe, E., Utsunomiya, T., 1995, "An Eigenfunction Expansion-Matching Method for Analyzing the Wave-Induced Responses of an Elastic Floating Plate," *Applied Ocean Research*, 17, pp. 301-310.

Wu, D.M., and Wu, T.Y., 1982,"Three-Dimensional Nonlinear Long Waves Due to Moving Surface Pressure," Proc. 14th Symp. On Naval Hydrodynamics, National Academy Press, Washington, D.C., pp. 103-125.

Wu, T. Y. 1979, "On Tsunami Propagation—Evaluation of Existing Models," Tsunamis— Proc. of the Nat. Science Foundation Workshop, L. S. Hwang and Y. K. Lee, eds., Tetra Tech. Inc., Pasadena, Calif., 110-149.

Wu, T.Y., 1981, "Long Waves in Ocean and Coastal Waters," *J. Engrg. Mech. Div., ASCE*, 107, pp. 501-522.

Xue, M., Xü, H., Liu, Y., Yue, D.K.P., 2001, "Computations of Fully Nonlinear Three-Dimensional Wave-Wave and Wave-Body Interactons, Part 1. Dynamics of Steep Three-Dimensional Waves," *J. Fluid Mech*., 438, pp. 11-39.

Yang, C., Ertekin, R.C., 1992, "Numerical Simulation of Nonlinear Wave Diffraction by a Vertical Cylinder," *Journal of Offshore Mechanics and Arctic Engineering*, 114(1), pp. 36-44.

Yates, G.T., and Wang, K.H., 1994, "Solitary Wave Scattering by a Vertical Cylinder: Experimental Study," *Proceedings of the Fourth (1994) International Offshore and Polar Engineering Conference, Osaka, Japan*, v 3, pp. 118-124.

Yeung, R.W., 1981, "Added Mass and Damping of a Vertical Cylinder in Finite-Depth Waters," Applied Ocean Research, 3, pp. 119-133.

Yilmaz, O., 1998, "Hydrodynamic Interactions of Waves With Group Of Truncated Vertical Cylinders," *J. Wtrwy., Port, Coastal, and Ocean. Engrg.,* 124 (5), pp.272-279

Yilmaz, O., Incecik, A., Barltrop, N., 2001, "Wave Enhancement Due to Blockage in Semi-Submersible And TLP Strucutes," *Ocean Engineering*, 28(5), pp. 471-490.

Yu, X., and Chwang, A. T., 1993, "Analysis of Wave Scattering by Submerged Disk," *J. Engrg. Mech.*, 119(9), pp. 1804-1817.

Yuhi, M., Ishida, H., and Mase, H., 2000, "Numerical Study of Solitary Wave Propagation in Curved Channels," *Coastal Engineering*, PP. 519-532.

Zeng, X., and Tang, S., 2013, "The Hydrodynamic Interactions of an Array of Truncated Circular Cylinders as Each Cylinder Oscillates Independently with Different Prescribed Modes," *J. Hydrodynamics*, 25(1), pp.27-38.

Zheng, S., and Zhang, Y., 2015, "Wave Diffraction from a Truncated Cylinder in Front of A Vertical Wall," *Ocean Engineering*, 104, pp. 329-343.

Zhong, Z., 2007, "Time-Accurate Stabilized Finite Element Model for Nonlinear Shallow-Water Waves," Ph.D Dissertation, University of Houston, Houston, Texas.

Zhong, Z., and Wang, K.H., 2008, "Time-Accurate Stabilized Finite-Element Model For Weakly Nonlinear And Weakly Dispersive Water Waves," *Int. J. Numer. Meth. Fluids*., 57, pp. 715-744.

Zhu, G., Borthwick, A.G.L., Eatock Taylor, R., 2001, "A Finite Element Model of Interaction between Viscous Free Surface Waves and Submerged Cylinders," *Ocean Engineering*, 28(8), pp. 989-1008.